Phase Modulation Two-Photon Microscopy of Hybrid Halide Perovskite

Shi, Qi

2020

Citation for published version (APA):
Shi, Q. (2020). *Phase Modulation Two-Photon Microscopy of Hybrid Halide Perovskite* (Media-Tryck ed.). [Doctoral Thesis (monograph), Chemical Physics]. Lund University.

Total number of authors:
1

LUND UNIVERSITY

PO Box 117
221 00 Lund
+46 46-222 00 00

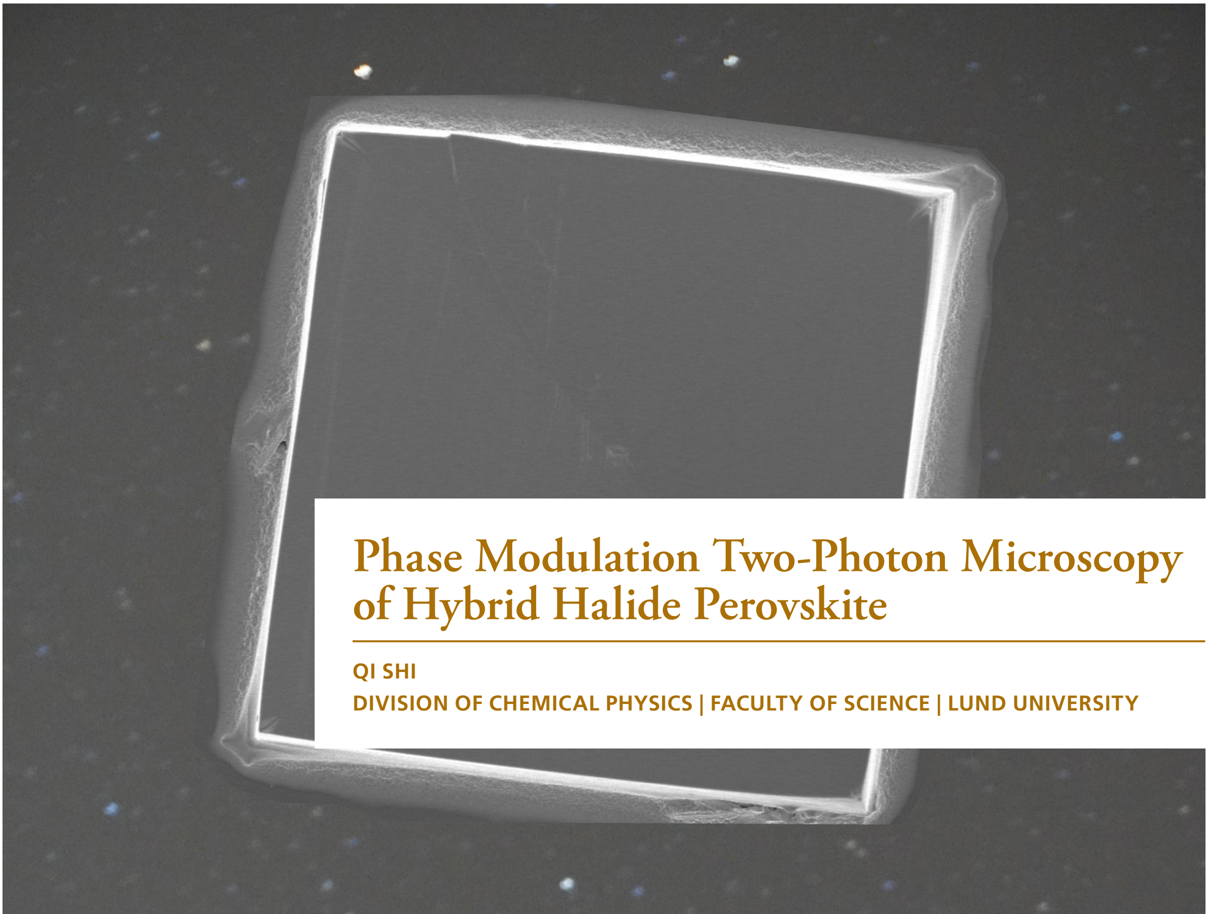

Phase Modulation Two-Photon Microscopy of Hybrid Halide Perovskite

QI SHI
DIVISION OF CHEMICAL PHYSICS | FACULTY OF SCIENCE | LUND UNIVERSITY

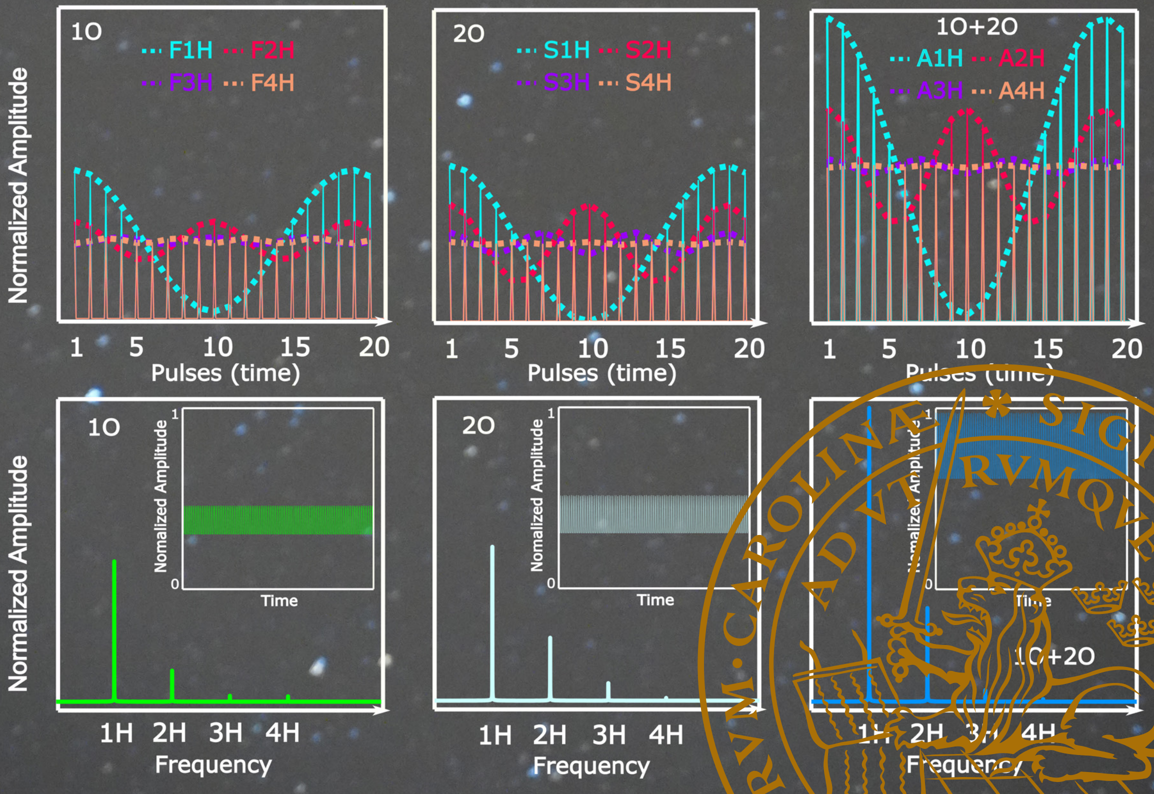

Printed by Media-Tryck, Lund 2020 NORDIC SWAN ECOLABEL 3041 0903

LUND
UNIVERSITY

Faculty of Science
Department of Chemistry
Division of Chemical Physics

ISBN 978-91-7422-768-0

9 789174 227680

Phase Modulation Two-Photon Microscopy of Hybrid Halide Perovskite

Qi Shi

DOCTORAL DISSERTATION

by due permission of the Faculty of Science, Lund University, Sweden.
To be defended at lectural hall A, Kemecentrum, Naturvetarvägen 16, 22362
Lund. Friday the 11th of December at 13:00 pm.

Faculty opponent
Prof. Dr. Elisabetta Collini

Organization LUND UNIVERSITY Division of Chemical Physics Department of Chemistry P.O.Box 124 SE-22100 Lund, Sweden	**Document name** Doctoral Dissertation
	Date of issue 2020-12-11
Author(s) Qi Shi	Sponsoring organization

Title and subtitle
Phase Modulation Two-Photon Microscopy of Hybrid Halide Perovskite

Abstract

Recently, intense research activities have been focused on solution-processed hybrid lead halide perovskite semiconductors which are being developed for the solar-cell, light emitting diode (LED), and lasing applications. To optimize and fabricate a competitive perovskite-based optoelectronic device, the fundamental studies of the electronic structure, photo-generated carrier dynamics as well as the photoluminescence (PL) & photocurrent (PC) response are necessary and of great significance. In this thesis, we have used the temperature dependent phase modulation two-photon PL and PC microscopy to investigate fundamental photophysics of the hybrid halide perovskite. Firstly, we investigate the carrier-phonon scattering process in methylammonium lead bromide ($\mathrm{MAPbBr_3}$) and formamidinium lead bromide ($\mathrm{FAPbBr_3}$) perovskites directly after the excitation by the sunlight or optical lasers. We found that the charge carrier coupling to the longitudinal optical (LO) phonons is stronger than the exciton-acoustic phonon coupling in both $\mathrm{MAPbBr_3}$ and $\mathrm{FAPbBr_3}$ perovskites. The large LO phonon - free charge carrier coupling strength in $\mathrm{MAPbBr_3}$ thin films (TFs) at room temperature hinders the carrier mobility and lowers the PC yield. The charge carriers recombine via exciton or free charge carrier recombination. By separately quantifying spatially resolved emission from excitons and free charge carriers in $\mathrm{MAPbBr_3}$ bulk crystals, we found that the emission from excitons is predominant in the small isolated localized spot of the crystal while the emission from the free charge carriers is predominant in the main bulk crystal. The larger band structure deformation surrounding the localized spot protects the photo-generated carriers and promotes the first order (1O) recombination. Considering the charge accumulation effect in the high repetition rate excitation system, the trap states and their dependence on phase transition at low temperature are explored. We found that the areas with less traps have more second order recombination emission. With decreasing temperature, the 1O recombination emission is increasing due to the increased exciton population and the related emission. Besides, the lifetime related to the accumulation effect is decreasing since the electrons cannot de-trap from the deeper traps. In addition, the studies on the photo physics processes may help to develop highly efficient $\mathrm{MAPbBr_3}$ perovskites solar cells and photodetectors. The relationship between the PC performance with the different emissive states is investigated in a $\mathrm{MAPbBr_3}$ solar cell. The results suggest that the high emissive state at 2.34 eV, corresponding to the band to band recombination, strongly contributes to the PC, while the lower emissive state at 2.28 eV does not significantly contribute to the PC since it is a trap state. When working as a $\mathrm{MAPbBr_3}$ microcrystal (MC)-based photodetector, the carrier transport length can vary from 5.7 µm (0.02 V) due to diffusion to 23.2 µm (2 V) due to the drift. For the solar cell and photodetector application, the inhomogeneous distribution of the trap states introduces spatially inhomogeneous distribution of PC as well as PL.

Key words
Phase modulation, two-photon microscopy, perovskite, trap, carrier recombination

Classification system and/or index terms (if any)

Supplementary bibliographical information		**Language** English
ISSN and key title		**ISBN** 978-91-7422-768-0 (print) 978-91-7422-769-7 (PDF)
Recipient's notes	**Number of pages**	Price
	Security classification	

I, the undersigned, being the copyright owner of the abstract of the above-mentioned dissertation, hereby grant to all reference sources permission to publish and disseminate the abstract of the above-mentioned dissertation.

Signature Qi Shi Date 2020-11-02

Phase Modulation Two-Photon Microscopy of Hybrid Halide Perovskite

Qi Shi

LUND
UNIVERSITY

Coverphoto by Juanzi Shi and Qi Shi

Faculty of Science
Department of Chemistry
Division of Chemical Physics

ISBN 978-91-7422-768-0 (print)
ISSN 978-91-7422-769-7 (PDF)

Printed in Sweden by Media-Tryck, Lund University
Lund 2020

Be happy every day.

Table of Contents

Abstract

Recently, intense research activities have been focused on solution-processed hybrid lead halide perovskite semiconductors which are being developed for the solar-cell, light emitting diode (LED), and lasing applications. To optimize and fabricate a competitive perovskite-based optoelectronic device, the fundamental studies of the electronic structure, photo-generated carrier dynamics as well as the photoluminescence (PL) & photocurrent (PC) response are necessary and of great significance.

In this thesis, we have used the temperature dependent phase modulation two-photon PL and PC microscopy to investigate fundamental photophysics of the hybrid halide perovskite. Firstly, we investigate the carrier-phonon scattering process in methylammonium lead bromide ($MAPbBr_3$) and formamidinium lead bromide ($FAPbBr_3$) perovskites directly after the excitation by the sunlight or optical lasers. We found that the charge carrier coupling to the longitudinal optical (LO) phonons is stronger than the exciton-acoustic phonon coupling in both $MAPbBr_3$ and $FAPbBr_3$ perovskites. The large LO phonon - free charge carrier coupling strength in $MAPbBr_3$ thin films (TFs) at room temperature hinders the carrier mobility and lowers the PC yield. The charge carriers recombine via exciton or free charge carrier recombination. By separately quantifying spatially resolved emission from excitons and free charge carriers in $MAPbBr_3$ bulk crystals, we found that the emission from excitons is predominant in the small isolated localized spot of the crystal while the emission from the free charge carriers is predominant in the main bulk crystal. The larger band structure deformation surrounding the localized spot protects the photo-generated carriers and promotes the first order (1O) recombination. Considering the charge accumulation effect in the high repetition rate excitation system, the trap states and their dependence on phase transition at low temperature are explored. We found that the areas with less traps have more second order recombination emission. With decreasing temperature, the 1O recombination emission is increasing due to the increased exciton population and the related emission. Besides, the lifetime related to the accumulation effect is decreasing since the electrons cannot de-trap from the deeper traps. In addition, the studies on the photo physics processes may help to develop highly efficient $MAPbBr_3$ perovskites solar cells and photodetectors. The relationship between the PC performance with the different emissive states is investigated in a $MAPbBr_3$ solar cell. The results suggest that the high emissive state at 2.34 eV, corresponding

to the band to band recombination, strongly contributes to the PC, while the lower emissive state at 2.28 eV does not significantly contribute to the PC since it is a trap state. When working as a $MAPbBr_3$ microcrystal (MC)-based photodetector, the carrier transport length can vary from 5.7 μm (0.02 V) due to diffusion to 23.2 μm (2 V) due to the drift. For the solar cell and photodetector application, the inhomogeneous distribution of the trap states introduces spatially inhomogeneous distribution of PC as well as PL.

Popular science summary

Due to the increased consumption of energy, and the increased CO_2 levels, the development of renewable energy sources, such as photovoltaics and the related materials is on demand. Solution processed hybrid halide perovskite with low cost show promising application in solar cells, light emitting diodes and lasers devices. In order to achieve commercially competitive products comparable or better than the traditional silicon and gallium arsenide photovoltaic devices, the fundamental working principles such as light absorption, charge carrier transport and photo emission processes need comprehensive understanding.

When the material is exposed to the sunlight, free electron hole pairs and excitons will be generated. These species and the interaction among them will have a significant influence on the performance of the photovoltaic and light emitting diode devices. Therefore, in this thesis, aiming to improve the performance of hybrid halide perovskites, we used the phase modulation two-photon microscopy technique to investigate the related species and their interaction processes. Based on $MAPbBr_3$ and $FAPbBr_3$ perovskite, the effect of the temperature and spatial inhomogeneity are also taken into account. It was found that the population of free electron and hole pairs is predominant at room temperature, which benefits the perovskite-based photovoltaic devices. The population of excitons is predominant at low temperature, which benefits the perovskite-based light emitting diode devices. Besides, the phonon coupling with free electron hole pair and exciton limits the carrier mobility and lowers the power conversion efficiency of perovskite-based photovoltaic and lasing devices. Thirdly, the compress strain engineering through structural designs could improve the performance of perovskite-based light emitting diodes. In addition, we also found a good sample preparation procedure could reduce the impurities and improve the performance of the perovskite. Finally, we use hybrid halide perovskite microcrystals to fabricate photodetectors and it shows great potentials to work as good photodetectors.

Acknowledgement

I would like to give my sincerest thanks to all the people who have helped and supported me during my PhD life. This thesis could have not been accomplished without your help.

First and foremost, I want to thank my main-supervisor Prof. Dr. Tönu Pullerits, who has provided me this precious opportunity to work as a PhD student in Lund University. You are so friendly, nice, and enlightened, making my PhD life relax and happy. Besides, your rigorous attitude on scientific research has given me a deep impression and influenced me. One of the most memorable things is that when we discussed the charge accumulation effect work together, your patient, knowledgeable, professional, and meticulous attitude on science gave me much encouragement and made me respect science more and more.

To Dr. Khadga Jung Karki, co-supervisor of my PhD studies for 2.5 years, you have shared me a lot of knowledge about the phase modulation, semiconductor physics, digital sampling, many software programs, and practical skills in the workshop. You helped me a lot in paper writing and publishing as well. Thanks a lot.

Supriya Ghosh and Pushpendra Kumar, we have worked together on several projects. You are open-minded and have a good scientific sense. It is comfortable and good to work with you. I wish you all the best in your future work.

All the co-authors of the publications, thank you all for the work we have done together. Thanks to Laura for introducing me to the XRD measurements. Thanks to Alexander Dobrovolsky for teaching me the SEM and sputtering operation in NanoLab.

Prof. Akady Yartsev, thank you for all the kind answers whenever I came to your office with my questions. Prof. Ivan Scheblykin, thanks for your kind contribution to the kitchen and workshop maintenance. I still remember the nice trip to Singapore together with Jun and Juanzi. Prof. Donatas Zigmantas, thanks for organizing the 2D spectroscopy book reading club and I really appreciate it. Prof. Per Uvdal, thanks for good chatting with you during the breaks, it has made me feel easy and happy to work here.

Kaibo and Junsheng, you helped me a lot both in work and daily life. Kaibo, you have helped me about the synthesis of the $MAPbBr_3$ bulk crystals. Junsheng, you have helped me a lot for many small and cumbersome problems at the beginning of my PhD study. Thanks for giving me the chance to hold the Department Hotpot Party and Department Dumpling Party with you.

To Tönu's group members: Kaibo Zheng, Junsheng Chen, Daniel Finkelstein-Shapiro, Pavel Chabera, Zhengjun Wang, Weihua Lin, Alireza Honarfar, Wei Zhang, Anurag Kawde, Albin Hedse, Yanmei He, and Fan Wu. I really enjoy the group meetings and discussions with all of you.

I would like to thank Guangmeng Guo at the Institute of Optics and Electronics, Chinese Academy of Science for helping me a lot with the programming in Qt. I would also like to thank Chen Lan in Nankai University for helping me a lot with understanding the mathematic derivations in many articles. I would also thank Sudipta Seth for having a good time in Lund, discussion the perovskite material and sharing many interesting things around us.

Thanks to all the Chemphys members. I really enjoy the seminars, Fika, social activities (Department BBQ, Department Hotpot Party, and Department Dumpling Party), spring trips, science days, and Christmas parties a lot. Thank you all for making my PhD life colorful and interesting.

To my good friends in Sweden, Huifang Geng, Juanzi Shi, Xin Liu, Haiyue Gong, Haoran Yu. We have had four years of great and fantastic time. We have experienced a lot such as: Christmas travel to Switzerland and Venice, Dapanji gathering in Kämnarsvägen, the Amazing Race in Copenhagen, aurora travel to Tromsö, good time in Öland, exciting canoeing and camping in Halens Camping och Stugby, and swimming in Falsterbo.

Besides, thanks to many friends in lund, BinYang, Chen Sun, Chuanshuai Li, Fang Huang, Fengying Zhang, Guanquan Du, Hong Jiang, Huiting Ma, Jie Zhang, Jun Li, Kena, Li, Liu Yang, Meng Dan, Meiyuan Guo, Pushpendra Kumar, Ruiyun Chen, Shraddha Rao, Sudipta Seth, Supriya Ghosh, Xianshao Zou, Xiaoqing Hou, Xiaoyan Xu, Yao Wang, Yuanze Chen, Yuchen Liu, Yue Wu, Yuhan Ma, Yupan Bao, Yunqian Zhong, Zhengkan Wang.

I would like to thank the financial support from China Scholarship Council (CSC) and Royal Physiographic Society. I would also like to thank my Bachelor's supervisor Prof. Dr. Sujuan Li at Anyang Normal University for leading me to the world of research. Also, sincere thanks to my Master's supervisor Prof. Dr. Yixiang Duan in Sichuan University and our Research Center of Analytical Instrument group for providing me the high level scientific platform and giving me freedom to explore my interest in research.

Thanks to Wei Zhang and Sudipta Seth for proofreading the thesis.

Guanghui Niu, my boyfriend, thanks a lot for your love, understanding, and support. You helped me a lot in manuscript and thesis writing. You also make a lot of delicious food for us.

最后感谢我的父亲母亲，每周末与你们的视频聊天给了我很多快乐和幸福。看到你们每天开心快乐是身在瑞典的我最开心的事情。希望你们以后的每一天都能开心快乐、幸福安康。感谢我的哥哥嫂子在父母身边无微不至的照顾，你们的陪伴让我在瑞典更加安心和放心的工作。希望你们日后的每一天都能幸福开心。最后感谢我的侄女侄子，每周末的视频你们的微笑都给予了我很

多的幸福与鼓舞。每次看到你们的笑容，我的心情就会特别好。希望你们开心快乐的长大。

List of publications

This thesis is based on the following papers, which will be referred to in the text by Roman numerals.

I. **Shi, Q.,** Ghosh, S., Sarkar, A. S., Kumar, P., Wang, Z., Pal, S. K.*, Pullerits, T*. & Karki, K. J*. (2018). Variation in the photocurrent response due to different emissive states in methylammonium lead bromide perovskites. *The Journal of Physical Chemistry C*, *122*(7), 3818–3823.

II. Yang, B., Chen, J., **Shi, Q.,** Wang, Z., Gerhard, M., Dobrovolsky, A., Scheblykin, I., Karki, K. J*. Han, K, L.*, & Pullerits, T*. (2018). High resolution mapping of two-photon excited photocurrent in perovskite microplate photodetector. *The journal of physical chemistry Letters*, *9*(17), 5017–5022.

III. Ghosh, S., **Shi, Q.,** Pradhan, B., Kumar, P., Wang, Z., Acharya, S., Pal, S. K.*, Pullerits, T.*, & Karki, K. J*. (2018). Phonon coupling with excitons and free carriers in formamidinium lead bromide perovskite nanocrystals. *The Journal of Physical Chemistry Letters*, *9*(15), 4245–4250.

IV. **Shi, Q.,** Ghosh, S., Kumar, P., Folkers, L. C., Pal, S. K., Pullerits, T., & Karki, K. J*. (2018). Variations in the Composition of the Phases Lead to the Differences in the Optoelectronic Properties of MAPbBr3 Thin Films and Crystals. *The Journal of Physical Chemistry C*, *122*(38), 21817–21823.

V. Kumar, P., **Shi, Q.,** & Karki, K. J*. (2019). Enhanced radiative recombination of excitons and free charges due to local deformations in the band structure of MAPbBr3 perovskite crystals. *The Journal of Physical Chemistry C*, *123*(22), 13444–13450.

VI. **Shi, Q.,** Kumar, P., Karki, K. J. & Pullerits, T*. (2020). Impurity effects change with phase transition in hybrid metal halide perovskite. Manuscript.

My Contribution to the Publications

I. I performed the measurements of phase modulation two-photon luminescence (PL) and photocurrent (PC) microscopy under different applied biases. I analysed the PC and, PL imaging data, PL spectrum data. I was responsible for writing the major part of the paper.

II. I performed the measurements of the I-V curves, excitation light density dependent two-photon PC, excitation light density dependent responsivity, frequency-dependent two-photon PC, and two-photon PC mapping under different biases, analysed the experiment data, and discussed the manuscript with other authors.

III. I performed the measurements of temperature dependent two-photon PL spectra together with Supriya Ghosh, analysed the experimental data, and I contributed to the paper writing.

IV. I performed the measurements of temperature dependent two-photon PL spectra together with Supriya Ghosh, analysed the experiment data. I was responsible for writing the major part of the paper.

V. I analysed the temperature dependent phase modulation two-photon PL experimental data, discussed the manuscript, and drafted the manuscript.

VI. I analysed and modelled the temperature dependent phase modulation two-photon PL experiment data. I was responsible for writing the major part of the paper.

Other publications are not included in this thesis

VII. Kumar, P., Eisenhauer, D., Yousef, M. M. K., **Shi, Q.,** Khalil, A. S. G., Saber, M. R., Becker, C., Pullerits, T., & Karki, K. J. (2018). Photoimpedance Spectroscopy Analysis of Planar and Nano-Textured Thin-Film Silicon Solar Cells. *International Journal of Physical and Mathematical Sciences*, *12*(2), 57–61.

VIII. Karki, K. J., Chen, J., Sakurai, A., **Shi, Q.,** Gardiner, A. T., Kühn, O., Cogdell, R., & Pullerits, T. (2019). Before Förster. Initial excitation in photosynthetic light harvesting. *Chemical Science*, *10*(34), 7923–7928.

IX. Meng, J., Lan, Z., Abdellah, M., Yang, B., Mossin, S., Liang, M., Naumova, M., **Shi, Q.,** Alvarez, S., Liu, Y., Lin, W., Castelli, I., Canton, S., Pullerits, T., & Zheng, K. (2020). Modulating Charge-Carrier Dynamics in Mn-Doped All-Inorganic Halide Perovskite Quantum Dots through the Doping-Induced Deep Trap States. *The Journal of Physical Chemistry Letters*, *11*(9), 3705-3711.

X. Ghosh, S., **Shi, Q.,** Pradhan, B., Mushtaq, A., Acharya, S., Karki, K. J., Pullerits, T., & Pal, S. K. (2020). Light-Induced Defect Healing and Strong Many-Body Interactions in Formamidinium Lead Bromide Perovskite Nanocrystals. *The Journal of Physical Chemistry Letters*, *11*(4), 1239-1246.

XI. Niu, G., **Shi, Q.,** Yuan, X., Wang, J., Wang, X., & Duan, Y. (2018). Combination of support vector regression (SVR) and microwave plasma atomic emission spectrometry (MWP-AES) for quantitative elemental analysis in solid samples using the continuous direct solid sampling (CDSS) technique. *Journal of Analytical Atomic Spectrometry*, *33*(11), 1954–1961.

XII. Guo, G., Niu, G., **Shi, Q.,** Lin, Q., Tian, D., & Duan, Y. (2019). Multi-element quantitative analysis of soils by laser induced breakdown spectroscopy (LIBS) coupled with univariate and multivariate regression methods. *Analytical Methods*, *11*(23), 3006–3013.

Abbreviations

1O	First order
2O	Second order
3O	Third order
1H	First harmonic
2H	Second harmonic
3H	Third harmonic
4H	Fourth harmonic
A1H	first harmonic signal from first order and second order recombination
A2H	second harmonic signal from first order and second order recombination
A3H	third harmonic signal from first order and second order recombination
A4H	fourth harmonic signal from first order and second order recombination
ADC	Analog to digital converter
ALL1O	All the first order recombination generated PL
ALL2O	All the second order recombination generated PL
AOM	Acousto-optical modulator
APD	Avalanched photodiode
BS	Beam splitter
CB	Conduction band
CMP	Chirped mirror pair
CU	Cubic
DM	Dichroic mirror

DFT	Discrete Fourier transform
DSPVs	Dye-sensitized photovoltaics
F1H	first harmonic signal from first order recombination
F2H	second harmonic signal from first order recombination
F3H	third harmonic signal from first order recombination
F4H	fourth harmonic signal from first order recombination
FFT	Fast Fourier transform
FWHM	Full width at half maximum
GM	Göppert-Mayer
GSa/s	Giga sample per second
HR	High PL region
IPSE	Illumination point spread function
ITO	Indium tin oxide
LEDs	light-emitting diodes
LO	Optical phonon moving in the longitudinal dimension
LOR	Localized spot region
LR	Low PL region
M	Microscope
MC	Microcrystal
MR	Middle PL region
MZI	Mach-Zehnder interferometer
NA	Numerical aperture
NIR	Near-infrared
OPVs	Organic photovoltaics
OR	Orthorhombic
PC	Photocurrent
PCE	Power conversion efficiency
PL	Photoluminescence
PV	Photovoltaic

RO	Reflective objective
RF	radio frequency
S1H	first harmonic signal from second order recombination
S2H	second harmonic signal from second order recombination
S3H	third harmonic signal from second order recombination
S4H	fourth harmonic signal from second order recombination
SEM	Scanning electron microscope
SNR	Signal to noise ratio
SPCM	Scanning photocurrent microscopy
SQ	Shockley-Queisser
SL	Saha-Langmuir
TE	Tetragonal
TPA	Two-photon absorption
THz	Terahertz
VB	Valence band

Chapter 1 Introduction

1.1 Perovskite materials for renewable and sustainable energy

With increased population, world economy, and urbanisation, the threat of the looming energy crisis is gradually increasing. While due to the rising CO_2 emission by the fossil fuels, the usage of renewable energy from sunlight, wind, hydro, tides, waves and geothermal heat is increasing steadily[1]. Photovoltaics works well as clean energy resource and many kinds of solar cells have been developed such as crystalline silicon, dye sensitized, quantum dot, organic, and inorganic-organic heterojunction solar cells[2]. Many researchers in various fields, including, but not limited, to materials science, chemistry, electrical engineering, chemical physics have joined forces to enhance the power conversion efficiency (PCE) of solar cells to make it competitive, compared with the traditional fossil fuels. At present, crystalline silicon and single junction gallium arsenide (GaAs) based solar cells perform excellentlly with the highest PCE of 27.6 %[3] and 30.5 % under one-sun and concentrated illumination, respectively (**Figure 1.1**)[4]. The PCE can be as high as 47.1 % for the multijunction devices[5], exceeding the theoretical Shockley-Queisser limit which is about 33.7 %[6]. The cost of such multi-junction solar cells is quite high, limiting their application mainly to space power. Therefore, it is essential to find easy fabrication and low cost alternatives, such as organic photovoltaics (OPVs)[7] and dye-sensitized photovoltaics (DSPVs)[8].

Recently, intense research activities have been focused on solution-processed hybrid lead halide perovskite semiconductor for their promising application in the fields of photovoltaic (PV) [9–17], light-emitting diodes (LEDs) devices [18–21], light diode[22,23], and lasers[24,25], due to the unique advantages such as high optical absorption coefficients, high carrier mobility, long carrier recombination time, and excellent electron-hole diffusion length[9,10,19–25,11–18]. The most efficient perovskite solar cell has a PCE of 25.2 % (**Figure 1.1**)[4]. These above mentioned parameters have a close relationship with the electronic structure of the material and charge carrier generation as well as recombination processes when being used for electronic devices[11,12,26].

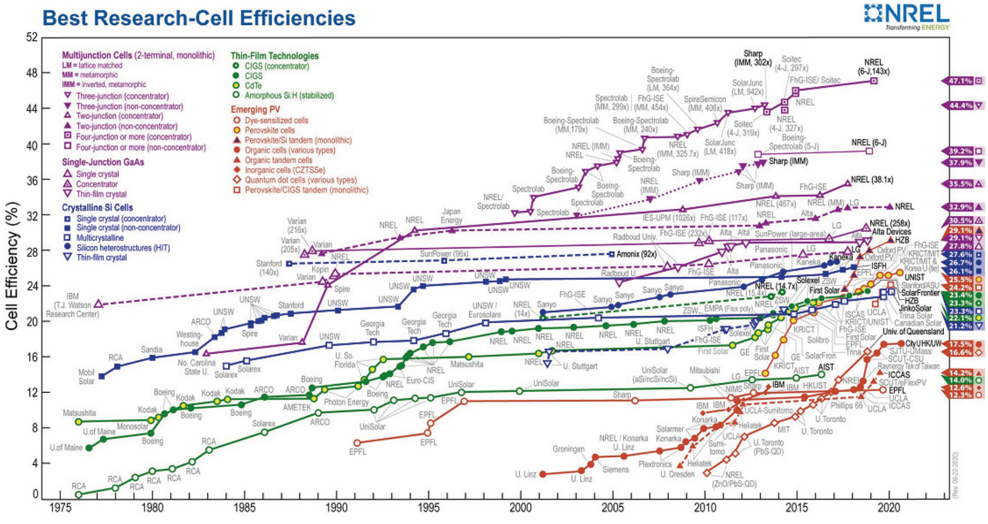

Figure 1.1
Reported timeline of solar cell power conversion efficiencies since 1976 (courtesy of the National Renewable Energy Laboratory, Golden, CO)

The name Perovskite originates from a famous Russian mineralogist Lev Perovski and refers to the crystal structure of the mineral calcium titanium oxide $CaTiO_3$, the chemical formula of which can be represented as ABX_3[27]. For a highly efficient photovoltaic cell based on perovskite semiconductor, A is a monovalent cation such as methylammonium ($CH_3NH_3^+$ or MA^+), formamidinium ($CH_3(NH_2)_2^+$ or FA^+), caesium (Cs^+) or their mixture. The divalent cation B typically represents lead (Pb (II)) or tin (Sn (II)). X stands for halogen elements which bind A and B together, including chloride (Cl^-), bromide (Br^-), and iodine (I^-)[28]. The divalent metal cation B (such as MA^+) has a 6-fold coordination and forms an octahedron unit with X (such as Br^-).

$MAPbBr_3$ perovskites, in particular, are more stable than the iodine (I) counterparts and can be used in tandem solar cell to harvest visible light[29–31]. There are three phases, namely cubic (CU), tetragonal (TE), and orthorhombic (OR), for the ABX_3 bulk crystal with different orientation and distortion of the BX_6 octahedra and cation methylammonium (A)[32]. The crystal structure of $MAPbBr_3$ with TE phase is shown in **Figure 1.2 (a)** and **(b)**, respectively. Phase of the hybrid lead halide perovskite plays an important role in the band structure[33], phonon-carrier coupling[34,35], and charge-carrier dynamics[36].

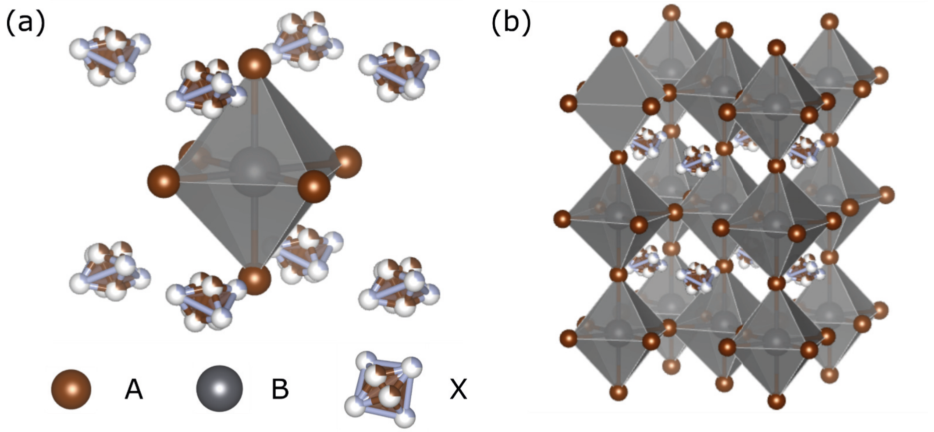

Figure 1.2
(a) Crystal structure of $MAPbBr_3$ perovskite in TE phase. A (MA^+), B (Pb (II)), and X (Br^-). **(b)** three-dimensional perovskite lattice structure.

1.2 Electronic structure of hybrid halide perovskite

In semiconductors, when a number of atoms come together, a band is formed due to the splitting of each atomic orbital into many energy levels. The highest occupied band is normally called valence band (VB), while the lowest unoccupied band is conduction band (CB). The energy gap between CB and VB is called bandgap of the semiconductor.

It has been widely reported that the band edge states in organic/inorganic lead bromide perovskite originate mainly from the orbitals of lead and halide[37,38]. As shown in **Figure 1.3 (a)**, there are mainly four types of orbital hybridization that contribute to the CB edge and upper VB. They are bonding Pb (6s) - I (5p) and Pb (6p) – I (5p) orbitals compositing the deeper VB and antibonding Pb (6s) – I (5p) and Pb (6p) – I (5p) orbitals compositing the CB edge and VB edge. It is calculated that the antibonding states at the VB and the bonding states at the CB are likely to be tolerant to defects in semiconductors[39]. Besides, the dangling bonds or vacancies form states which are shallow defects close to the band edges or are within the CB or VB. While for most of the defect-intolerant semiconductors shown in **Figure 1.3 (b)**, the CB is composited by antibonding states and VB by bonding states. Therefore, the nonbonding or weakly bonding orbitals act as trap states that reside deeply within the band gap[40].

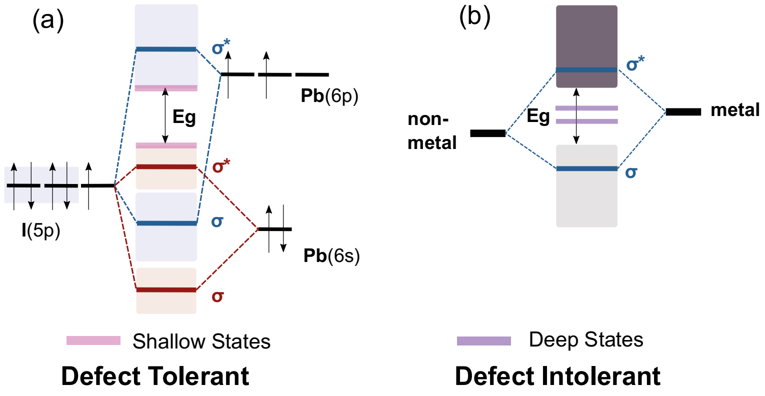

Figure 1.3
(a) Bonding and antibonding orbitals in $MAPbI_3$ demonstrating the formation of energy bands relative to isolated *p* and *s* atomic orbital energies. (b) electronic structures of the conventional semiconductors which is defect-intolerant.

1.3 Carrier kinetics

1.3.1 Generation of excitons and free charge carriers

Being exposed to a light with energy larger than the band gap, the semiconductor material can absorb a photon by which a valence electron is promoted to the CB. If the photon energy is high, an electron-hole pair with energy significantly higher than the band gap can be generated. The minimum energy to dissociate the exciton is called exciton binding energy (E_b). If the thermal energy exceeds the binding energy E_b, the exciton rapidly dissociates into free electron and hole pairs. At the same time an electron and a hole can meet and form an exciton. These two processes are in equilibrium where the dissociation rate is determined by the temperature and the exciton binding energy while the recombination depends on the concentration of the free charge carriers which is proportional to the excitation fluence. This equilibrium can be described by the Saha-Langmuir equation[34,35,41–43],

$$\frac{x^2}{1-x} = \frac{1}{n}\left(\frac{2\pi\mu k_B T}{h^2} e^{\frac{-E_b}{k_B T}}\right) \quad (1.1)$$

where x is the ratio between the free charge carriers over the total excitation density; n is the excitation density; h is the Planck constant; k_B is the Boltzmann constant; μ is the reduced mass of the exciton. This relationship shows that the relative population of the free charge carriers increases with the increased temperature and decreased excitation density.

1.3.2 Early stage hot carrier cooling via carrier-phonon scattering

When the charge-carriers have energy above the band edge which corresponds to a thermal energy that is significantly higher than the lattice temperature, the carriers are termed as hot carriers. The distribution of the hot carriers is not in equilibrium and subsequently these hot carriers will relax via processes such as charge-carrier interaction, in other words, carrier-phonon scattering[44]. Several groups proposed that the carrier-phonon coupling limits the charge-carrier mobility and leads to the emission line broadening in hybrid metal halide perovskites[45–48]. They discovered that the scattering from longitudinal optical phonons (LO phonon) via Fröhlich interaction is the predominant process at room temperature, while the scattering from the acoustic phonons is negligible. The hot carriers are cooled down by interacting with LO phonon firstly. A subsequent interaction between the LO phonon and acoustic phonon will reestablish the thermal equilibrium. The timescale of the cooling process is quite important for designing an excellent solar cell device to extract the hot carriers and generate high open-circuit voltage and PCE. While the timescale of the hot carrier cooling is generally investigated using transient absorption spectroscopy which is beyond the outline of this thesis. However, the coupling strength between the phonons and the carriers can be studied by investigating the photoluminescence (PL) spectral linewidth which is closely related to the interaction process. The LO phonon interaction strength has an inverse relationship with the carrier mobility based on the Feynman-Ösaka model[35,49–51]. Therefore, the understanding of the hot carrier cooing via carrier-phonon scattering will give more information on the carrier mobility which is essential to develop high efficient perovskite photovoltaics and lasers.

1.3.3 Recombination

Besides cooling, the charge carriers recombine. The charge carrier recombination dynamics can be expressed in terms of the orders of concentration or population – the first-order (1O), second-order (2O), third-order (3O) in the population, as expressed through the rate equation $\frac{dn}{dt} = -k_3 n^3 - k_2 n^2 - k_1 n$ [11,12,52]. In the equation, k_1 is the rate constant associated with 1O recombination, which depends on the population of electrons (n_e), holes (n_h) or excitons. If shallow electron traps are present, k_1 is related to the recombination of a trapped electron with surrounding abundant holes. Analogous process for the trapped holes can also take place. k_2 is the 2O charge-carrier recombination rate constant, which depends on the square of the population – for example multiplication of the population of electrons and holes. The proportion of the free charge carrier population can be evaluated based on the Saha-Langmiur (SL) theory[34,35,41]. k_3 represents the rate constant of Auger recombination in which the recombination energy of the electron-hole pair is transferred to a third participant, either an electron or a hole. Therefore, the total recombination rate $r(n)$ (**equation 1.2**) which influences the charge-carrier diffusion length L_D (**equation 1.3**) is the comprehensive result of three combination mechanisms[52,53],

$$r(n) = k_3 n^2 + k_2 n + k_1 \quad (1.2)$$

$$L_D = \sqrt{\frac{\mu k_B T}{q} \frac{1}{r(n)}} \quad (1.3),$$

where μ is the carrier mobility; k_B is the Boltzmann constant; q is the elementary charge and T is the temperature.

Besides, the trap states introduced by the impurities, also make a significant influence on the recombination kinetics of the carriers[11,12,58–65,15,34,35,52,54–57]. Typically, the impurities can be introduced in the form of interstitial impurity atoms, edge dislocations, and vacancies[66].

1.4 Phase modulation two-photon PL and PC microscopy

1.4.1 Two-photon microscopy

1.4.1.1 Two-photon absorption (TPA)

Two-photon absorption microscopy is a popular imaging technique in live animal[67–71] and brain slices[72,73]. It typically uses a near-infrared (NIR) light to generate two-photon absorption (TPA), which was originally predicted by Maria Goeppert-Mayer in 1931[74]. TPA is the simultaneous absorption of two photons by which an electron is promoted from a lower energy state to a high energy level (such as from VB to CB in a semiconductor) while the energy difference between the levels is equal to the sum of the absorbed photons' energies. TPA technique was firstly verified by the two-photon-excited fluorescence in a europium-doped crystal[75]. The relationship between the light intensity and the two-photon absorption is quadratic. The transition probability R_0 of TPA can be given by

$$R_0 = s_2 I_0^2 \quad (1.4).$$

Normally, the excitation intensity I_0 represents the number of excitation photons passing through the investigated object per unit area per unit time (photons cm^{-2} s^{-1}). s_2 is the TPA cross section in cm^{4}s, and 1GM (Göppert-Mayer) = 10^{-50} cm^{4}s.

1.4.1.2 Three-dimensionally localized excitation

The three-dimensionally localized excitation in TPA can increase the transition probability and enable the excitation at different depth in the investigated object. Take 1 mW laser excitation as an example,

$$1\,mW = 10^{-3}\left(\frac{J}{s}\right) \; (1.5)$$

The photon energy is obtained as: $E = \frac{hc}{\lambda} = \frac{6.626*10^{-34}\,Js*3.0*10^{8}\,\frac{m}{s}}{\lambda*10^{-9}\,m} = \frac{1.989*10^{-16}}{\lambda}\,(J)$ (1.6).

The number of photons per second with wavelength located at 790 nm is written as: $n = \frac{10^{-3}\,\frac{J}{s}}{\frac{1.989*10^{-16}}{\lambda}\,J} = 5*10^{12}*\lambda\left(photons\,\frac{1}{s}\right) = 3.95*10^{15}\left(photons\,\frac{1}{s}\right)$ (1.7).

Then the number of the photons is divided by the focal plane area. Diffraction limited objectives produce a minimum focused spot size defined by the Airy Disk. The minimum spot diameter can be calculated using the numerical aperture (NA) of the objective and laser wavelength:

Minimum spot diameter = $1.22\frac{\lambda}{NA} = 1.22*\frac{790\,nm}{0.5} = 1.927\,(\mu m)$ (1.8).

The area of the focusing spot is $s = \pi r^2 = 2.9166*10^{-8}\,cm^2$ (1.9).

Therefore, the excitation intensity I can be obtained as: $I = \frac{3.95*10^{15}photons\,\frac{1}{s}}{2.9166*10^{-8}\,cm^2} = 1.3543*10^{23}\,\frac{photons}{s*cm^2}$ in the focal plane.

Compared with one photon absorption, the excitation volume of TPA process is quite small. The illumination point spread function $IPSF(x,y,z)$ can be used to describe the intensity distribution around the focal point. For two-photon microscopy, the $IPSF(x,y,z)^2$ can be used to describe the three-dimensional Gaussian-like volume. The square of the $IPSF$ minimize the wings relative to the center. Therefore, the excitation intensity decreases rapidly and there is little TPA process off the focal plane. As a result, the three-dimensional resolution is superior for the two-photon microscopy. The volume can be calculated as

$V_{focus} = \pi^{\frac{3}{2}}\omega_{xy}^2\omega_z$ (1.10).

With $NA \le 0.7$, $\omega_{xy} = \frac{0.320\lambda}{\sqrt{2}NA}$, $\omega_z = \frac{0.532\lambda}{\sqrt{2}}\left[\frac{1}{n-\sqrt{n^2-NA^2}}\right]$, where n is the refractive index of the material, ω_{xy} and ω_z are the estimated diffraction-limited lateral and axial 1/e radii of $IPSF(x,y,z)^2$ by fitting the lateral and axial intensity squared profiles with gaussian function[76–78]. The schematic diagrams of the $IPSF(x,y,z)$

for the one-photon absorption and the $IPSF(x,y,z)^2$ for the two-photon absorption are shown in **Figure 1.4 (a) and (b)**, respectively. Compared with one-photon absorption, the excitation area of the two-photon absorption is strictly confined in the focal plane because the two-photon absorption happens nearly simultaneously with extremely high photon density.

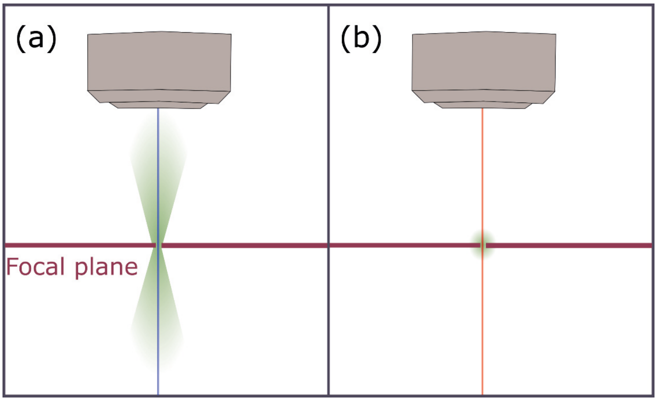

Figure 1.4
The schematic diagrams of the (a) one-photon absorption and (b) two-photon absorption. The insert figure in the middle shows the axial profile (0,0,z) of $IPSF^2$.

A femtosecond laser pulse train (Ti:sapphire laser, 700 - 900 nm) is the most commonly used source to generate enough TPA process due to the increased probability for the simultaneous interaction of two photons but with a relatively low average power. The average squared intensity can be calculated as[78–80],

$$< I(t)^2 >= \frac{g_P < I(t) >^2}{(R\tau)} \quad (1.11),$$

where g_P is a factor which depends on the temporal laser pulse shape (0.66 for Gaussian pulse shape); τ is the full-width half-maximum of the pulse (8 fs); R is the repetition rate 70.16 MHz. Thus, the TPA process has been increased by $\frac{g_P}{(R\tau)} \approx 1.176 * 10^6$ times while the average intensity of the beam is the same.

1.4.1.3 Low scattering intensity

TPA can reduce the scattering intensity more compared with one photon absorption due to the longer incident optical wavelength, resulting in a better signal to noise ratio (SNR). The relationship between the scattering intensity α and the wavelength of the incident radiation λ is shown as

$$\alpha = \frac{\pi D_p}{\lambda} \quad (1.12),$$

where D_p is the diameter of an object particle.

1.4.1.4 Deep penetration depth

The penetration depth is to describe the decayed intensity of the incident electromagnetic wave ($\frac{1}{e}$ (about 37%) of its original value) inside of a material. Based on Beer-Lambert law, the intensity of the decayed electromagnetic wave at depth z inside the material $I(z)$ can be described as

$$I\ (z) = I_0 e^{-\alpha z} \ \ (1.13),$$

where I_0 is the intensity of the incident electromagnetic wave on the material surface.

The penetration depth can be represented as: $z = \frac{1}{\alpha}$ (1.14).

The photons with energies below the band gap cannot be absorbed through one-photon absorption. Thus, the penetration depth of the two-photon excitation is longer than the that of one-photon excitation, if the photon energy is below the band gap.

1.4.2 Phase modulation spectroscopy

The effect of light intensity on the intrinsic action signal (such as PC and PL in a solar cell) can be used to investigate how the recombination process occurs and contribute to the functionality of a system. Various techniques have been utilized to follow different charge carrier recombination dynamics, including PL, photocurrent (PC), time-resolved PL, optical-pump–optical or terahertz (THz) probe spectroscopy, and others[36,54,81–83]. For example, based on the transient absorption microscopy, Nah et al. investigated the difference between the signals from free charges and excitons[84], while the direct information about the subsequent effect of the fast processes could not be observed.

The interaction of a system with coherent light leads to the excitation with well-defined phase signature which can be controlled. Different spectroscopic techniques (phase matching, phase cycling, and phase modulation) have been developed using a sequence of laser pulses with controlled relative phases to isolate the signal of interest by changing the wave-vector or modulation information.

The expression $E(t) = A(t)\cos(\boldsymbol{k}x - \omega_L t) = A(t)[exp(i(\boldsymbol{k}x - \omega_L t)) + exp(-i(\boldsymbol{k}x - \omega_L t)]$ describes an electric field of a propagating light beam, where

A(t) is the temporal envelope of the field; $\boldsymbol{k}$ is the wave-vector and ω_L is the carrier frequency of the light.

Phase matching can help to spatially isolate the signal of interest by changing the directions of the incident beams. The matching of the wave-vectors corresponds to the momentum conservation. If the incident beams have wave-vectors $\boldsymbol{k}_1$ and $\boldsymbol{k}_2$, the total electric field is $E(t) = \left[Ae^{-i(\boldsymbol{k}_1 x-\omega_L t)} + Ae^{-i(\boldsymbol{k}_2 x-\omega_L t)}\right] + [c.c.]$. The different second order non-linear processes induced in the non-linear crystal can be written as following:

$$\begin{aligned}\mathbf{P}_2(t) \propto E(t)^2 \propto 4 &+ [\exp\{-2i(\boldsymbol{k}_1 t + \omega_L t)\} + c.c.] \\ &+ [\exp\{-2i(\boldsymbol{k}_2 t + \omega_L t)\} + c.c.] \\ &+ 2\big[\exp\{-i\big((\boldsymbol{k}_1 + \boldsymbol{k}_2) + 2\omega_L t\big)\} + c.c.\big] \\ &+ 2[\exp(-i(\boldsymbol{k}_1 - \boldsymbol{k}_2)t) + c.c.] \; (1.15)\end{aligned}$$

where c.c. represents the complex conjugate. The terms $[\exp\{-2i(\boldsymbol{k}_1 t + \omega_L t)\} + c.c.]$ and $[\exp\{-2i(\boldsymbol{k}_2 t + \omega_L t)\} + c.c.]$ are related to second harmonic generation (SHG). The terms $[\exp\{-i((\boldsymbol{k}_1 + \boldsymbol{k}_2)t - 2\omega_L t)\} + c.c.]$ is caused by sum frequency generation (SFG). The number 4 and $[\exp(-i(\boldsymbol{k}_1 - \boldsymbol{k}_2)t) + c.c.]$ are corresponding to the optical rectification. The different non-linear process can be followed at different wave-vectors.

Ignoring the spatial dependence, the frequency can also be used to separate different non-linear signals by using phase cycling and modulation. Compared with noncollinear phase matching, collinear phase cycling enables the application on the isolated microscopic system with the dimensions smaller than the wavelength of the light. Relative phases between the pulses are controlled by pulse shapers. By forming well-chosen combinations of the measured signals with properly chosen relative phases of the pulses, the desired non-linear signals can be obtained. If the incident beams have phases ϕ_1 and ϕ_2, the total electric field is $E(t) = \left[Ae^{-i(\boldsymbol{k}x-\omega_L t-\phi_1)} + Ae^{-i(\boldsymbol{k}x-\omega_L t-\phi_2)}\right] + [c.c.]$, then the different second order non-linear processes induced in the non-linear crystal can be obtained as following:

$$\begin{aligned}\mathbf{P}_2(t) \propto E(t)^2 \propto 4 &+ [\exp\{-2i(\boldsymbol{k}t + \omega_L t + \phi_1)\} + c.c.] \\ &+ [\exp\{-2i(\boldsymbol{k}t + \omega_L t + \phi_2)\} + c.c.] \\ &+ 2[(\exp\{-i(\phi_1 + \phi_2 + 2\boldsymbol{k}t + 2\omega_L t)\} + c.c.] \\ &+ 2\big[\exp\big(-i(\phi_1 - \phi_2)\big) + c.c.\big] \; (1.16)\end{aligned}$$

Taking two-experiment phase cycles as an example, the terms $[\exp\{-2i(\boldsymbol{k}t + \omega_L t + \phi_1)\} + c.c.]$ can be eliminated by $\left\{\left(\left[Ae^{-i(\boldsymbol{k}x-\omega_L t-0)} + Ae^{-i(\boldsymbol{k}x-\omega_L t-0)}\right] + [c.c.]\right) + \left(\left[Ae^{-i(\boldsymbol{k}x-\omega_L t-0)} + Ae^{-i(\boldsymbol{k}x-\omega_L t-\pi)}\right] + [c.c.]\right)\right\}$, which can be represent as $XX - X\bar{X}$, where X and $\bar{X}$ stand for phases ϕ_1 and ϕ_2 of two incident beams as 0 and π, respectively. The terms $[\exp\{-2i(\boldsymbol{k}t + \omega_L t + \phi_2)\} + c.c.]$ can be eliminated by $XX - \bar{X}X$.

While in phase modulation, acousto-optic modulators are used to continuously sweep the relative phases of the optical fields. A Mach-Zehnder interferometer (MZI) with two acousto-optical modulators is used to manipulate the phase modulation. Each AOM acts as a Bragg cell where a longitudinal acoustic wave is propagating. The frequency of the acoustic wave is about 55 MHz. Compared with the acoustic wave velocity, the laser pulse velocity is much faster. Therefore, the AOM applies a time-varying phase shift Ωt to the pulse. The total electric field $E(t)$ is described as $E(t) = \left[Ae^{-i(\boldsymbol{k}x-\omega_L t-\Omega_1 t)} + Ae^{-i(\boldsymbol{k}x-\omega_L t-\Omega_2 t)}\right] + [c.c.]$, then the different second order non-linear processes induced in the non-linear crystal can be obtained as:

$$\begin{aligned}\mathbf{P}_2(t) \propto E(t)^2 \propto 4 &+ [\exp\{-2i(\boldsymbol{k} + \omega_L + \Omega_1)t\} + c.c.] \\ &+ [\exp\{-2i(\boldsymbol{k} + \omega_L + \Omega_2)t\} + c.c.] \\ &+ 2[(\exp\{-i(\Omega_1 + \Omega_2 + 2\boldsymbol{k} + 2\omega_L)t\} + c.c.] \\ &+ 2[\exp(-i(\Omega_1 - \Omega_2)t) + c.c.] \quad (1.17)\end{aligned}$$

where c.c. represents the complex conjugate. The terms $[\exp\{-2i(\boldsymbol{k} + \omega_L + \Omega_1)t\} + c.c.]$ and $[\exp\{-2i(\boldsymbol{k} + \omega_L + \Omega_2)t\} + c.c.]$ are due to SHG. The terms $[(\exp\{-i(\Omega_1 + \Omega_2 + 2\boldsymbol{k} + 2\omega_L)t\} + c.c.]$ are due to SFG. 4 and the terms $[\exp(-i(\Omega_1 - \Omega_2)t) + c.c.]$ are corresponding to the optical rectification. The different non-linear process can be detected at different modulation frequencies.

1.4.3 Phase modulation two-photon PL and PC microscopy

By ignoring the spatial dependence on $\boldsymbol{k}$ in the following derivation in the collinear phase modulation experiment with the same spatial dependence on $\boldsymbol{k}$, the expression can be simplified. The electric field E for a wave after the AOM can be described with the following equations

$$E_1(t) = A_1(t)(\cos(\omega_L t + \Omega_1 t)) \quad (1.18)$$

$$E_2(t) = A_2(t)(\cos(\omega_L t + \Omega_2 t)) \quad (1.19)$$

Where the A_1 and A_2 are the carrier envelopes of the pulses. Ω_1 and Ω_2 are the driving frequencies of AOMs and they are about 55 MHz which is much lower compared to the optical frequency (379 THz). The total electric field after a sequence of phase-modulated pulses can be written as,

$$\begin{aligned}E(t) &= E_1(t) + E_2(t) \\ &= [A_1(t)\cos(\omega_L t + \Omega_1 t)] + [A_2(t)\cos(\omega_L t + \Omega_2 t)] \quad (1.20)\end{aligned}$$

The intensity of the corresponding laser beam is proportional to the square of the field. Consequently, the corresponding train of the laser pulse intensity is modulated at the difference of the phase modulation frequencies ϕ=$\Omega_1 - \Omega_2$, which in our case is 50 kHz., which we name as the first harmonics (1H) in this work. The schematic diagram of the laser pulse train with the modulated intensity (2+cos (ϕt)) is presented in **Figure 1.5**. Due to the high repetition of the laser pulses, 20 pulses are used to represent the 1500 pulses in experiment in **Figure 1.5**.

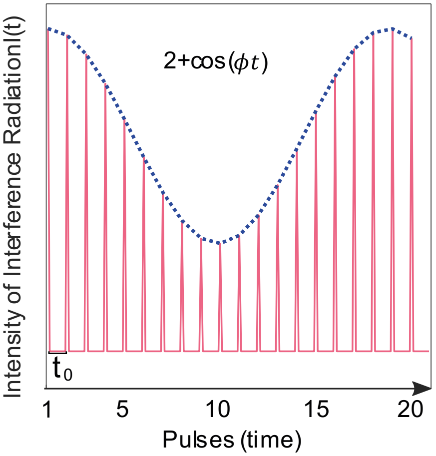

Figure 1.5
The Train of the laser pulse intensity modulated at 1H. 20 pulses are used to represent the 1500 pulses in experiment.

The probability of two-photon absorption is proportional to the light intensity square. Therefore, the excitation concentration or, in other words, population, has, besides 1H, even the second harmonic (2H) frequency present.

For the 1O recombination process, the PL emission is proportional to the population P of the electrons or holes in the CB or excitons. By expanding the fourth power of the **equation (1.20),** we can find the ratio between the amplitudes of the 1H (F1H) and 2H (F2H) components of the corresponding 1O signal as:

$$F1H\colon F2H = \frac{3}{2}\colon\frac{3}{8} = 4\colon 1 \quad (1.21)$$

The 2O recombination PL signal is proportional to the product of the population of electrons and holes, and is described as:

$$E(t)^8 = \left(E_1(t) + E_2(t)\right)^8 \quad (1.22)$$

These signals have frequency components at 1H, 2H, third harmonic (3H), and fourth harmonic (4H). And the amplitudes at these four harmonics can be represented as S1H, S2H, S3H, and S4H, respectively. After expanding the expression, the ratio of the amplitude of the 2O recombination PL at the 1H:2H: 3H:4H is

$$S1H{:}\,S2H{:}\,S3H{:}\,S4H = \frac{490}{32}:\frac{490}{64}:\frac{70}{32}:\frac{35}{128} = 56{:}\,28{:}\,8{:}\,1 \quad (1.23)$$

1.4.4 Phase modulation two-photon microscopy with charge accumulation effect

When the ground state recovery timescale is larger than the interval between the laser pulses ($t_0 \simeq 14.25\,ns$), accumulation effects leading to nonlinearities can occur.

Accumulation effects related to the ground state depleting due to slow 1O recombination process after two-photon excitation can be described as follows:

$\mathrm{P}(\sigma)$ describes the population of systems in excited state. The time evolution of the excited state population is given by the kinetic equation which consists of the relaxation and excitation by the laser pulses

$$\frac{d\big(\mathrm{P}(\sigma)\big)}{d\sigma} = -\Gamma\mathrm{P}(\sigma) + \mathrm{R}[1-\mathrm{P}(\sigma)]\sum_{n} a_n\delta(\sigma - \mathrm{n})\,,\mathrm{P}(0) = 0 \quad (1.24)$$

$\sigma \equiv \frac{t}{t_0}$ is the integer value describing the laser pulse arriving condition, and t_0 is the interval time of the two ultrafast pulses.

$\Gamma = \frac{t_0}{\tau}$ where τ is the lifetime of the 1O recombination process.

$a_n = (1 + \cos(\phi t))^2$ describes the cosine modulated pulse intensity, where the n is the pulse sequence of the laser pulse train.

$\mathrm{R}[1-\mathrm{P}(\sigma)]$ is the transition rate (R) from the VB to CB multiplied by the population of electrons in the ground state $[1-\mathrm{P}(\sigma)]$.

From 1.24, the following recurrence relation can be obtained

$$P_n = \gamma P_{n-1} + R_0 a_n(1-\gamma P_{n-1}), \qquad \mathrm{P}(0) = 0 \quad (1.25).$$

And **equation1.25** is illustrated in **Figure 1.6**. The first term of the right-hand side of the **equation 1.25** represents the part of the previous pulse excitation which has still not come back to the ground state. The second term represents the new excitation by the pulse sequence n.

$\gamma = e^{-\Gamma}$ is the exponential decay of the excited electron population, and $R_0 = s_2 I^2 \Delta t$ is the transition probability. s_2 is the estimated two-photon absorption cross-section of $MAPbBr_3$ perovskites, I is the peak intensity of the laser pulse of the length Δt.

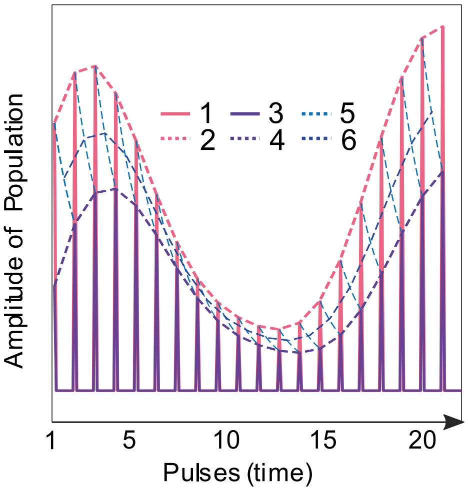

Figure 1.6
The Amplitude of the excited state population with the charge accumulation effect. The line 1 and 2 represent the amplitude and trend of the population P_n of electron or hole or excitons. The line 3 and 4 represent the population γP_{n-1} of accumulated by the previous pulse. The line 5 represents the exponential decay of the population just after each excitation. The line 6 represents the 1O recombination PL change.

We expand the **equation (1.24)** in terms of Fourier components corresponding to the harmonics 1H, 2H, 3H, and 4H with their corresponding amplitudes F1H, F2H, F3H, and F4H, respectively. The final result for the ratios of the amplitudes ($R_{\frac{F2H}{F1H}}$, $R_{\frac{F3H}{F1H}}$, and $R_{\frac{F4H}{F1H}}$) between F1H, F2H, F3H, and F4H are obtained as:

$$R_{\frac{F2H}{F1H}} = \frac{1}{4}\sqrt{\frac{\Gamma^2 + 4\tilde{\phi}^2\left(1 - 2\gamma\cos\left(2\tilde{\phi}\right) + \gamma^2\right)}{\Gamma^2 + \tilde{\phi}^2\left(1 - 2\gamma\cos\left(\tilde{\phi}\right) + \gamma^2\right)}}\left(1 - \frac{7}{2}\beta + \frac{101}{16}\beta^2\right) \quad (1.26),$$

$$R_{\frac{F3H}{F1H}} = \frac{\beta}{2}\sqrt{\frac{\Gamma^2 + 9\tilde{\phi}^2}{\Gamma^2 + \tilde{\phi}^2}\frac{1 - 2\gamma cos3\tilde{\phi} + \gamma^2}{1 - 2\gamma cos\tilde{\phi} + \gamma^2}}\left(1 - \frac{27}{8}\beta\right) \quad (1.27),$$

$$R_{\frac{F4H}{F1H}} = \frac{\beta}{16}\sqrt{\frac{\Gamma^2 + 16\tilde{\phi}^2}{\Gamma^2 + \tilde{\phi}^2}\frac{1 - 2\gamma cos4\tilde{\phi} + \gamma^2}{1 - 2\gamma cos\tilde{\phi} + \gamma^2}}(1 - 13\beta) \quad (1.28).$$

where $\tilde{\phi} = \phi t_0 = 0.000715$; $\beta = \frac{\gamma R_0}{1-\gamma}$; R_0 is the two photon transition probability; Δt is the pulse duration evaluated by the full width at half maximum (FWHM) which is about 10 fs in this present work.

We point out that since the 2O recombination process in the perovskites is fast[12], influence of the accumulation effects to the 2O expression (6) is negligible.

In the frame of the above model which consists of the 1O recombination with accumulation effects and the 2O recombination, we can express the experimental amplitudes of the four harmonic components as A1H = F1H + S1H, A2H = F2H + S2H, A3H = |-F3H+S3H|, and A4H = |-F4H+S4H|. Due to the 180° phase flip (opposite sign) of the accumulation related F3H and F4H, they will partially cancel the S3H and S4H. We summarize simplified expressions of the decomposition amplitudes of the four harmonics in **Table 1.1**.

Table 1.1
The simplified expression of the decomposition amplitude of four harmonics for 1O, 2O, and the total outcomes of 1O and 2O recombination processes are presented here.

	A1H	A2H	A3H	A4H
1O	F1H	F2H	F3H	F4H
	F1H*1	F1H*$R_{\frac{F2H}{F1H}}$	F1H*$R_{\frac{F3H}{F1H}}$	F1H*$R_{\frac{F4H}{F1H}}$
2O	S1H	S2H	S3H	S4H
	S4H*56	S4H*28	S4H*8	S4H*1

The simulated time and frequency domain data with four harmonics originating from 1O and 2O recombination are visualised separately and a sum in **Figure 1.7**. The transition rate is set to 0.01 and the ground state recovery timescale is set to 300 ns. **Figure 1.7 (a)** shows the simulated time domain data with F1H, F2H, F3H, and F4H components labelled as blue, red, purple and orange dotted lines, respectively. The relationships between amplitudes of these four components is given in the **Table 1.1**. The simulated time domain intensity due to the 1O recombination process with four harmonics is plotted as the inset in **Figure 1.7 (d)**, marked with blue colour. The corresponding Fourier transform with the amplitudes F1H, F2H, F3H, and F4H are plotted in **Figure 1.7 (d)**, marked with blue colour.

Similarly, **Figure 1.7 (b)** shows the simulated time domain data for the 2O recombination. The relationships between amplitudes of these four components follows **equation (1.23)**, 56:28:8:1. The sum of the different components for the 2O recombination is plotted as the inset in **Figure 1.7 (e)**, marked with red colour. The simulated frequency domain data with S1H, S2H, S3H, and S4H are plotted in **Figure 1.7 (e)**, marked with red colour.

Figure 1.7 (c) shows the simulated time domain combined outcomes of 1O and 2O recombination processes with A1H, A2H, A3H, and A4H components labelled as blue, red, purple and orange dotted lines, respectively. Due to the 180° phase flip (opposite sign) of the accumulation related F3H and F4H, they will partially cancel the S3H and S4H. The resulting A3H is the absolute difference of S3H and F3H, and A4H is the absolute difference of S4H and F4H. The time domain combined outcome of 1O and 2O recombination processes with four harmonics together is plotted as the inset in **Figure 1.7 (f)**, marked with green colour. In addition, the simulated frequency domain data with A1H, A2H, A3H, and A4H are plotted in **Figure 1.7 (f)**, marked with green colour.

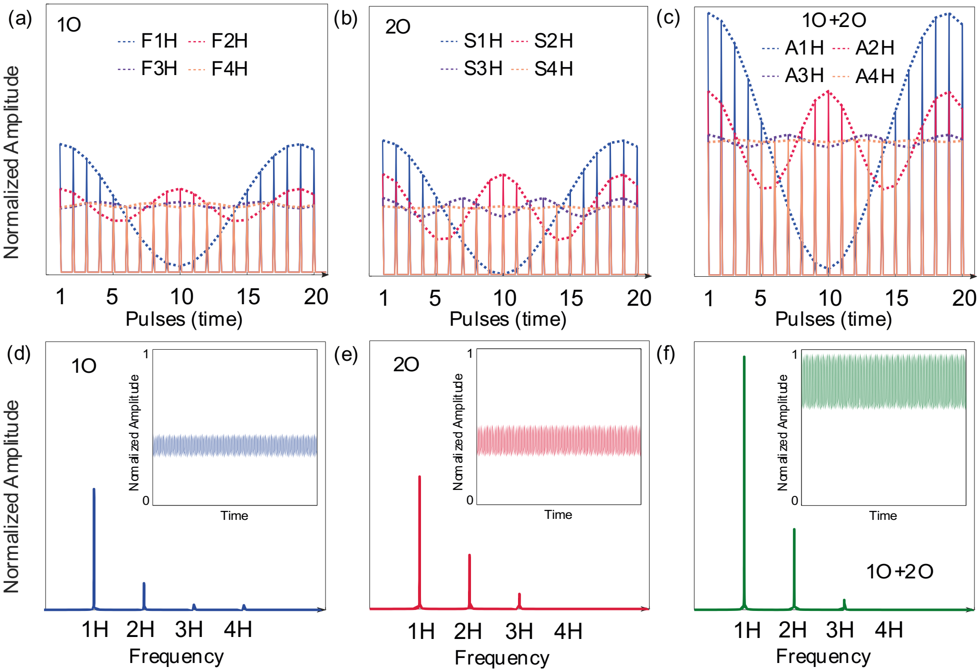

Figure 1.7
(a-c) Simulated time domain signal of 1O, 2O, 1O+2O recombination process. (d-f) Simulated frequency domain signal of 1O, 2O, 1O+2O recombination process.

The discrete Fourier transform of the raw data is carried out using a fast Fourier transform (FFT) algorithm with MATLAB software. The modulus $|a + bi| = \sqrt{a^2 + b^2}$ of the Fourier transformed complex numbers show modulation amplitudes at 1H, 2H, 3H, and 4H frequencies as A1H, A2H, A3H, and A4H, respectively. We point out that the data used here partially overlap with the raw data in our previous work[13] where we separate PL from excitons and free charges in $MAPbBr_3$ perovskite crystals using two-photon phase-modulated PL spectroscopy.

At room temperature, the average amplitudes of A3H and A4H are 2.4362 and 0.3189, respectively. The amplitude of A4H is low and significantly disturbed by electronic noise. Therefore, only A1H, A2H, and A3H are used for further analysis.

The following relations follow the above description of 1O+2O:

A1H=F1H+S1H, (1.29)

A2H=F2H+S2H, (1.30)

A3H=|-F3H+S3H|, (1.31)

F2H=F1H*$R_{\frac{F2H}{F1H}}$, (1.32)

F3H= F1H*$R_{\frac{F3H}{F1H}}$, (1.33)

S1H:S2H: S3H=7:3.5:1. (1.34)

The experimental A1H, A2H, and A3H at each image pixel and temperature were fitted to the model by using nonlinear least-square analysis (Levenberg-Marquardt method) as implemented in Matlab. The fitting has three independent parameters (F1H, S1H, and the lifetime of the 1O recombination) based on the set of **equations (1.29)-(1.34).** As the results, the F1H, F2H, F3H, F4H, S1H, S2H, S3H, S4H, and time scale of 1O recombination process (τ) at each pixel and temperature can be obtained. Besides, the relative error of A1H, A2H, and A3H can be calculated as,

$$R_{err\_1H} = \frac{(\mathrm{F1H} + \mathrm{S1H}) - \mathrm{A1H}}{\mathrm{A1H}}, (1.35)$$

$$R_{err\_2H} = \frac{(\mathrm{F2H} + \mathrm{S2H}) - \mathrm{A2H}}{\mathrm{A1H}}, (1.36)$$

$$R_{err\_1H} = \frac{|\mathrm{F3H} - \mathrm{S1H}| - \mathrm{A3H}}{\mathrm{A1H}}. (1.37)$$

Chapter 2 Experimental methods

2.1 Sample preparation

2.1.1 Synthesis of $MAPbBr_3$ microcrystal and thin film

$MAPbBr_3$ microcrystal was synthesized according to the method described by Kojima et al[13,14,35,85]. The precursor was obtained by dissolving 21.12 g MABr (Dyenamo, purity > 98 %, ~ 0.01 mol) and 3.67 g $PbBr_2$ (Sigma-Aldrich, purity ≥ 98%, ~ 0.01 mol) in 10 mL N, N-Dimethyl formamide (Sigma-Aldrich, purity ≥ 99 %). Subsequently, about 100 µL precursor was pipetted onto the glass substrates which were washed by acetone in an ultrasound machine. By heating the substrates at around 80 ℃, the solvent was completely evaporated, leading to the formation of microcrystals. The $MAPbBr_3$ thin film was obtained by spin coating a 5 µL precursor on the glass substrate surface at a speed of 4000 rpm. To ensure the sample conductivity during the SEM measurement, a 5 nm Pd/Pt layer was coated on the perovskite crystals using Q150t ES metal sputter coater. High-resolution scanning electron microscope (SEM, Hitachi S4800) images were obtained to observe the morphology distribution.

2.1.2 Synthesis of $FAPbBr_3$ nanocrystals

0.2 mmol lead acetate trihydrate (Aldrich, purity 99.99 %), 0.75 mmol formamidinium acetate (0.078 g,), 2 mL oleic acid (Sigma, purity 90 %), 3 mL 1-octadecene (ODE, Sigma, purity 90 %,) were placed in a three neck round bottom flask to obtain the precursors. The mixture was heated up to 100 ºC for 30 minutes under vacuum to remove any impurity and water in the precursors. 0.6 mmol OLAmBr in 2 mL toluene (Merck, sonicated to dissolve) was swiftly injected when the temperature reached 130 ºC. During the reaction, N_2 was backfired to the system. The reaction flask was dipped into an ice-water bath to rapidly cool down the reaction mixture for 30 s. Then, the reaction product was dispersed in the mixture of toluene and acetonitrile with 1:1 ratio and centrifuged at 12000 rpm. The upper supernatant part was discarded, and the precipitate part was dispersed in toluene and centrifuged at 2000 rpm again. The supernatant part was collected in a separated vial and stored in refrigeration for further utilizations.

2.1.3 $MAPbBr_3$ solar cell fabrication

The glass substrate coated with fluorine-doped tin oxide (FTO) was purchased from Sigma Aldrich, USA. Zinc powder (Merck, USA) and 2 M HCl were used to etch the substrates and form the electrode pattern (2 mm × 25 mm, W × L). These patterned substrates were then cleaned in an ultrasonic bath with detergent (5 % labolene), de-ionized water, acetone, isopropyl alcohol (IPA), and ethanol for 20 minutes, respectively. To remove the organic residuals, these cleaned substrates were treated with UV light for 15 min. The TiO_2 layer was prepared by spin coating PMT-20 (Dyesol, Australia) at 3000 rpm for 60 s. Subsequently, the TiO_2 coated substrates were sintered at 500 °C for 60 min at a heating ramp rate of 10 °C/min. Then the $MAPbBr_3$ layer was coated on the top of FTO/TiO_2 by spin casting at 3000 rpm for 200 s. The obtained substrates were annealed on a hotplate at 100 °C for 2 min inside the glove box. The hole transporting layer poly (3-hexylthiophene 2-5, diyl) (P3HT) (Sigma Aldrich) was deposited by spin casting at 3000 rpm for 30 s on $FTO/TiO_2/MAPbBr_3$ substrate using the solution with 15 mg P_3HT in 1mL toluene. In the end, the golden back contact was deposited using thermal evaporation under the pressure of 2×10^{-6}. The active area was about 0.02 cm^2. The OAI solar simulator (USA) consisting of Keithley 2400 source measuring unit was used to record the photovoltaic current-voltage performance.

2.1.4 $MAPbBr_3$ based photodetector fabrication

The $MAPbBr_3$ detector was fabricated by covering the substrate with several microcrystals after the fast crystallization and annealing process. The glass substrates were coated with ITO contacts (5 μm channel width and 1000 μm length). Then, the single $MAPbBr_3$ microcrystal based photodetector can be characterized by contacting the two ITO electrodes.

2.1.5 GaAs p-i-n diode

The GaAs p-i-n diode was purchased from Kyosemi Co. LTC with the part nr. KPDG008. The active area of this diode is about 80 × 80 μm^2. A classic AAA solar simulator (OAI Trisol) fitted with AM1.5 (air mass) filter was used to simulate the solar irradiation and it was calibrated using a standard Si solar cell. All the devices were characterized under ambient conditions. Under 100 mW/cm^2 illumination, the cell has a short circuit current density of 88.90 mA/cm^2, open circuit voltage of 0.93 V, and a fill factor of 84.07 %. The external quantum efficiency of the device at 790 nm (excitation wavelength) is about 78 %[86].

2.2 Experimental Section

2.2.1 Optical setup

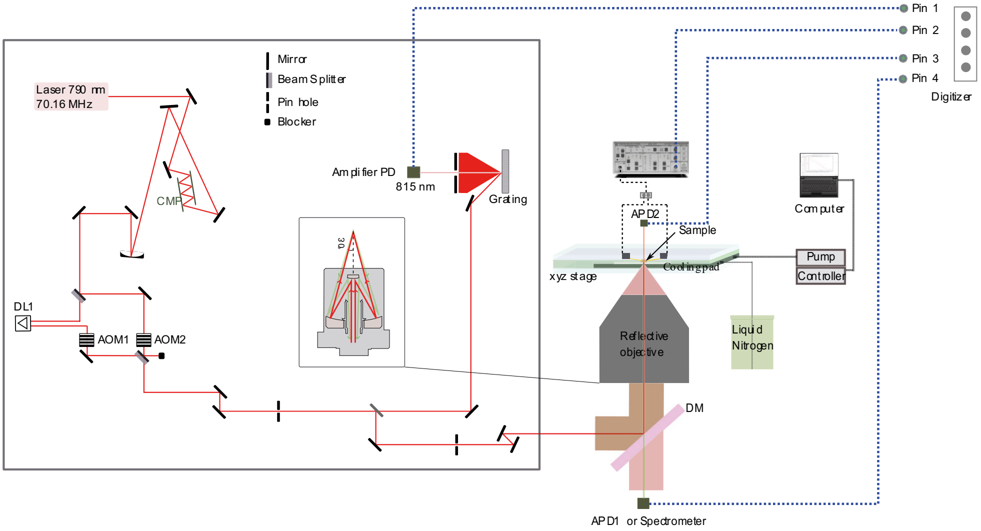

Figure 2.1
The schematic of the setup, with CMP (Chirp mirror pair), AOM (Acousto-optic modulator), DL (Delay line), PD (photodiode), APD (Avalanched photodiode), DM (Dichroic mirror), Pre-AMP (Preamplifier).

The schematics of the setup is shown in **Figure 2.1**. A Ti:sapphire oscillator (Synergy, Femtolasers) provides 8-20 fs pulses at 70.16 MHz repetition rate. The group-velocity dispersion induced by the different optical elements is pre-compensated by a pair of chirped mirrors (CMP). The Mach-Zehnder interferometer (MZI) includes two beam splitters (BS), two totally reflecting mirrors, and two acousto-optic modulators. The beam splitter splits the laser pulses into two equal replicas with equal intensity. The phases of the electric filed of the two replicas are swept using acousto-optic Bragg cells (AOM). The two AOMs are driven by two radio frequency generators at different frequency. The tunable delay line is placed in front of one of the beams to control the temporal overlap of the two beams. The two pulses with precise time delay and phase difference are finally brought together collinearly using the other beam splitter. One of the outputs from the MZI is directed to a 1200 l/mm grating. A narrow frequency range of the reference is selected by fixing a slit at the wavelength of 815 nm. The selected reference is detected by an amplified photodiode. The other output of the BS is alligned to an inverted microscope (Nikon Ti-S). Subsequently, a reflective objective (RO) is used to focus the laser beam onto the sample. The sample is placed in a temperature-controlled stage which is fixed on a three dimensional piezo-driven scanner (Nano-LP Series, Mad City Labs).

The fluorescence signal emitted by the sample is collected with the same objective and directed to an avalanche photodiode (APD1) (LCS A3000-01, Laser Components) or a spectrometer (Flame, Ocean Optics). A dichroic mirror (FF670-SDi01-25x36, Semrock) is used to separate the two-photon excited PL signal from the incident light. The transmitted laser beam is filtered out from the PL generated from the top side of the sample by a long-pass filter with cut-off wavelength at 600 nm. Then the transmitted laser signal is directed to the APD2. The PC is amplified by a pre-amplifier (SR570, Stanford Research Systems).

The signal from the amplified PD (reference signal), pre-amplifier (PC signal), APD2 (transmitted laser beam), and APD1 (fluorescence signal) can be digitized simultaneously by the pin 1, 2, 3, and 4, respectively, of the digitizers at different speed for different data acquisition time in different experiments.

2.2.1.1 Femtosecond Laser source

In order to get the nonlinear signal from the investigated material, the optical excitation with 10^{-14} s pulses is used to provide a much higher top intensity than what would be possible with continuous wave or longer pulses.

The shape of the laser pulse can be described as a Gaussian function. The relationship between the spectral bandwidth and duration of the laser pulse can be written as:

$$\Delta \upsilon \Delta t \geq K \ (2.1),$$

where $\Delta \upsilon$ is the frequency bandwidth of the laser pulse as full-width at half-maximum (FWHM). Δt is the temporal length of the laser pulse as FWHM, and K is a number only dependent on the pulse shape and it is 0.441 for a Gaussian pulse.

The frequency ν can be obtained as the **equation (2.2)**,

$$\nu = \frac{c}{\lambda} \ (2.2).$$

In the equation, c is the light speed in vacuum, $3.0*10^8$ m/s. ν is the frequency and λ is the wavelength of the light.

The differential of the above equation leads to

$$\Delta \nu = -\frac{c\Delta\lambda}{\lambda^2} \ (2.3).$$

Therefore, the time-frequency relationship can be rewritten as

$$\Delta t \geq K\frac{\lambda_0^2}{\Delta\lambda * c} \ (2.4).$$

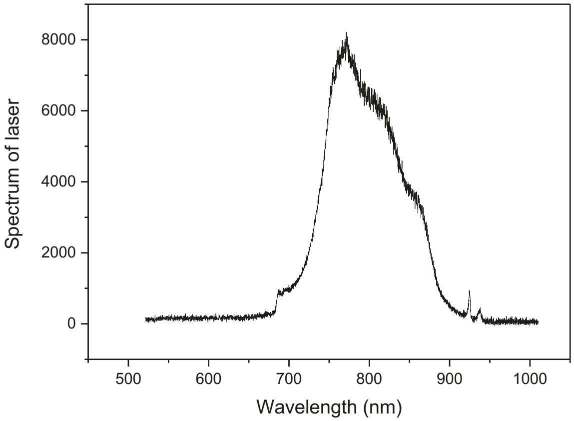

Figure 2.2
The spectrum of optical lasers used in this thesis work.

Figure 2.2 shows the spectrum of the optical laser in this thesis. By fitting with the Gaussian function, the central wavelength is obtained to be about 790 nm, and the FWHM is about 114.5 nm. Thus, $\Delta t \geq K\frac{\lambda_0^2}{\Delta\lambda * c} = 0.441 * \frac{790nm*790nm}{114.5nm*3.0*10^8\frac{m}{s}} \approx 8\,fs.$

2.2.1.2 Acousto-optic modulator

Acousto-optic effect or acousto-optic diffraction is the interaction between optical light and acoustic waves. This phenomenon was predicted firstly by Brillouin and experimentally demonstrated by Lucas, Biquard and Debye, Sears in 1932[87–89]. The acousto-optic interaction is a photo-elasticity effect change by applying mechanical strains. The strains are generated by the acoustic wave produced in a transparent medium by a radio frequency (RF) generator. The acoustic wave can be taken as a wave of refractive index variations that can be expressed as $\mathrm{n}(z,t) = n + \Delta n\, cos(2\pi ft - Kz)$ and used to describe the plane acoustic wave propagating along z axis, where f and K represent the frequency and propagation constant, respectively; n and Δn represent the undisturbed refraction index and the amplitude variation of the refractive index induced by the acoustic wave.

Considering the light diffraction effect by a monochromatic acoustic wave, two limiting regimes, namely Raman-Nath and Bragg, are expected and shown in **Figure 2.3 (a)** and **(b)**, respectively. The regimes are determined by the quality factor Q[90] (**equation 2.5**).

$$Q = \frac{2\pi\lambda_L L}{n\lambda^2}, (2.5)$$

Where λ_L is the wavelength of the laser beam 790 nm; λ is the acoustic wavelength $= \frac{v}{f} = \frac{5900\ m/s}{55*10^6/s} = 107.3\ \mu m$; L is the distance of the laser beam travels through the acoustic wave.

The Raman-Nath regimes can be observed at quality factor << 1. As a result, the diffraction pattern contains many diffraction orders and the light intensity is symmetrically distributed. For the Bragg region, the quality factor >> 1. And there are only two diffraction orders in the diffraction pattern.

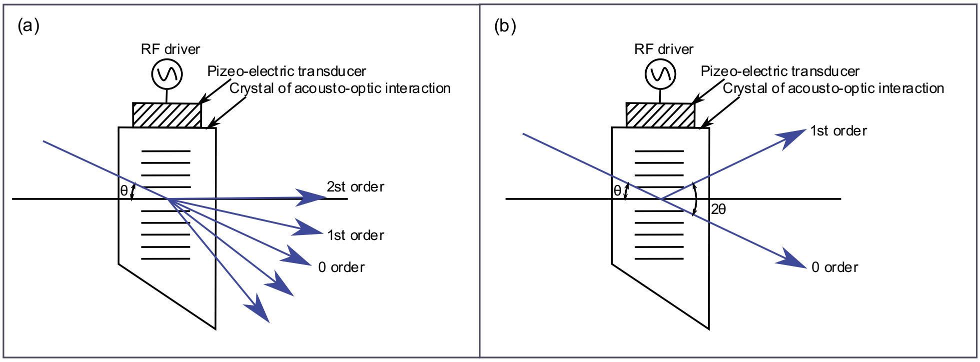

Figure 2.3
The working principle of an acousto-optic modulator in a Raman-Nath (a) and Bragg (b) regimes.

The acousto-optic modulators purchased from Gooch&Housego with model number 35022-1-8 are used in this thesis. The interactive material in the AOM is fused silica, with an operating wavelength range in 600 – 900 nm and the operating frequency is about 55 MHz. A RF signal is applied to a piezo-electric transducer, which is bound to the fused silica, and an acoustic wave will be generated. This acoustic wave acts as a phase grating traveling through the crystal at a speed of 5.9 km/s and with an acoustic wavelength $\lambda = \frac{v}{f} = \frac{5900\ m/s}{55*10^6/s} = 107.3\ \mu m$, which strongly depends on the frequency of the RF signal.

The Bragg angle θ represents the incidence angle and it can be calculated as:

$$sin\theta = -\frac{\lambda f}{2nv} \quad (2.6),$$

where λ is the optical wavelength (790 nm); f is the acoustic frequency (55 MHz); n is the refractive index for the light (1.46 for the fused silica); v is the acoustic wave velocity in the crystal (5.9 km/s). Therefore, θ is about 0.005 degree which gives efficient diffraction larger than 85%.

2.2.1.3 Reflective objective--Schwarzschild reflector

When a broad band femtosecond laser pulse transmits through a dispersive medium, the group velocity dispersion occurs[91]. Therefore, the reflective objectives do not experience chromatic effect and perform better for such laser pulses with an extremely broad band, compared with the refractive optics.

The reflective objective (RO, 36X/0.5 NZ, Edmund Optics) in an inverse Cassegrain configuration or Schwarzschild configuration is used to focus the laser beam onto the sample. The diagram of a typical reflective microscope objective is shown is **Figure 2.4**. The laser pulse train passes through the aperture hole and the primary concave mirror, then to the secondary convex mirror. Subsequently, the laser beam was reflected, diverged by the secondary mirror, and reflected back by the primary mirror subsequently. In the end, the beam is focused by the primary mirror to the focal point with an angle of 30° (NA=0.5). The PL signal emitted from the sample is also collected by the primary mirror. Further on, the PL signal is guided out from the aperture hole after reflecting by the secondary mirror.

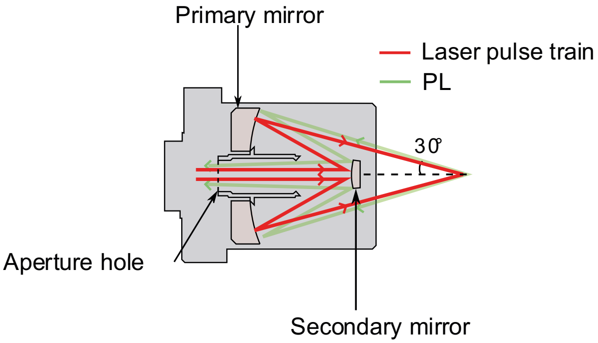

Figure 2.4
The diagram of the reflective microscope objective.

The minimum diameter of focusing spot is dependent on the NA of the objective and the laser wavelength. Therefore, the minimum spot diameter can be calculated as: Minimum spot diameter = $1.22\frac{\lambda}{NA} = 1.22 * \frac{790\ nm}{0.5} = 1.927\ \mu m$ (2.7).

Due to the two-photon excitation, the focal spot is even smaller (section 1.3.1).

2.2.1.4 Digitizer

To capture and process data at a high speed, the Alazartech's ATS9870 and ATS9440 digitizers were used.

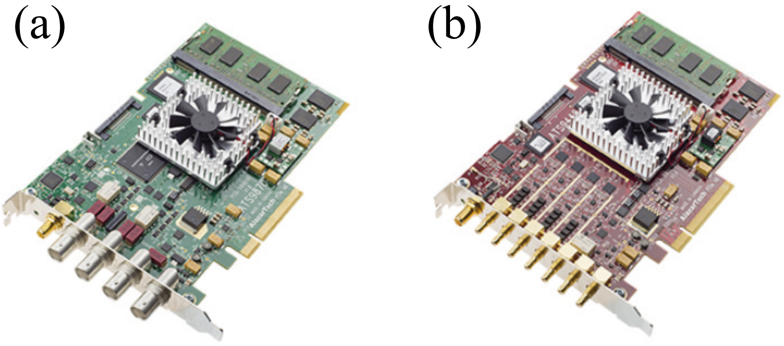

Figure 2.5
(a) Alazartech's ATS9870 and **(b)** Alazartech's ATS9440

The Alazartech's ATS9870 digitizer is a dual-channel digitizer and is shown in **Figure 2.5 (a).** The digitizer provides two 8-bit analog to digital converters (ADC) channels which enable simultaneous sampling of 2 or 1 channel with a maximum sampling rate of 1 GSa/s. Each 8-bit sample is stored in 1 byte. Therefore, the maximum acquisition data rate at 1 GSa/s is given by:

1 GSa/s *2 channels*1 byte per sample = 2 GB/s.

The Alazartech's ATS9440 digitizer is a Quad-channel digitizer and is shown in **Figure 2.5 (b)**. The digitizer provides four 14-bit ADC channels which enable the simultaneous sampling of 4, 2, or 1 channel with a maximum sampling rate of 125 MSa/s. Therefore, the maximum acquisition data rate at 125 MSa/s is given by:

125 MSa/s*4 channels*2 bytes per sample = 1 GB/s.

2.2.1.5 Temperature-control system

A temperature-control system (Linkam Scientific Instruments, LTS420E-P) is used to vary the sample temperature from -195 °C to 420 °C. This temperature-control system is designed with low level of noise and vibrations. The whole system is automatically controlled by the T96 controller. A platinum sensor is embedded near the surface of a temperature-controlled stage (53.5 mm x 43 mm) for accurate temperature control. The temperature can be detected by simply placing the sample on the stage and contact the appropriate points manually on the sample. Liquid nitrogen is used to control the stage temperature at linear cooling rate as fast as 100 °C/min or as slow as 0.01 °C/min.

2.2.2 Data acquisition and analysis

The generalized lock-in amplifier technique is used in the data acquisition and analysis process[92].

2.2.2.1 Data acquisition with phase modulation technique

We take one measurement as an example. The PL and PC from the solar cell with applied forward 2V bias are acquired using the digitizer ATS9440. The data on all four channels are acquired, where channel A, channel B, channel C, and channel D are PL signal, reference, reference, and PC signal, respectively. The preamplifier is set as 1 mA/V. Channel A is DC coupled with 100 mV range. Channel D is coupled with 400 mV range. Channel B and C are AC coupled with 100 mV range. The data acquisition rate (F_s) is 10 MSa/s and acquisition time (t) is 0.05 s (50 ms). The modulation frequency is 3 kHz. The total number of data points N in each channel is calculated as:

$N = F_s * t = 10 \frac{MSa}{s} * 0.05\ s = 5 * 10^5$ (2.8).

For each channel, there are $5 * 10^5$ data points. The acquired time domain data points are $4 * N = 2 * 10^6$.

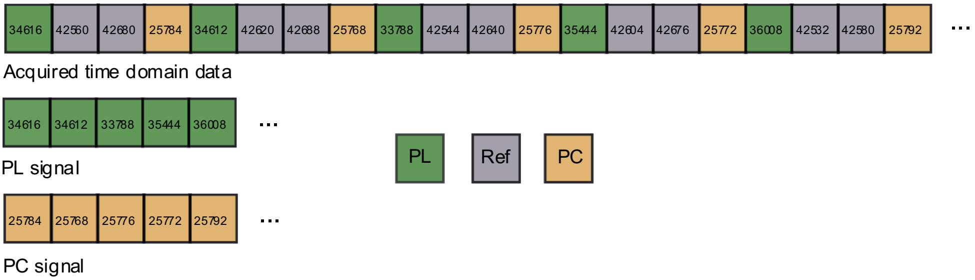

Figure 2.6
The acquired data for 4 channels and they are PL, Ref, Ref, and PC, respectively. The green blocks represent the PL channel, the grey blocks represent the Ref channel, and the orange blocks represent the PC channel.

The raw data of the signal is a binary file in a time domain and shown in **Figure 2.6**. The four channels are digitized subsequently and written into the binary file. The PL, Ref and PC data can be obtained by selecting the 1st, 2nd or 3rd, and 4th datapoints in each block which contains four data points.

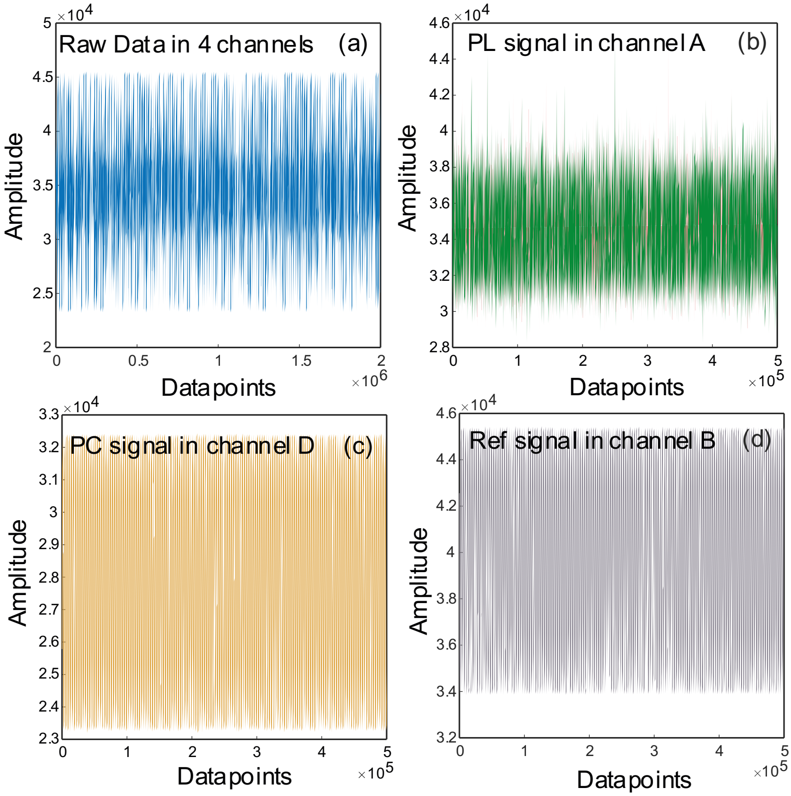

Figure 2.7

The plot of the time domain raw data. (a) raw time domain data which contain $2 * 10^6$ data points in four channels. (b) the selected PL data which contain $5 * 10^5$ data points in channel A. (c) the selected PC data which contain $5 * 10^5$ data points in channel D. (d) the selected Ref data which contain $5 * 10^5$ data points in channel B.

The time domain raw data of the solar cell with the applied forward bias +2 V consisting of four channels information are shown in **Figure 2.7 (a).** The selected PL raw data in channel A are shown in **Figure 2.7 (b)**. The plot of the PC raw data in channel D is shown in **Figure 2.7 (c)**. The reference raw data in channel B are shown in **Figure 2.7 (d)**. All the data points are 16 bits. The range from 1 to 2^{16}represents the range from -100 mV to 100 mV. For channel A, the amplitude of the signal in mV is obtained as,

$$y_{PLmV} = \frac{(x-2^{15})*100}{2^{15}} \quad (2.9).$$

For channel B, the amplitude of the signal in mV is obtained as,

$$y_{RefmV} = \frac{(x-2^{15})*100}{2^{15}} \quad (2.10).$$

For channel D, the amplitude of the signal in mV is obtained as,

$$y_{PCmV} = \frac{(x-2^{15})*400}{2^{15}} \quad (2.11).$$

The total PL and PC signal containing modulated signal and dark background can be calculated as:

$$y_{PL} = \frac{\sum \frac{y_{PLmV}}{y_{RefmV}}}{5*10^5}, \text{ and } y_{PC} = \frac{\sum \frac{y_{PCmV}}{y_{RefmV}}}{5*10^5}.$$

The calculated $y_{PL} = 0.3498$, and $y_{PC} = -2.6058$. The negative value of PC means that the photo-induced PC direction is opposite to the applied forward dark current.

To extract the PL and PC signal, the discrete Fourier transform (DFT) is carried out on the data set of each channel using a fast Fourier transform (FFT) algorithm with MATLAB software. The modulus $|a + bi| = \sqrt{a^2 + b^2}$ of the Fourier transformed complex numbers show the modulations at different frequencies. The frequency can be calculated as:

$$F_n = \frac{(n-1)*F_s}{N} \quad (2.12),$$

where F_n is the frequency of the n-th point; n is the number in the signal sequence in time domain; F_s is the sampling rate; N is the total digitized data points.

The modulation signal at first harmonic (1H) is located at the 151th data point based on the above equation. The modulation 1H signal of PL is $8.18 * 10^7$ and that of PC is $1.13 * 10^9$.

2.2.2.2 Laser repetition rate validation

The repetition rate of the laser pulse train can be validated by the following example. The PL from FAPbBr$_3$ nanocrystals is acquired by the digitizer ATS9870. Only one channel is used with 40 mV range. The data acquisition rate is 1 GSa/s and acquisition time is 0.001 s (1 ms). By applying the Fourier transform on the time domain data shown in **Figure 2.8 (a),** the signal at 70.16 MHz (1H) and signals at overtones frequencies, such as 140.32 MHz (2H), 210.49 MHz (3H) and 280.65 MHz (4H) can be obtained and shown in **Figure 2.8 (b)**. It can be seen that the repetition rate of the laser pulse train is about 70.16 MHz**.**

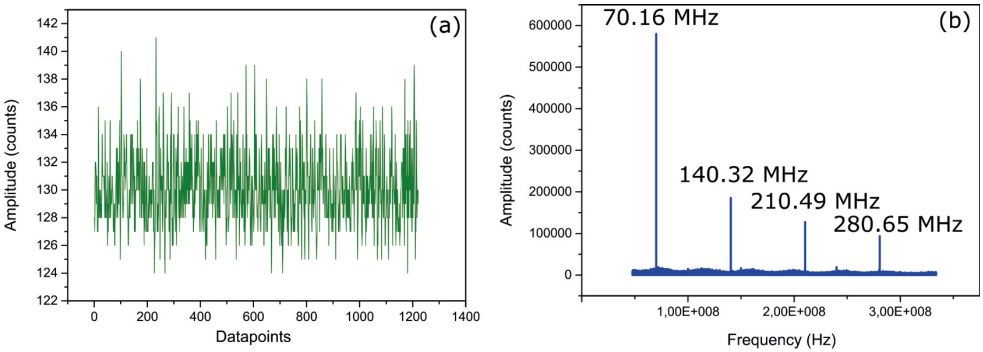

Figure 2.8

The frequency of laser. (a) the two-photon PL of $FAPbBr_3$ nanoparticles and digitized at a speed 1GSa/s (1 Giga sample per second) for about 1 ms. And there are 1048576 datapoints in total. (b) the Fourier Transform of the time domain 2PPL spectrum. And the signal at 70.16 MHz is the laser frequency.

Chapter 3 Carrier-phonon scattering in $MAPbBr_3$ and $FAPbBr_3$ perovskite

The hot carrier, created by the photoexcitation with energy well above the band edge, can be cooled down via carrier-phonon scattering. The strength of the carrier-phonon coupling can be investigated via analysing the temperature-induced PL spectral linewidth broadening[34,35]. The analyses are made difficult by other sources of line broadening like the coexistence of multiple structural phases. Therefore, it is necessary to proceed the PL spectral imaging and the PL corresponding to different phases can be separated and individually resolved, which is important for perovskite applications in optical and optoelectronic devices.

3.1 Carrier-phonon scattering of $MAPbBr_3$ with different phases

$MAPbBr_3$ is typically more stable than the iodine (I) counterpart and it is easy to grow. Three different phases (CU, TE, and OR) are prevalent in $MAPbBr_3$ bulk crystals (BCs). Many studies have shown that the temperature related phase transition in $MAPbBr_3$ bulk crystals significantly influences the optical properties[93–97]. The PL spectrum peak at 2.22 eV is mainly contributed by TE phase at room temperature[98], while the PL spectrum peak at 2.24 eV was originated from the OR phase below 160 K[99]. Besides，the carrier-phonon scattering does affect the hot carrier mobility a lot[49,51,100]. Therefore, in this chapter, we use the temperature dependent two-photon PL to investigate the influence of the different phases on the carrier-phonon scattering and identify how it influences the carrier mobility in $MAPbBr_3$ thin films (TFs) and BCs.

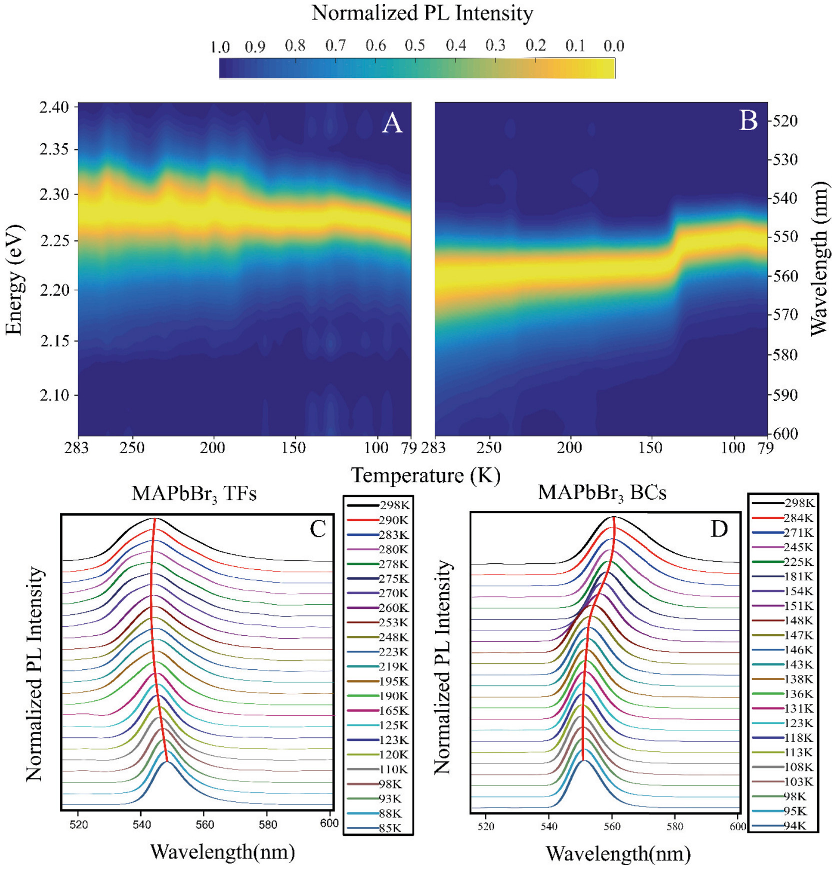

Figure 3.1

Temperature dependent PL spectra of (A) $MAPbBr_3$ TF. (B) $MAPbBr_3$ BC. (C) and (D) show normalized PL spectra of $MAPbBr_3$ TF and BC, respectively, at some selected temperatures.

Temperature dependent PL spectra of $MAPbBr_3$ TFs and BCs are shown in **Figure 3.1 (A)** and **(B)**. The normalized PL spectra of the TFs and BCs are shown in **Figure 3.1 (C)** and **(D)**, respectively. The PL spectra are fitted with three Voigt components centered at 2.22, 2.28, and 2.31 eV corresponding to TE, OR, and CU phases, respectively. At room temperatures, the main peaks for $MAPbBr_3$ TFs and BCs are centered at 544 nm (2.28 eV, OR phase) and 558 nm (2.22 eV, TE phase), respectively. The peak at 2.28 eV which comes from the OR phase at room temperature is the main component providing 63% of the PL spectra. The slight blue shift of 2.28 eV compared with 2.24 eV of the OR components at low temperature is mainly due to shift of the balance of equilibrium from mainly free charge carriers at room temperature to excitons at low temperature. At 79 K, the peak is at 2.246 eV corresponding to the OR phase for both $MAPbBr_3$ BCs and TFs.

With decreasing temperature, there is a continuous red shift in the PL spectra of the $MAPbBr_3$ TFs. This can be explained by the increased population of the excitons and decreased population of free charge carriers. The balance between excitons and free charges is usually described by the Saha-Langmuir **equation (1.1)**. This is different from the red shift due to the reabsorption because the PL is collected in the epi-direction. In contrast to the $MAPbBr_3$ TFs, an abrupt blue shift from 560 nm to 552 nm is observed in the $MAPbBr_3$ BCs with temperature decreasing from about 160 K to 140 K , suggesting a phase transition from TE to OR phase [32].

Besides, the free charge carrier – phonon coupling, exciton – phonon coupling has a significant influence on the PL linewidth broadening[94,101,102]. As demonstrated in **Figure 3.1**, the PL spectra show a broader linewidth at room temperature and a narrower one at 79 K for both $MAPbBr_3$ TFs and BCs. The relationship between the linewidth of the PL spectra and charge carrier coupling can be described as,

$$\Gamma(T) = \Gamma_0 + \Gamma_{ac} + \Gamma_{LO} + \Gamma_{imp} \quad (3.1)$$

$$\Gamma_{ac} = \gamma_{ac} T \quad (3.2)$$

$$\Gamma_{LO} = \gamma_{LO} N_{LO}(T) = \gamma_{LO} \frac{1}{e^{\frac{E_{LO}}{K_B T}} - 1} \quad (3.3)$$

$$\Gamma_{imp} = \gamma_{imp} e^{-\frac{E_B}{K_B T}} \quad (3.4),$$

where Γ_0 is the temperature-independent inhomogeneous broadening due to the disorder and inperfections[103,104]; Γ_{ac} and Γ_{LO} are the homogeneous broadening resulting from the acoustic and the LO phonons with coupling strength γ_{ac} and γ_{LO}, respectively; Γ_{imp} is the inhomogeneous broadening because of the ionized impurities; γ_{imp} is the contribution part to the PL line width broadening when the impurities are fully ionized; and E_B is the average binding energy of the impurities[103,105]. Besides, $N_{LO}(T)$ is the occupation of the respective phonons given by Bose-Einstein distribution function $N_{LO} = \frac{1}{e^{\frac{E_{LO}}{k_B T}} - 1}$, where E_{LO} is the energy of the LO phonons and k_B is the Boltzmann constant.

To extract the coupling strength with the LO phonons and acoustic phonons, two separate temperature regions are selected according to the obviously different energies of two kinds of phonons. The energy of the acoustic phonon is less than 2.5 meV, while the energy of the LO phonon is about 15.3 meV[101]. For temperatures lower than 100 K, the LO phonon occupation is negligible as the thermal energy is only about 7 meV. Therefore, only the acoustic phonons are prevalent and contribute to the linewidth broadening at temperatures lower than 100 K, while the LO phonons start playing a role when the temperature is above 200 K. In addition to the different phonon types, the coupled excited species are different as well. At higher temperatures (200 - 298 K), we mainly have free charge carriers and consequently coupling between the LO phonon and free charge carriers is the dominating source for the line broadening. At low temperature, however, the balance shifts towards the excitons and therefore below 100 K mainly the coupling between the acoustic phonon and excitons determines the line broadening. Both phonon-carrier/exciton couplings in different $MAPbBr_3$ TFs and BCs samples are shown in **Figure 3.2.** The related linewidth parameters are extracted according to **equations (3.1 - 3.4)** and the results are presented in **Table 3.1**. In the fitting we have included the scattering by the impurities, and found that the corresponding contribution to the broadening is negligible[101,106]. The exciton acoustic phonon coupling strength is about 21 meV/K for both samples as they are in the same phase at low temperature. The free charge carrier LO phonon coupling strength is about 52 meV in the $MAPbBr_3$ TFs with OR phase and about 24 meV in the $MAPbBr_3$ BCs with TE phase. The 2.2 times difference in the coupling constants in different phases can result in significant difference in the carrier mobility based on the Feynman-Ösaka model, where the carrier mobility is inversely proportional to the LO phonon coupling strength. Therefore, it is suggested that the transition from the OR phase to the TE phase at room temperature can improve the photovoltaic performance of the $MAPbBr_3$ TFs if the sample degradation by the external effect is inhibited.

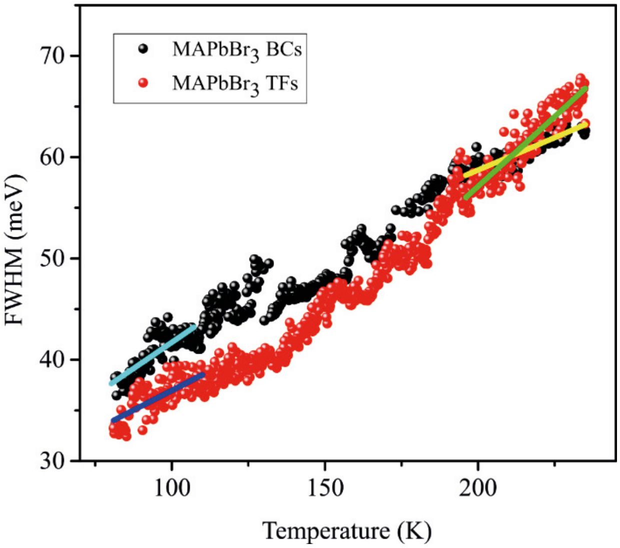

Figure 3.2
Temperature dependent linewidth of $MAPbBr_3$ TFs (red color) and BCs (black color). Four regions with blue line, green line, cyan line and yellow line demonstrate the exciton-acoustic phonon coupling, free charge carrier-LO phonon coupling in TFs and BCs, respectively.

Table 3.1
Extracted linewidth parameters

Sample	TFs				BCs			
MAPbBr$_3$	$\Gamma_{0(ac)}$ (meV)	γ_{ac} (meV/K)	$\Gamma_{0(LO)}$ (meV)	γ_{LO} (meV)	$\Gamma_{0(ac)}$ (meV)	γ_{ac} (meV/K)	$\Gamma_{0(LO)}$ (meV)	γ_{LO} (meV)
	0.16 ± 0.01	21 ± 1	21 ± 1	52 ± 2	0.20 ± 0.02	21 ± 2	42 ± 1	24 ± 1

3.2 Coupling of phonons with excitons and free charge carriers in formamidinium bromide perovskite nanocrystals

Formamidinium lead bromide (FAPbBr$_3$) nanocrystals show unique optoelectronic and PL properties. They are more stable compared with the MAPbBr$_3$. The same technique and method can be used to investigate the FAPbBr$_3$ nanocrystals as well.

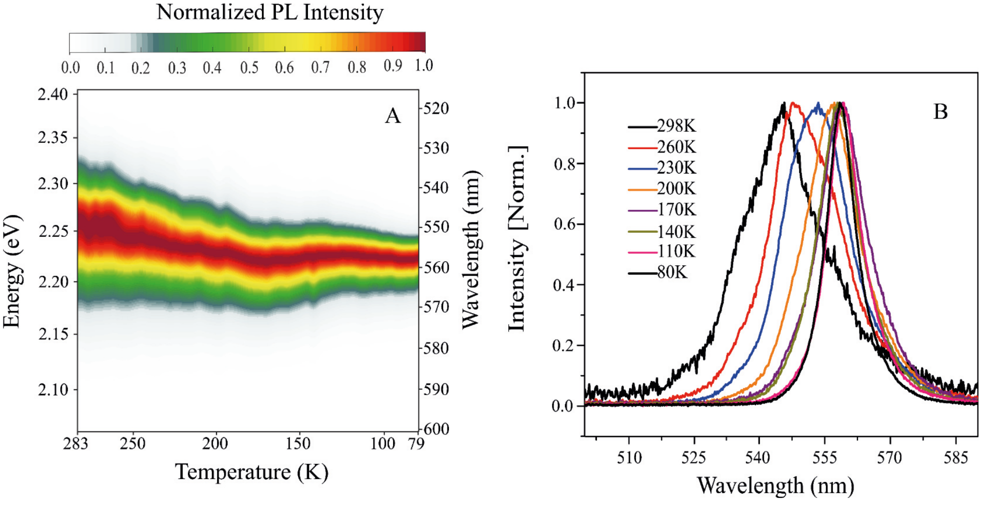

Figure 3.3
(A) Temperature dependent PL map of FAPbBr$_3$ NCs cooling from room temperature. (B) Normalized PL spectra of FAPbBr$_3$ at different temperature (RT to 80 K).

The temperature dependent two-photon PL spectra from 283 to 79 K of the NCs is shown in **Figure 3.3 (A)**. **Figure 3.3 (B)** shows the normalized spectra averaged over 20 points at selected temperatures. Firstly, it can be seen that FAPbBr$_3$ NCs contain three phases at room temperature (CU phase at 537 nm, TE phase at 557 nm, and OR phase at 548 nm[98]). Below 260 K, it only contains the OR phase. Secondly, the different contribution from the population of free charge carriers and excitons influence the position of the maximum in the PL spectra. Thirdly, a gradual red shift in PL is observed when the temperature decreases from room temperature until 200 K due to the increased exciton population. Compared with $MAPbBr_3$ BCs (**Figure 3.1 (B)**), there is no phase transition below 260 K, indicating that the main PL peak originates from the same phase as for the high temperature. In addition, the maxima of the PL spectra shift from 546 to 558 nm, giving an approximated exciton binding energy of 0.05 eV. Compared with the exciton binding energy in $FAPbBr_3$ BCs in the OR phase (0.022 eV)[99], the relatively high exciton binding energy estimated here can be caused by the lattice induced compression strain and the localization of s^2 electron density in Pb^{2+} which can affect the cation-anion interaction in VB[107].

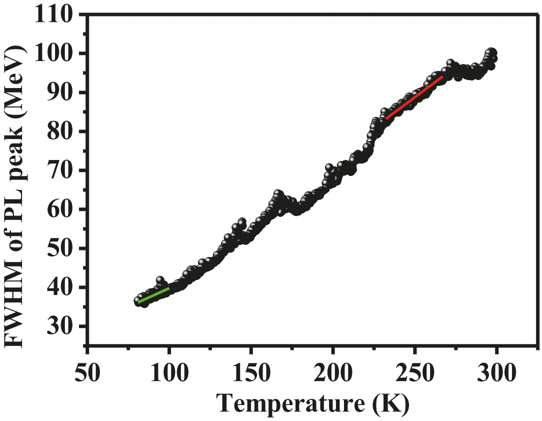

Figure 3.4
Temperature dependent PL FWHM of the $FAPbBr_3$ NCs. The red curve shows the LO phonon coupling to free charge carriers. Green line is the acoustic phonon and exciton coupling.

The temperature broadening of the PL linewidth can be used to investigate the coupling of phonons with excitons and free charge carriers. As above, the analyses are carried out separately for the high temperatures (240 - 298 K) and low temperatures (79 - 100 K), which is shown in **Figure 3.4**. Based on **equations 3.1-3.4**, the fitting results providing coupling strength and the fitting parameters are shown in **Table 3.2**. LO phonon free charge carrier coupling strength is about 58 meV and the acoustic phonon exciton coupling strength is about 0.1 meV/K, which is similar to the case in $FAPbBr_3$ bulk perovskites (61 ± 7 meV and 0.06 ± 0.02 meV/K)[101]. Thus, the acoustic phonon – exciton coupling strength is higher in the NCs compared with the bulk crystal counterpart. In total, these findings provide a fundamental understanding of the carrier phonon dynamics in the early stage hot carrier cooling.

Table 3.2
Extracted Line Width Parameters

Sample	$\Gamma_{0(ac)}$ (meV)	γ_{ac} (meV/K)	$\Gamma_{0(LO)}$ (meV)	γ_{LO} (meV)
$FAPbBr_3$	21±2	0.1±0.02	32±1	58±1

Chapter 4 PL emission of excitons and free charge carriers with the influence of local band structure deformation

In a direct band gap semiconductor, the carrier recombination processes are complex due to the existence of excitons, traps, and structural inhomogeneities. The recombination kinetics have a close relationship with the unique advantages of the perovskite material such as long carrier diffusion length, which is crucial for a material to be efficient in electronic devices[9,10]. Therefore, the investigation of the segregation of first order (1O) and second order (2O) recombination channels and their distribution as well as contribution to the PL emission is important. Based on the phase modulation two-photon PL microscopy technique (**section 1.4.3**), separate quantification of the emission from excitons and free charge carriers in $MAPbBr_3$ crystal can be achieved.

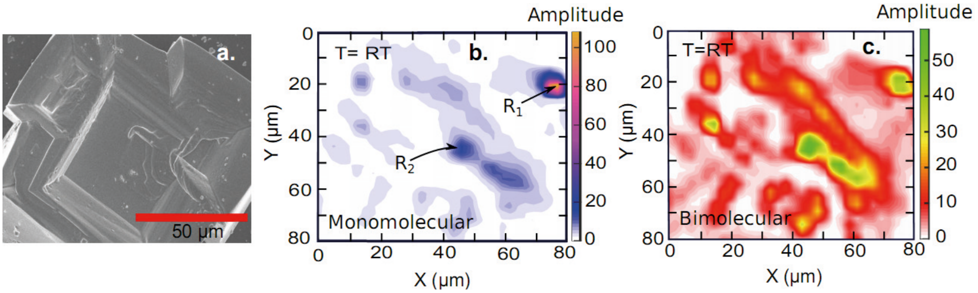

Figure 4.1
Spatially resolved maps of the excitons and free charge carriers in a crystal of $MAPbBr_3$ at room temperature. (a) An SEM image of the $MAPbBr_3$ crystal. Size of the image is 80 µm * 80 µm. (b) Spatial distribution of excitons obtained from the monomolecular recombination. (c) Distribution of free charge carriers obtained from the bimolecular recombination. The amplitudes of each image are scaled by the colour bar to emphasize the spatial features. The R_1 in (b) shows the predominant contribution from the excitons. The R_2 in (b) shows the predominant contribution from the free charge carriers.

Figure 4.1 (a) presents the SEM image of a $MAPbBr_3$ crystal. The PL distributions obtained from excitons and free charge carriers at room temperature are shown in **Figure 4.1 (b)** and **(c)**, respectively. Firstly, the SEM image shows structural inhomogeneities, which results in the variations in emission from the excitons following the 1O recombination and free charge carriers following the 2O recombination. As the exciton binding energy ($E_b = 35 - 50\,\text{meV}$)[108] is slightly larger than the thermal energy at room temperature ($E_t = 25\,\text{meV}$), the free charge carriers dominate compared to the excitons[15,109]. Due to the highly emissive property of the excitons generated from the free electrons and holes, the total emission from the free charge carriers (**Figure 4.1 (c)**) is about 4 times higher than that from the excitons (**Figure 4.1 (b)**). Besides, the excitonic emission is the predominant in some small isolated localized spot crystal (R_1 in **Figure 4.1 (b)**). Such localized spot scenario has been investigated previously[15,84].

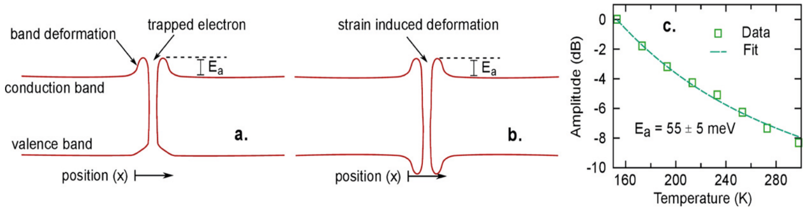

Figure 4.2
Influence of band structure deformation on PL. **(a, b)** show band structure deformations in the conduction and VB induced by trapped charges (in this case trapped electrons) and local strains, respectively. The local band structure deformations in $MAPbBr_3$ create a barrier for the capture of free charge carriers and excitons. As the charges and excitons do not have enough thermal energy to cross the barrier and reach the traps at low temperatures, they recombine radiatively. At room temperature, a significant number of charges and excitons can reach the traps and recombine nonradiatively reducing the yield of PL. The dependence of the total emission on the temperature following **eq 4.1**shown in **(c)**. The measured data are shown by boxes, and the line is the resulting fit. The height of the barrier Ea, obtained from the fit is 55 ± 5 meV.

In semiconductor, nonradiative recombination process induced by impurities (traps or strains, shown in **Figure 4.2 (a)** and **(b)**, respectively) can decrease the emission from perovskites at room temperature[11]. The band structure deformation potential of traps or strains acts as barrier and protects the free charge carriers and excitons from the nonradiative recombination[110]. The strain induced band structure deformation generates a barrier to the electrons, hole and the excitons. Therefore, it controls the whole emission from the perovskite. While the trap induced band structure deformation is generated by the Coulomb repulsion between the trapped electrons and free electrons, while giving a less influence on the excitons. The height of the barrier (E_a) determines the temperature dependent PL emission (η) and the relationship is given by,

$$\eta = 1/(1 + C exp(-E_a/(k_B T))) \quad (4.1),$$

where k_B is the Boltzmann constant and C is a constant. The total emission at different temperatures from (153 - 298 K) is fitted with **eq 4.1**. The height of the barrier is obtained to be 55 ± 5 meV (**Figure 4.2 (c)**).

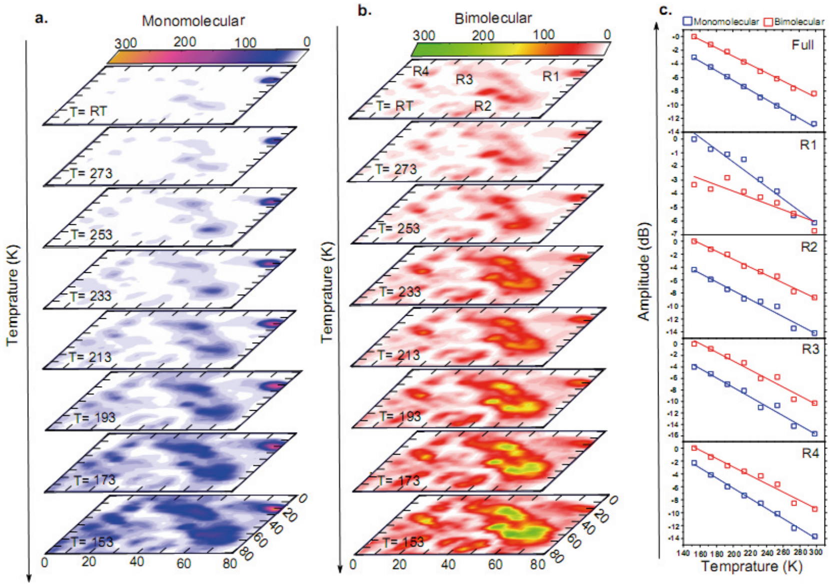

Figure 4.3
Temperature dependent spatially resolved PL maps of the excitons and the free charge carriers (153 K to room temperature). Images with an area of 80 µm × 80 µm are recorded for excitonic emission in **(a)** and emission from free charge carriers in **(b)**. Temperature dependence of the emissions from the intense regions, R_1, R_2, R, and R_4, and the emissions integrated over the crystal are shown in **(c)**. Solid blue and red lines are fitting results corresponding to the emissions from the excitons and free charge carriers, respectively.

In addition, by analyzing the emissions from the exciton and free charge carriers separately, it is possible to identify the type of the deformations to the band structure. The temperature dependent spatially resolved PL maps from 1O and 2O recombination are shown in **Figure 4.3 (a)** and **(b)**, respectively. Figure **4.3 (c)** shows the emission from excitons and free charge carriers in the whole region, R1, R2, R3, and R4, respectively. The fitted results are summarized in **Table 4.1**. The activation energy in the whole region for the trapping of excitons is higher than that of free charge carriers, indicating that both the electrons and holes pass through the barrier. Besides, in R1, R2, and R3 region, the activation energies of the excitons and free charge carriers are quite similar to that in the whole region. While the emission from excitons dominate in R4 region and the activation energies are significantly larger. The higher activation energy for the free charge carriers indicates that the band structure deformations are resulted from both the trapped charges and the local strains, making a significant influence on the PL emission. Therefore, the strain in crystals can be controlled by the size, shape, or morphology to improve the light-emitting performance of the perovskite crystals.

Table 4.1
Height of the Barrier Preventing Nonradiative Recombination of Excitons and Free Charge Carriers in a Crystal of $MAPbBr_3$

Region	Excitons (meV)	Free charge carriers (meV)
Average	75 ± 7	49 ± 4
R_1	73 ± 7	56 ± 6
R_2	78 ± 12	50 ± 6
R_3	75 ± 8	63 ± 10
R_4	90 ± 12	131 ± 28

Chapter 5 Phase modulation technique and the effect of accumulation

Phase modulation two-photon microscopy can be used to spatially quantify the emissions from 1O and 2O radiative recombination in $MAPbBr_3$ perovskites (chapter 4). For laser pulses with high repetition rate, the charge accumulation effect needs to be considered when the ground state recovery timescale is larger than the interval t_0 between two laser pulses ($t_0 \simeq 14.25\ ns$). In this case, the accumulation effects like bleaching of the ground state can influence the amplitude of the lower harmonics and introduce additional higher harmonics (3H and 4H) in the 1O process as well[111]. Since the 2O recombination is fast (in picosecond scale)[12] compared to the 1O recombination, it does not contribute to the charge accumulation effect. The ground state recovery timescale is mainly determined by the 1O recombination lifetime in the $MAPbBr_3$ perovskites.

Based on the model in **section 1.4.4**, the nonlinear least-square analysis (Levenberg-Marquardt algorithm) provided by MATLAB is used to fit the experimentally measured amplitudes of three harmonics A1H, A2H and A3H. As a result, the harmonics of the first order recombination F1H, F2H, F3H, F4H, and second order recombination S1H, S2H, S3H, S4H, together with the time constant of 1O recombination process (τ) can be obtained. While the fitting results is strongly influenced by the starting lifetime value (the starting value for the iterative Levenberg-Marquardt fitting procedure). Therefore, it is necessary to optimize the fitting results by varying the given initial timescale for the 1O recombination process.

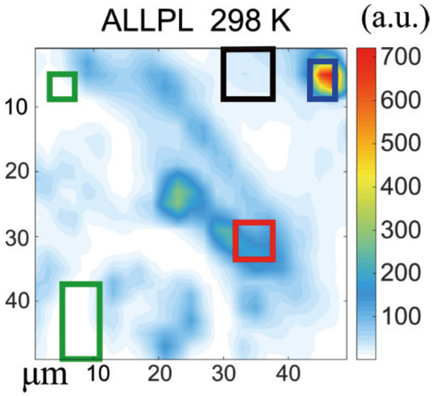

Figure 5.1
Determination of four regions based on the total PL emission at room temperature. HR: high PL region; MR: medium PL region; LR: low PL region; LOR: localized spot region. The areas representing HR, MR, LR, and LOR are enclosed by red, black, green, and blue rectangles. The investigated area of each figure is 50*50 μm^2.

There are four characteristic regions in the $MAPbBr_3$ perovskite films: high PL region (HR), middle PL region (MR), low PL region (LR), and localized spot region (LOR), consisting of 9, 16, 22, and 6 pixels, respectively. These four regions are defined via the total PL emission at room temperature, which is shown in **Figure 5.1**. The areas representing HR, MR, LR, and LOR are enclosed by red, black, green, and blue rectangles. The investigated area of each figure is 50*50 μm^2.

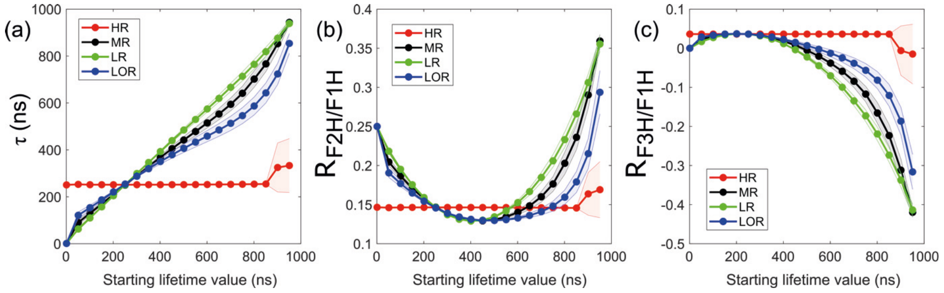

Figure 5.2
(a) Fitted timescales at different stating lifetime value, (b) fitted ratio of $R_{\frac{F2H}{F1H}}$, and (c) fitted ratio of $R_{\frac{F3H}{F1H}}$ based on Levenberg-Marquardt least square method. The standard deviations are calculated based on the 9, 16, 22 and 6 pixels based on the mask matrix for high PL region (HR), middle PL region (MR), low PL region (LR), and localized spot region (LOR), respectively. The shaded regions represent the 0.5*STD.

It turns out that fitting of the pixels in many regions of the analysed image tend to get stuck in local minima which depend on the initial guess of the parameter τ. **Figure 5.2** shows the relationships between the starting lifetime value τ value (the 1O recombination lifetime), fitted ratio of $R_{\frac{F2H}{F1H}}$, and fitted ratio of $R_{\frac{F3H}{F1H}}$ and the results at 113 K taken separately for four characteristic regions. Different from the other regions, in HR the convergence of the τ is very robust consistently leading to the same τ = 250 ns independent of the initial guess. Therefore, we use 250 ns as the starting lifetime value of τ in all pixels.

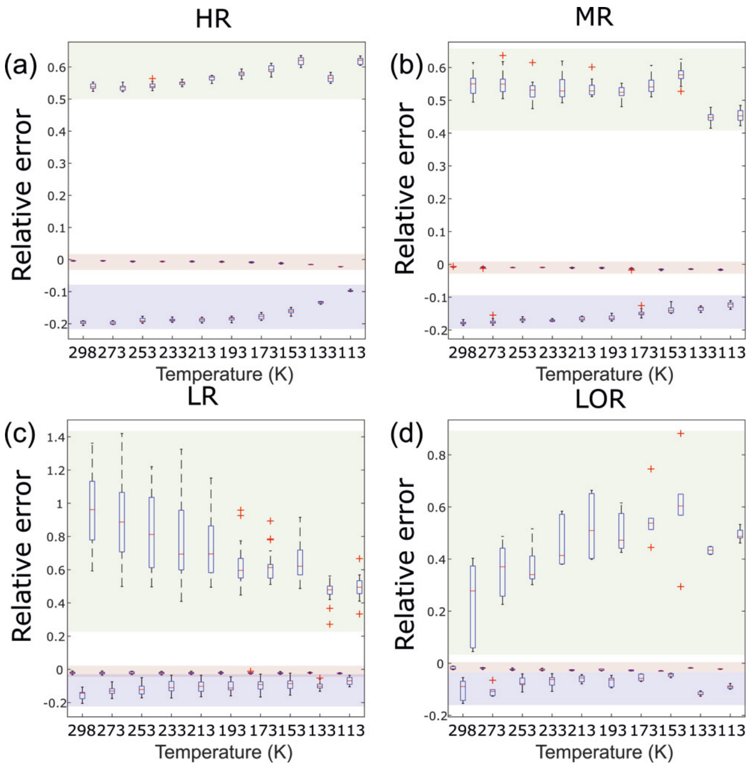

Figure 5.3
(a-d) the relative error of HR, MR, LR, and LOR, respectively at different temperatures. The enclosed pink, purple, and light blue rectangles represent the relative error of A1H (R_{err_1H}), A2H (R_{err_2H}), and A3H (R_{err_3H}), respectively.

The relative deviation between the experimental amplitudes A1H, A2H, A3H and the corresponding model can be expressed as,

$$R_{err\_1H} = \frac{(\mathrm{F1H} + \mathrm{S1H}) - \mathrm{A1H}}{\mathrm{A1H}}, (5.1)$$

$$R_{err\_2H} = \frac{(\mathrm{F2H} + \mathrm{S2H}) - \mathrm{A2H}}{\mathrm{A2H}}, (5.2)$$

$$R_{err\_1H} = \frac{|\mathrm{F3H} - \mathrm{S1H}| - \mathrm{A3H}}{\mathrm{A3H}}. (5.3)$$

These deviations for four regions at different temperatures are presented in **Figure 5.3**. The deviations in HR, MR, and LOR are quite small while in LR the deviations are larger due to the experimental uncertainty in this low signal region.

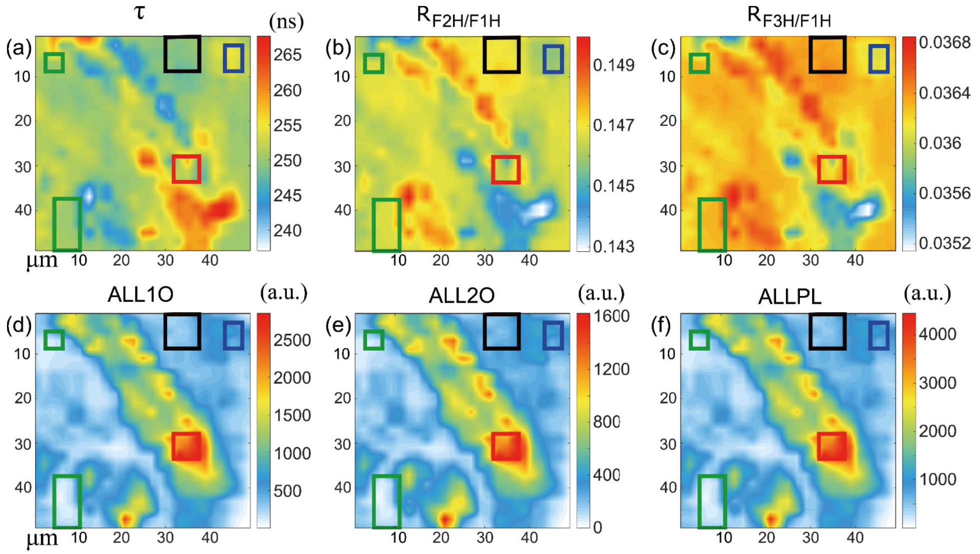

Figure 5.4
Images based on the analyses of the two-photon excited PL of $MAPbBr_3$ perovskite film at 113 K. The following fitting results are shown: (a) the time constant of ground state recovery τ in 1O recombination, (b) ratio of amplitudes F2H/F1H of 1O recombination, (c) ratio of amplitudes F3H/F1H of 1O recombination, (d) sum of all 1O recombination ALL1O, (e) sum of all 2O recombination ALL2O, and (f) sum of both first and second order recombination ALLPL. The areas representing HR, MR, LR, and LOR are enclosed by red, black, green, and blue rectangles. The investigated area of each figure is 50*50 μm^2.

The PL intensity shows large spatial variations which can be explained by the differences in the local non-radiative channels[54,112]. The higher the concentration of the traps, the more non-radiative recombination is expected, and the lower the PL amplitude. In addition, due to the high trap density or deeper trap states in LR, marked with green rectangle, low levels of both 1O and 2O recombination PL were found. The MR region marked with a black rectangle shows the medium intensity region with PL levels between HR and LR. For the LOR, the morphology has significantly changed due to the phase transition from TE (**Figure 5.1** at room temperature) to OR phase (**Figure 5.4 d-f** at 113 K).

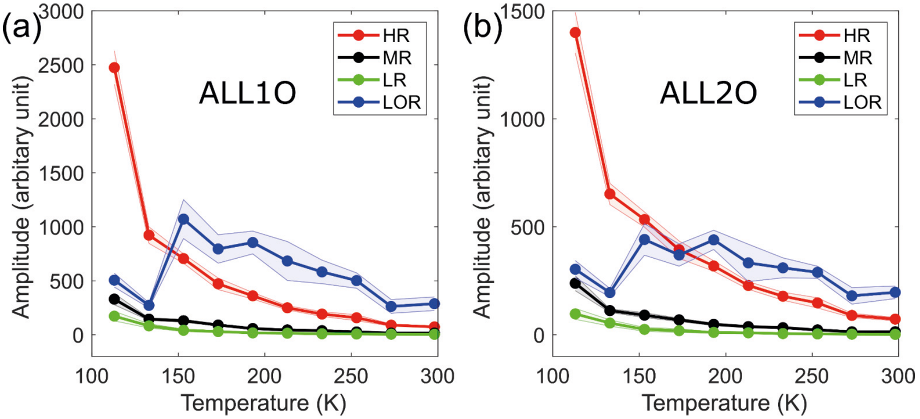

Figure 5.5
Temperature dependence of the 1O recombination PL amplitude ALL1O (a) and 2O PL amplitude ALL2O (b) in four regions defined in Fig 4. The standard deviations (SD) are calculated based on the 9, 16, 22, and 6 pixels in the HR, MR, LR, and LOR, respectively. The shaded regions represent the 0.5*SD.

Figure 5.5 a-b show the changes of averaged amplitude of 1O and 2O recombination in the four regions as a function of temperature. In general, it can be found that the PL intensities for all the regions except localized spot region increase with decreased temperature, which is similar to the trend obtained based on the previous model[13]. This phenomenon is also found in $MAPbI_3$ films and single crystal samples[43,44]. The population of intrinsic defects follows a Boltzmann distribution and therefore it is exponentially sensitive to temperature[115]. Besides, the localized spot regions are the brightest in 1O PL emission, and are almost the brightest regions in the 2O PL emission above 200 K (as shown the blue curve in **Figure 5.5).** This suggests that the grain boundaries in the localized spot act as barriers that restrict the diffusion of photodoped holes around the trap sites, leading to a decelerated depopulation and longer radiative recombination lifetime[116]. After the phase transition from TE to OR at around 150 K[35,117–120], the 1O recombination PL in localized spot regions significantly decreases. This indicates that the barrier effect disappears after the phase transition. Alternatively, the phase transition may induce additional defects.

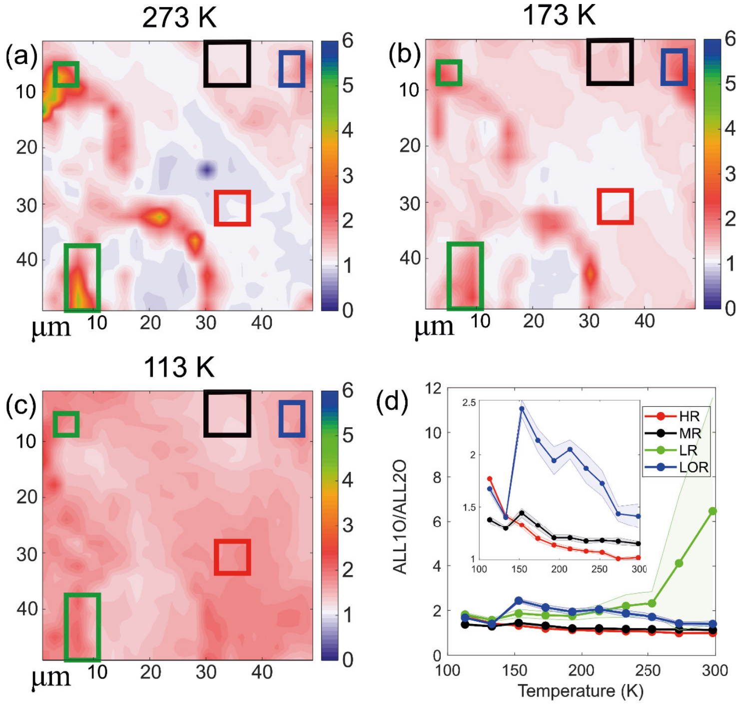

Figure 5.6

The ratio of the 1O and 2O recombination PL amplitude $\frac{A_{1O}}{A_{2O}}$ (a) at 253, (b) 173, and (c) 113 K. The HR, MR, LR, and LO are marked as in **Figure 5.4**. (d) Temperature dependence of $\frac{A_{1O}}{A_{2O}}$ in the four regions.

Images of the ratio $\frac{A_{1O}}{A_{2O}}$ at 253, 173, and 113 K are shown in **Figure 5.6 a-c** and the temperature dependence of the ratios in the four regions are shown in **Figure 5.6 d**. The images of the ratio $\frac{A_{1O}}{A_{2O}}$ show large spatial variations as well which can be explained by the different 1O and 2O recombination PL channels. When the ratio is larger than 1, the 1O recombination process is the predominant process. It is obvious that the 1O recombination process is the predominant process in all the four regions for the two phases. Besides, the ratio in the LR is larger than that in the HR, and the ratio in the LOR is larger than that in the HR as well. The reasons are different and will be explained in detail in the following section (**Figure 5.8**). In addition, the ratios $\frac{A_{1O}}{A_{2O}}$ in HR, MR, and LOR are increasing with temperature decreasing in the TE phase. While the ratios $\frac{A_{1O}}{A_{2O}}$ are similar in these three regions in the OR phase at low temperatures.

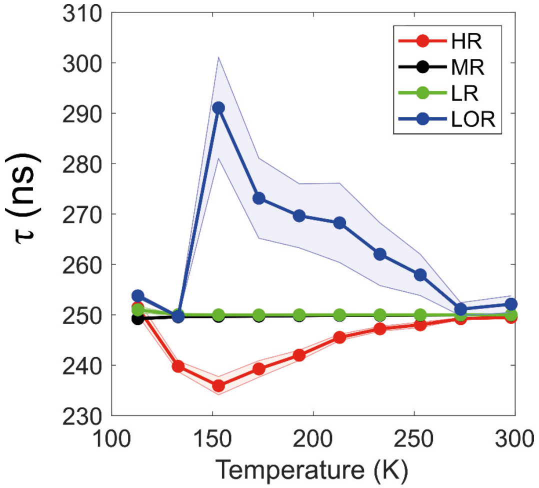

Figure 5.7
Fitted 1O recombination time constant (ns) as a function of temperatures. The standard deviations are calculated based on the 9, 16, 22 and 6 pixels based on the mask matrix for high PL region (HR), middle PL region (MR), low PL region (LR), and localized spot region (LOR), respectively. The shaded regions represent the 0.5*STD.

Figure 5.7 presents the temperature dependence of 1O recombination lifetimes. The 1O recombination lifetime which is decreasing in the TE phase and increasing in the OR phase with temperature decreasing in HR, behaves differently in two phases. In addition, the 1O recombination lifetime in LOR increases with decreased temperature in the TE phase, and it does decrease a lot after the phase transition. However, the 1O recombination lifetime in the MR and LR does not change significantly, meaning that the phase transition does not influence them.

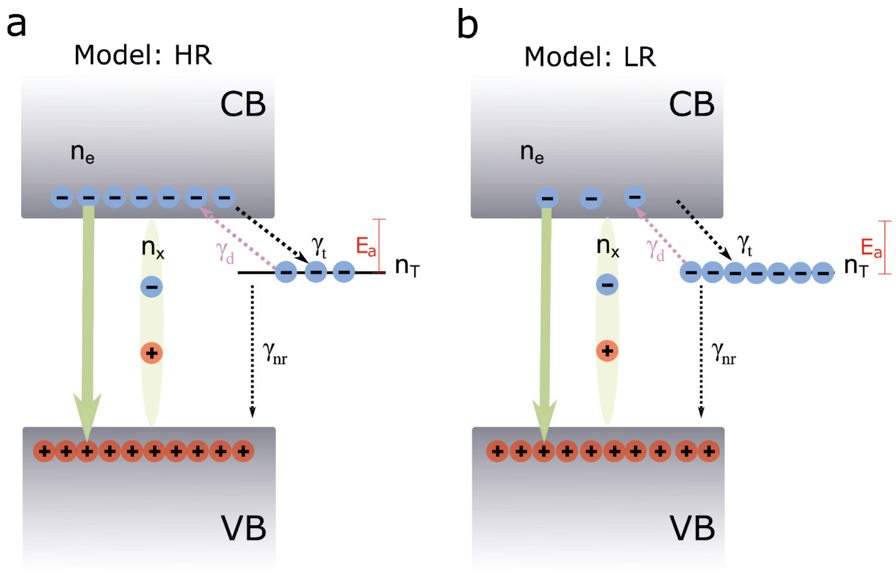

Figure 5.8
(a) Photophysical scenario of HR in the perovskite and (b) Model for LR in the perovskite.

To further explore the effect of the spatial distribution of traps on the thermal PL dynamics, we adapt the trapping model by Stranks and coworkers[11] for our experimental conditions considering the thermal electron-hole PL and thermal excitonic PL in HR and LR. Schematic explanation of the model is presented in **Figure 5.8**. The rate equations for the excitons, free electrons and trapping can be given by the set of rate **equations (5.4) - (5.6).**

$$\frac{dn_X}{dt} = R_f n_e n_h - R_d n_X - R_X n_X \quad (5.4)$$

$$\frac{dn_e}{dt} = G + R_d n_X - R_f n_e n_h - \gamma_t n_e (N_T - n_T) - R_{eh} n_e n_h + \gamma_d n_T \quad (5.5)$$

$$\frac{dn_T}{dt} = \gamma_t n_e (N_T - n_T) - \gamma_{nr} (n_T n_e + n_T^2) - \gamma_d n_T \quad (5.6)$$

No hole trapping is considered. N_T is the concentration of the electron traps which varies from region to region, n_T is the concentration of the filled traps and gives also the corresponding concentration of the free photodoped holes in VB. Thus, the free electrons at a certain temperature can be obtained as $n = n_e$ and the free holes are obtained as $n_h = n_e + n_T$. G is the generation rate determined by the two-photon absorption. n_X is the concentration of excitons. The parameters R_f, R_d, and R_x are the exciton formation from free electron and hole (nongeminate recombination of an electron and hole to an exciton), dissociation to electron and hole, and radiative recombination rate, respectively. R_{eh} is the radiative recombination rate of free electrons and holes. γ_t, γ_d, and γ_{nr} are the trapping, de-trapping, and the trap mediated non-radiative recombination rate, respectively.

There are two channels which give PL, namely free electron-hole pair recombination R_{eh} and exciton recombination R_x. Both can lead to 1O and 2O dependence. Let us first discuss the 2O emission scenarios. Clearly, the term $R_{eh}n_e n_h$ after an intense laser pulse when we have high concentration of electron-hole pairs, corresponds to the 2O process. In this regime the exciton emission $R_X n_X$ is also 2O if the exciton/charge carrier balance is such that it is determined by the quadratic term $R_f n_e n_h$. The latter is very similar to the Saha-Langmuir description of the exciton/free carrier balance which also depends on the exciton binding energy and temperature. The 1O radiative recombination of excitons after an intense laser pulse is very short-lived and the corresponding contribution to the integrated emission is small. The 1O recombination also appears once the concentration of the electrons has dropped due to the trapping. In this case n_e is much less than $n_h = n_e + n_T$ and $n_e \ll n_T$ and the term $n_e n_h \approx n_e n_T$ leads to 1O PL in both two radiative channels. In this regime the de-trapping channel $\gamma_d n_T$ may become particularly important at longer timescales after the excitation pulse when the rapid 2O recombination has depleted the population. The de-trapping also leads to temperature dependence of the PL.

In the TE phase, besides the 1O $R_X n_X$ and 2O $R_f n_e n_h$ after an intense laser pulse and the 1O de-trapped $R_{eh}n_h$ in both HR and LR, the 1O de-trapped $R_X n_X$ in the HR and 2O de-trapped $R_X n_X$ in the LR generates a higher $\frac{A_{1O}}{A_{2O}}$ in LR, compared with $\frac{A_{1O}}{A_{2O}}$ in the HR. Further on, the grain boundaries in the localized spot act as barriers that restrict the diffusion of photodoped holes around the trap sites. The increased n_e leads to more exciton population in the localized spot according to the Saha-Langmuir equation, and the extra 1O $R_X n_X$ in the LR results in a higher $\frac{A_{1O}}{A_{2O}}$ in LOR compared with that in the HR. In addition, the population of excitons *vs* free charge carriers is increasing at lower temperature based on the Saha-Langmuir equation. As a result, the ratios of $\frac{A_{1O}}{A_{2O}}$ in HR, MR, and LOR increase at lower temperature in the TE phase. After the phase transition, the barriers in the localized spot may disappear due to the structural changes (see **Figure 5.1** and **Figure 5.4**). As the consequence, the ratios become quite similar in the OR phases with decreased temperature in these three regions.

To better understand the carrier dynamic in different regions with different traps, it is of great importance to know the 1O recombination lifetime. In the HR, the gradually frozen deeper traps reduce de-trapping thereby the 1O recombination lifetime here is shorter at lower temperature. After phase transition, the increased bandgap or emerged new traps may increase the trapping and de-trapping process in HR. In the LOR, the increased 1O recombination lifetime suggests that the boundary effect is increasing with temperature decreasing. While the abrupt decrease of the 1O recombination lifetime indicates that the boundary effect disappears after the phase transition from TE phase to OR phase with decreased temperature. In addition, the 1O recombination lifetimes in the MR and LR do not change significantly, which may be due to abundancy of traps with different depths which do not significantly influence the trapping and de-trapping processes.

Chapter 6 $MAPbBr_3$ solar cell device and microplate photodetector

The perovskite works well for the solar cells and photodetector applications due to the high carrier mobility with less LO phonon – carrier coupling strength (chapter 3), longer diffusion length with slower total recombination rate and longer 1O recombination rate (chapter 4 and 5). For a good solar cell material such as GaAs, the photo-generated electrons and holes have no place to go under the open-circuit condition. Therefore, the external luminescence emission balances the incoming sunlight. Any nonradiative recombination channel impairs the carrier density, lowering the open-circuit voltage. Thus, efficient external luminescence (which is good for the LED application) is a counterintuitive necessity to approach the Shockley-Queisser (SQ) efficiency limit[121]. Further, the short-circuit current of a solar cell material mainly depends on two aspects: the ability to absorb light which generates the carriers and the yield of the generated free charge carriers reaching the electrical contacts successfully. Here too, any nonradiative recombination channel impairs the carrier density, lowering the short-circuit current. The high open-circuit voltage as well as the short-circuit current contribute to the high output power of a solar cell. Therefore, it is of significance to investigate the external luminescence as well as the PC under the same excitation condition, giving detailed information on the charge carrier dynamics.

6.1 Variation in PC response due to the different PL emissive states

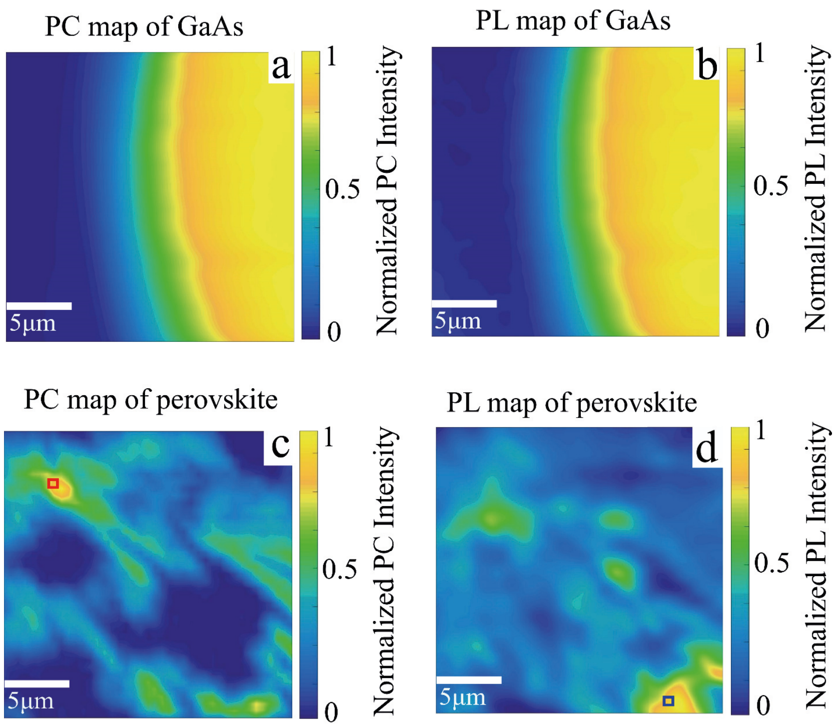

Figure 6.1
(a) PC map and (b) PL map measured on the film of GaAs solar cell, and (c) PC map with region A marked by a red box and (d) PL map with region B marked by a blue box measured on the film of $MAPbBr_3$ perovskite. The regions A and B are later used for biases dependent study and the detial are present in Figure 6.3.

The PC and PL maps of the GaAs solar cell film at zero bias are shown in **Figure 6.1 (a)** and **(b)**, respectively. It is obvious that the edge of the solar cell appears in both the PC and PL map, separating the active region (yellow) and substrate region (blue). The regions that give high PL also give high PC signal. The Pearson's correlation coefficient (γ) **(equation 6.1)** can be used to characterize the correlation of these two images,

$$\gamma = \frac{\sum_{i=1}^{n}(x_i - \bar{x})(y_i - \bar{y})}{\sqrt{\sum_{i=1}^{n}(x_i - \bar{x})^2}\sqrt{\sum_{i=1}^{n}(y_i - \bar{y})^2}} \quad (6.1)$$

where x_i and y_i represent the PC and the PL yields at different positions in the investigated area, respectively. The calculated correlation coefficient from these two images is 0.9993, indicating the emissive states contribute not only to the PL signal but also the PC signal, which is expected in the case of an ideal solar cell. While the PC map and PL map of the $MAPbBr_3$ perovskite do not show a clear correlation (as shown in (**Figure. 6.1 (c)** and **(d)**). The Pearson's correlation coefficient of **Figure 6.1 (c)** and **(d)** is only 0.32. There are several reasons for this poor correlation. Firstly, the inhomogeneity in the film thickness can contribute to the variations in the PC and PL map. Secondly, the contact heterogeneity adds randomness to the PC response[122]. The truelly intrinsic sources for the poor PC and PL correlation in $MAPbBr_3$ perovskite solar cell need to be explored.

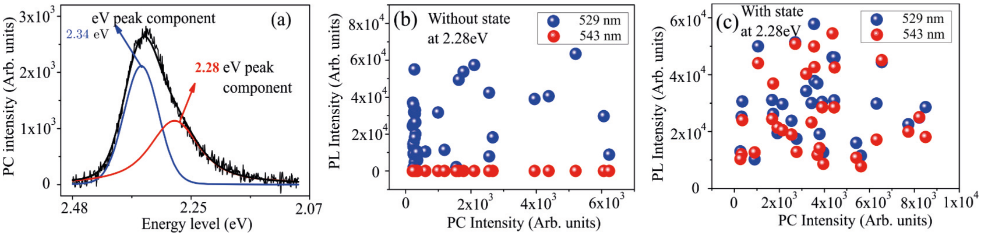

Figure 6.2
PL spectrum peak fitting results as a function of PC response for positions of interest in $MAPbBr_3$ perovskite solar cell. (a) The PL spectrum is fitted with two Voigt profiles centered at 2.34 eV (blue line) and 2.28 eV (red line); (b) PL and PC correlation in regions where the 2.28 eV emission does not occur; (c) PL and PC relationship in regions shows. The blue and the red dots are the areas under the corresponding Voigt profiles.

As mentioned above, the PL spectra of each point in the image of **Figure 6.1 (d)** are obtained under zero bias voltage. One of the representative PL spectra is shown in **Figure 6.2 (a).** The spectra can be decomposed to two Voigt profiles centered at 2.34 eV (blue) and 2.28 eV (red), respectively. The integrated area under the two fitted lines gives the corresponding PL intensity. Positions with high PC intensity and positions with high PL intensity are selected to perform the peak fitting based on **Figure 6.1 (c)** and **(d)**. Normally, two pathways corresponding to the PC and the PL from one state are expected and there are four pathways for two emissive states in total. After peak fitting, the PL at 2.34 eV can be observed in all of the selected positions in the sample, while the emissive state at 2.28 eV component is not present everywhere. In **Figure 6.2 (b)**, the positions show the PL contribution at 2.34 eV vs PC, while the 2.28 eV emission is negligible. This suggests the absence of the state responsible for 2.28 eV emission and the PC at these positions originate from the 2.34 eV emissive states. The positions showing significant PL contribution with negiligible PC contribution suggest the poor contacting of the electrodes. **Figure 6.2 (c)** shows the PL intensity versus PC plot from the positions where the contribution from both emitting states is significant. The random distribution of the PL yield suggests that significant heterogeneity is present. Besides, the appearance may be due to the contribution to the PC from both emissive states. It may be also due to the fact that the PC is only contributed by the 2.34 eV state and the appearance of the 2.28 eV is caused by the energy transfer from the high energy state to the lower energy state.

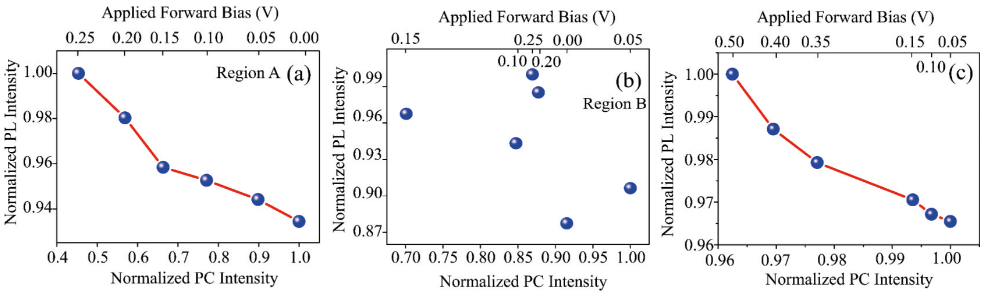

Figure 6.3
(a) PC-PL relation in the region A without emissive state at 2.28 eV by applying different forward bias to $MAPbBr_3$ perovskite solar cell; (b) in the region B with the emissive state at 2.28 eV and (c) PC-PL relationship obtained by applying different forward bias to the GaAs solar cell;

To confirm the above two possibilities, the PL-PC correlation in region A without 2.28 eV emissive state, in region B with 2.28 eV emission sate, and in the GaAs solar cell by applying different forward bias (0 to 0.25 V) are carried out and the results are shown in **Figure 6.3 (a)**, **(b)**, and **(c)**, respectively. The modulated signal at 3 kHz as well as the small window of bias voltage is used to eliminate the influence caused by the impedance of the device. Besides, the signal at the modulation frequency can select the contribution from the light induced current only. While the dc signals contain the contribution from the dark current that is not easy to separate. Typically, when a forward bias is applied to a direct band gap solar cell, fewer photogenerated carriers can be extracted as current and more radiative recombination occurs, which results in a negative correlation relationship between the PC and PL yields[123]. The obtained correlation coefficient of the PC-PL yield for region A in $MAPbBr_3$ perovskite solar cell and GaAs solar cell are around -0.97, while only -0.4 for region B in $MAPbBr_3$ perovskite solar cell. The weak PC-PL yield correlation suggests that the emissive state at 2.28 eV does not contribute to the PC significantly.

The emissive state at 2.34 eV is quite close to the band gap energy of $MAPbBr_3$ (2.36 eV)[124] and therefore it can be related to the band-to-band carrier recombination. While the emissive state at 2.28 eV is lower than the band gap energy, and it may be originated from the different phase of the $MAPbBr_3$ perovskite (TE phase) or defect-related polaronic emission. This suggests that the sample can be optimized in the preparation process to reduce the emissive traps and to increase the PCE performance.

6.1 High resolution mapping of two-photon excited PC in perovskite microplate photodetector

Single $MAPbBr_3$ microcrystals (MCs) can be used as active material for photodetectors. In this work, the scanning PC microscopy (SPCM) is used based on TPA and making use of the fact that the near-infrared light can penetrate the whole crystal and thereby the focal point, where TPA mainly takes place, can be chosen anywhere in the crystal. We study the PC distribution in single $MAPbBr_3$ MCs under different applied forward biases.

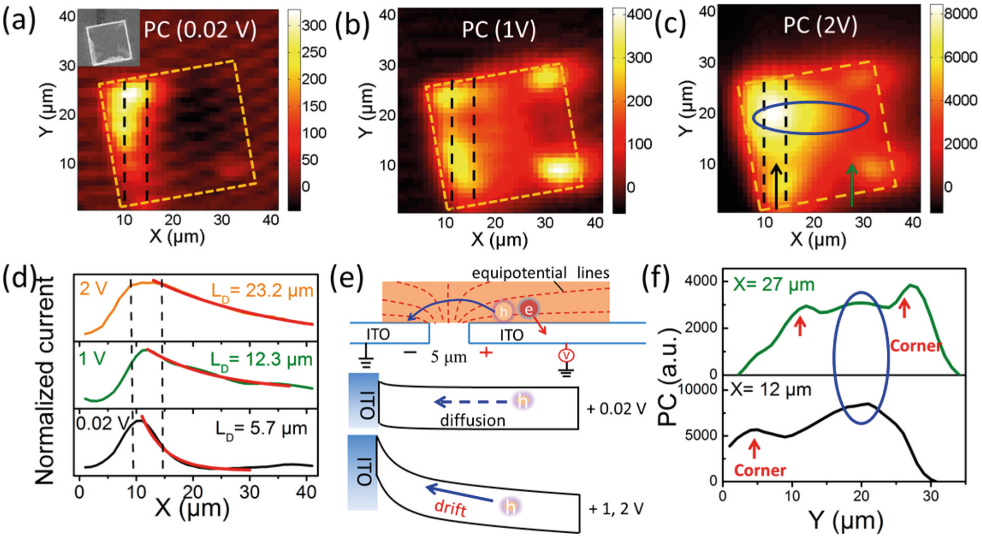

Figure 6.4
PC mapping with 0.02 (a), 1 (b), and 2 V (c) bias. The orange dashed line indicates the MC edge, the two black dashed lines show the ITO gap which separates the two electrodes. Inset of part a: SEM image of the $MAPbBr_3$ MC device used in the experiment. (d) Average PC decay length along X axis with different voltage bias. (e) Illustration of electron and hole transfer (top) and hole diffusion (+0.02 V) and drift (+1, 2 V) in VB. (f) PC intensity along Y axis at different x values with 2 V bias.

The SPCM measurements with 0.02, 1, and 2 V bias were performed on a $MAPbBr_3$ MCs to study the spatial variations of the photocurrent. The results are shown in **Figure 6.4 (a-c)**. The investigated MC size is about 25 × 25 μm^2. The 5 μm indium tin oxide (ITO) gap under the MC is indicated by two parallel black dashed lines. Under a very weak bias (0.02 V), the PC is only generated close to the ITO gap. It can be explained by the small band bending at the electrode gap edge, where the current flow occurs. While the charge carriers further away from the electrode gap perform nearly random motion and do not contribute to the photocurrent[125,126]. The carrier diffusion length can be fitted with the PC intensities along the X axis with an exponential decay function. The fitted diffusion length L_D are about 6.4, 3.7, and

7.0 μm for different Y positions at 7, 15, and 24 μm, respectively. The average diffusion length is about 5.7 ± 1.8 μm, which is quite close to the reported value[127]. The relationship between the diffusion length L_D and the carrier mobility μ can be expressed as **equation 6.2**,

$$L_D = \sqrt{\frac{\mu k_B T}{q}\tau}\ (6.2),$$

where k_B is the Boltzmann constant; T is the sample temperature; q is the elementary charge; τ is the carrier lifetime which is normally 200 ns in this material[128]. Therefore, the estimated carrier mobility is about 63 $cm^2V^{-1}s^{-1}$, which is quite close to the reported value (60 $cm^2V^{-1}s^{-1}$)[129]. This result is consistent with the suggestion that the carrier diffusion is the main mechanisms for the PC under very low bias.

By increasing the bias from 0.02 V to 1 V to 2 V, the PC distribution becomes wider along the X axis (**Figure 6.4 (b) and (c)**) due to the larger band bending at the electrode gap edge by a larger applied forward electric field (**Figure 6.4 (e)**). By fitting the minority diffusion length with an exponential decay under 1 and 2 V, the average PC decay lengths increases to 12.3 ± 2.2 and 23.2 ± 1.9 μm, respectively. Under high applied external bias, between the anode (+) and cathode (-), the band bending is stronger, electrons and holes move faster and can thereby reach their corresponding electrodes from more far[130]. The PC shows large variations among the crystal (**Figure 6.4 (f)**). This strong spatial distribution is mainly due to the inhomogeneous distribution of the trap-states[112].

Conclusions

In this thesis, we have studied photophysics of perovskite by using temperature dependent phase modulation two-photon PL and PC microscopy. These results are of importance for both fundamental research and applications in devices.

After photoexcitation, the hot carriers can be cooled down via carrier-phonon scattering. The temperature-dependent two-photon PL is used to investigate the linewidth broadening resulted from carrier-phonon scattering, coexistence of different phases, emissions from exciton as well as free charge carriers in the $MAPbBr_3$ and $FAPbBr_3$ perovskites. In $MAPbBr_3$ perovskite, we found that TE phase is predominant in the BCs while OR phase is predominant in the thin films (TFs) at room temperature. With decreased temperature, the abrupt blue shift in the PL peak at around 150 K suggests a phase transition from TE to OR in the bulk crystal. While a continuous red shift in the PL peak shows a gradual increase of the exciton population. The higher LO phonon - free charge carrier coupling strength is found in the TFs, suggesting a lower carrier mobility. For the $FAPbBr_3$ NCs, three phases coexist at room temperature and only OR phase exists below 260 K. In addition, the LO phonon - free charge carrier coupling strength in the NCs is found to be higher than the bulk counterparts. Besides, the LO phonon-free charge carrier coupling strength is higher than the exciton-acoustic phonon coupling strength in both $MAPbBr_3$ and $FAPbBr_3$.

Besides cooling, the radiative recombination of excitons as well as free charge carriers can occur. The phase modulation two-photon PL microscopy is used to quantify the contribution of the emission originating from excitons and free charge carriers in $MAPbBr_3$ and separate both contributions spatially and spectrally. The experimental results show that the emission from free charge carriers is predominant in most of the regions in the crystal. While the emission from excitons is predominant in some localized spots. In addition, the nonradiative recombination channels originate from the traps and strain. The band structure deformation depth is highest around the localized spots which protect the photogenerated carriers and promote the 1O recombination process.

Considering the charge accumulation effect, phase modulation two-photon PL microscopy is used to spatially resolve how the impurities change with phase transition in $MAPbBr_3$ polycrystalline perovskite film. We analyzed the PL in terms of 1O and 2O recombination dynamics taking into account the possible accumulation effects related to the depletion of the ground state due to the high pulse repetition rate. We found more 2O recombination emission in the region with less traps. The highly emitting localized spot showed evidence for a boundary which can explain the enhanced 1O recombination emission. With temperature decreasing, the 1O recombination emission is increasing due to the increased exciton population in the perovskite film. Besides, the 1O recombination lifetime is decreasing.

The perovskites can be used to make optoelectronic devices as solar cells and photodetectors owing to their many favourable properties like the high carrier mobility (less LO phonon – carrier coupling strength) and the long diffusion length (slower total recombination rate and longer 1O recombination rate). For the solar cell application, phase modulation two-photon PL and PC microscopy is used to investigate the correlation of the PC response with emission from two different states at 2.28 and 2.34 eV in $MAPbBr_3$ crystal. The experimental results show an obvious heterogeneous distribution both in the PC and PL map. Besides, the strong correlation of PC and PL map for GaAs solar cell and $MAPbBr_3$ solar cell containing only 2.34 eV state indicates that the state at 2.34 eV contributes to the PC significantly. While the emissive state at 2.28 eV, which might be caused by the trap states, will lower the performance of solar cells. For the photodetector application, we use SPCM to investigate the charge carrier distribution and transport in $MAPbBr_3$ MC photodetector. The results show that the charge carrier transport length is dependent on the applied electric field and it varies from 5.7 µm to 23.2 µm under the applied bias from 0.02 to 2 V.

References

(1) Armaroli, N.; Balzani, V. The Future of Energy Supply: Challenges and Opportunities. *Angewandte Chemie - International Edition*. 2007. https://doi.org/10.1002/anie.200602373.

(2) Mohammad Bagher, A. Types of Solar Cells and Application. *Am. J. Opt. Photonics* **2015**. https://doi.org/10.11648/j.ajop.20150305.17.

(3) Slade, A.; Garboushian, V. 27.6% Efficient Silicon Concentrator Solar Cells for Mass Production. *Tech. Dig. 15th Int. ...* **2005**.

(4) https://www.nrel.gov/pv/assets/pdfs/best-research-cell-efficiencies.20200922.pdf.

(5) Geisz, J. F.; France, R. M.; Schulte, K. L.; Steiner, M. A.; Norman, A. G.; Guthrey, H. L.; Young, M. R.; Song, T.; Moriarty, T. Six-Junction III–V Solar Cells with 47.1% Conversion Efficiency under 143 Suns Concentration. *Nat. Energy* **2020**. https://doi.org/10.1038/s41560-020-0598-5.

(6) Shockley, W.; Queisser, H. J. Detailed Balance Limit of Efficiency of P-n Junction Solar Cells. *J. Appl. Phys.* **1961**. https://doi.org/10.1063/1.1736034.

(7) Hedley, G. J.; Ruseckas, A.; Samuel, I. D. W. Light Harvesting for Organic Photovoltaics. *Chemical Reviews*. 2017. https://doi.org/10.1021/acs.chemrev.6b00215.

(8) Docampo, P.; Guldin, S.; Leijtens, T.; Noel, N. K.; Steiner, U.; Snaith, H. J. Lessons Learned: From Dye-Sensitized Solar Cells to All-Solid-State Hybrid Devices. *Adv. Mater.* **2014**. https://doi.org/10.1002/adma.201400486.

(9) Yoo, J. J.; Wieghold, S.; Sponseller, M. C.; Chua, M. R.; Bertram, S. N.; Hartono, N. T. P.; Tresback, J. S.; Hansen, E. C.; Correa-Baena, J. P.; Bulović, V.; Buonassisi, T.; Shin, S. S.; Bawendi, M. G. An Interface Stabilized Perovskite Solar Cell with High Stabilized Efficiency and Low Voltage Loss. *Energy Environ. Sci.* **2019**. https://doi.org/10.1039/c9ee00751b.

(10) Yang, S.; Chen, S.; Mosconi, E.; Fang, Y.; Xiao, X.; Wang, C.; Zhou, Y.;

Yu, Z.; Zhao, J.; Gao, Y.; De Angelis, F.; Huang, J. Stabilizing Halide Perovskite Surfaces for Solar Cell Operation with Wide-Bandgap Lead Oxysalts. *Science (80-.).* **2019**. https://doi.org/10.1126/science.aax3294.

(11) Stranks, S. D.; Burlakov, V. M.; Leijtens, T.; Ball, J. M.; Goriely, A.; Snaith, H. J. Recombination Kinetics in Organic-Inorganic Perovskites: Excitons, Free Charge, and Subgap States. *Phys. Rev. Appl.* **2014**, *2* (3). https://doi.org/10.1103/PhysRevApplied.2.034007.

(12) Herz, L. M. Charge-Carrier Dynamics in Organic-Inorganic Metal Halide Perovskites. *Annu. Rev. Phys. Chem.* **2016**, *67* (1), 65–89. https://doi.org/10.1146/annurev-physchem-040215-112222.

(13) Kumar, P.; Shi, Q.; Karki, K. J. Enhanced Radiative Recombination of Excitons and Free Charges Due to Local Deformations in the Band Structure of MAPbBr3 Perovskite Crystals. *J. Phys. Chem. C* **2019**. https://doi.org/10.1021/acs.jpcc.9b01968.

(14) Shi, Q.; Ghosh, S.; Sarkar, A. S.; Kumar, P.; Wang, Z.; Pal, S. K.; Pullerits, T.; Karki, K. J. Variation in the Photocurrent Response Due to Different Emissive States in Methylammonium Lead Bromide Perovskites. *J. Phys. Chem. C* **2018**, *122* (7), 3818–3823. https://doi.org/10.1021/acs.jpcc.8b00542.

(15) Sarritzu, V.; Sestu, N.; Marongiu, D.; Chang, X.; Wang, Q.; Loi, M. A.; Quochi, F.; Saba, M.; Mura, A.; Bongiovanni, G. Perovskite Excitonics: Primary Exciton Creation and Crossover from Free Carriers to a Secondary Exciton Phase. *Adv. Opt. Mater.* **2018**. https://doi.org/10.1002/adom.201700839.

(16) Zhang, H.; Ye, F.; Li, W.; Gurney, R. S.; Liu, D.; Xiong, C.; Wang, T. Improved Performance of Perovskite Light-Emitting Diodes by Dual Passivation with an Ionic Additive. *ACS Appl. Energy Mater.* **2019**. https://doi.org/10.1021/acsaem.9b00186.

(17) Droseros, N.; Longo, G.; Brauer, J. C.; Sessolo, M.; Bolink, H. J.; Banerji, N. Origin of the Enhanced Photoluminescence Quantum Yield in MAPbBr3 Perovskite with Reduced Crystal Size. *ACS Energy Lett.* **2018**. https://doi.org/10.1021/acsenergylett.8b00475.

(18) Jung, D. H.; Park, J. H.; Lee, H. E.; Byun, J.; Im, T. H.; Lee, G. Y.; Seok, J. Y.; Yun, T.; Lee, K. J.; Kim, S. O. Flash-Induced Ultrafast Recrystallization of Perovskite for Flexible Light-Emitting Diodes. *Nano Energy* **2019**. https://doi.org/10.1016/j.nanoen.2019.04.061.

(19) Su, Y.; Chen, X.; Ji, W.; Zeng, Q.; Ren, Z.; Su, Z.; Liu, L. Highly Controllable and Efficient Synthesis of Mixed-Halide CsPbX3 (X = Cl, Br, I) Perovskite QDs toward the Tunability of Entire Visible Light. *ACS Appl.*

Mater. Interfaces **2017**. https://doi.org/10.1021/acsami.7b10612.

(20) Jiang, Y.; Qin, C.; Cui, M.; He, T.; Liu, K.; Huang, Y.; Luo, M.; Zhang, L.; Xu, H.; Li, S.; Wei, J.; Liu, Z.; Wang, H.; Kim, G. H.; Yuan, M.; Chen, J. Spectra Stable Blue Perovskite Light-Emitting Diodes. *Nat. Commun.* **2019**. https://doi.org/10.1038/s41467-019-09794-7.

(21) Ding, J.; Cheng, X.; Jing, L.; Zhou, T.; Zhao, Y.; Du, S. Polarization-Dependent Optoelectronic Performances in Hybrid Halide Perovskite MAPbX3(X = Br, Cl) Single-Crystal Photodetectors. *ACS Appl. Mater. Interfaces* **2018**, *10* (1), 845–850. https://doi.org/10.1021/acsami.7b13111.

(22) Dou, L.; Yang, Y. M.; You, J.; Hong, Z.; Chang, W. H.; Li, G.; Yang, Y. Solution-Processed Hybrid Perovskite Photodetectors with High Detectivity. *Nat. Commun.* **2014**. https://doi.org/10.1038/ncomms6404.

(23) Bin Yang, Junsheng Chen, Qi Shi, Zhengjun Wang, M. G.; Alexander Dobrovolsky, Ivan G. Scheblykin, Khadga Jung Karki, Keli Han, T. P. High Resolution Mapping of Two-Photon Excited Photocurrent in Perovskite Microplate Photodetector. *J. Phys. Chem. Lett.* **2018**, *9*, 5017−5022.

(24) Tan, Z. K.; Moghaddam, R. S.; Lai, M. L.; Docampo, P.; Higler, R.; Deschler, F.; Price, M.; Sadhanala, A.; Pazos, L. M.; Credgington, D.; Hanusch, F.; Bein, T.; Snaith, H. J.; Friend, R. H. Bright Light-Emitting Diodes Based on Organometal Halide Perovskite. *Nat. Nanotechnol.* **2014**, *9* (9), 687–692. https://doi.org/10.1038/nnano.2014.149.

(25) Sutherland, B. R.; Sargent, E. H. Perovskite Photonic Sources. *Nature Photonics*. 2016. https://doi.org/10.1038/nphoton.2016.62.

(26) Brandt, R. E.; Poindexter, J. R.; Gorai, P.; Kurchin, R. C.; Hoye, R. L. Z.; Nienhaus, L.; Wilson, M. W. B.; Polizzotti, J. A.; Sereika, R.; Žaltauskas, R.; Lee, L. C.; Macmanus-Driscoll, J. L.; Bawendi, M.; Stevanović, V.; Buonassisi, T. Searching for "Defect-Tolerant" Photovoltaic Materials: Combined Theoretical and Experimental Screening. *Chem. Mater.* **2017**. https://doi.org/10.1021/acs.chemmater.6b05496.

(27) Ali, R.; Yashima, M. Space Group and Crystal Structure of the Perovskite CaTiO3 from 296 to 1720 K. *J. Solid State Chem.* **2005**. https://doi.org/10.1016/j.jssc.2005.06.027.

(28) Grätzel, M. The Rise of Highly Efficient and Stable Perovskite Solar Cells. *Accounts of Chemical Research*. 2017. https://doi.org/10.1021/acs.accounts.6b00492.

(29) Eperon, G. E.; Leijtens, T.; Bush, K. A.; Prasanna, R.; Green, T.; Wang, J. T. W.; McMeekin, D. P.; Volonakis, G.; Milot, R. L.; May, R.; Palmstrom, A.; Slotcavage, D. J.; Belisle, R. A.; Patel, J. B.; Parrott, E. S.; Sutton, R. J.;

Ma, W.; Moghadam, F.; Conings, B.; Babayigit, A.; Boyen, H. G.; Bent, S.; Giustino, F.; Herz, L. M.; Johnston, M. B.; McGehee, M. D.; Snaith, H. J. Perovskite-Perovskite Tandem Photovoltaics with Optimized Band Gaps. *Science (80-.).* **2016**. https://doi.org/10.1126/science.aaf9717.

(30) Sheng, R.; Ho-Baillie, A.; Huang, S.; Chen, S.; Wen, X.; Hao, X.; Green, M. A. Methylammonium Lead Bromide Perovskite-Based Solar Cells by Vapor-Assisted Deposition. *J. Phys. Chem. C* **2015**. https://doi.org/10.1021/jp512936z.

(31) Li, W. G.; Wang, X. D.; Liao, J. F.; Wei, Z. F.; Xu, Y. F.; Chen, H. Y.; Kuang, D. Bin. A Laminar MAPbBr3/MAPbBr3-XIx Graded Heterojunction Single Crystal for Enhancing Charge Extraction and Optoelectronic Performance. *J. Mater. Chem. C* **2019**. https://doi.org/10.1039/c9tc00972h.

(32) Poglitsch, A.; Weber, D. Dynamic Disorder in Methylammoniumtrihalogenoplumbates (II) Observed by Millimeter-Wave Spectroscopy. *J. Chem. Phys.* **1987**. https://doi.org/10.1063/1.453467.

(33) Yang, B.; Ming, W.; Du, M. H.; Keum, J. K.; Puretzky, A. A.; Rouleau, C. M.; Huang, J.; Geohegan, D. B.; Wang, X.; Xiao, K. Real-Time Observation of Order-Disorder Transformation of Organic Cations Induced Phase Transition and Anomalous Photoluminescence in Hybrid Perovskites. *Adv. Mater.* **2018**. https://doi.org/10.1002/adma.201705801.

(34) Ghosh, S.; Shi, Q.; Pradhan, B.; Kumar, P.; Wang, Z.; Acharya, S.; Pal, S. K.; Pullerits, T.; Karki, K. J. Phonon Coupling with Excitons and Free Carriers in Formamidinium Lead Bromide Perovskite Nanocrystals. *J. Phys. Chem. Lett.* **2018**, *9* (15), 4245–4250. https://doi.org/10.1021/acs.jpclett.8b01729.

(35) Shi, Q.; Ghosh, S.; Kumar, P.; Folkers, L. C.; Pal, S. K.; Pullerits, T.; Karki, K. J. Variations in the Composition of the Phases Lead to the Differences in the Optoelectronic Properties of MAPbBr3 Thin Films and Crystals. *J. Phys. Chem. C* **2018**. https://doi.org/10.1021/acs.jpcc.8b06937.

(36) Wehrenfennig, C.; Liu, M.; Snaith, H. J.; Johnston, M. B.; Herz, L. M. Charge Carrier Recombination Channels in the Low-Temperature Phase of Organic-Inorganic Lead Halide Perovskite Thin Films. *APL Mater.* **2014**, *2* (8). https://doi.org/10.1063/1.4891595.

(37) Brandt, R. E.; Stevanović, V.; Ginley, D. S.; Buonassisi, T. Identifying Defect-Tolerant Semiconductors with High Minority-Carrier Lifetimes: Beyond Hybrid Lead Halide Perovskites. *MRS Commun.* **2015**. https://doi.org/10.1557/mrc.2015.26.

(38) Madjet, M. E.; Berdiyorov, G. R.; El-Mellouhi, F.; Alharbi, F. H.; Akimov,

A. V.; Kais, S. Cation Effect on Hot Carrier Cooling in Halide Perovskite Materials. *J. Phys. Chem. Lett.* **2017**. https://doi.org/10.1021/acs.jpclett.7b01732.

(39) Zakutayev, A.; Caskey, C. M.; Fioretti, A. N.; Ginley, D. S.; Vidal, J.; Stevanovic, V.; Tea, E.; Lany, S. Defect Tolerant Semiconductors for Solar Energy Conversion. *Journal of Physical Chemistry Letters*. 2014. https://doi.org/10.1021/jz5001787.

(40) Kovalenko, M. V.; Protesescu, L.; Bodnarchuk, M. I. Properties and Potential Optoelectronic Applications of Lead Halide Perovskite Nanocrystals. *Science*. 2017. https://doi.org/10.1126/science.aam7093.

(41) D'Innocenzo, V.; Grancini, G.; Alcocer, M. J. P.; Kandada, A. R. S.; Stranks, S. D.; Lee, M. M.; Lanzani, G.; Snaith, H. J.; Petrozza, A. Excitons versus Free Charges in Organo-Lead Tri-Halide Perovskites. *Nat. Commun.* **2014**, *5*. https://doi.org/10.1038/ncomms4586.

(42) Cingolani, R.; Calcagnile, L.; Colí, G.; Rinaldi, R.; Lomoscolo, M.; DiDio, M.; Franciosi, A.; Vanzetti, L.; LaRocca, G. C.; Campi, D. Radiative Recombination Processes in Wide-Band-Gap II–VI Quantum Wells: The Interplay between Excitons and Free Carriers. *J. Opt. Soc. Am. B* **1996**, *13* (6), 1268. https://doi.org/10.1364/JOSAB.13.001268.

(43) Saha, M. N. On a Physical Theory of Stellar Spectra. *Proc. R. Soc. A Math. Phys. Eng. Sci.* **1921**, *99* (697), 135–153. https://doi.org/10.1098/rspa.1921.0029.

(44) Shah, J. *Ultrafast Spectroscopy of Semiconductors and Semiconductor Nanostructures*; 1999. https://doi.org/10.1007/978-3-662-03299-2.

(45) La-O-Vorakiat, C.; Xia, H.; Kadro, J.; Salim, T.; Zhao, D.; Ahmed, T.; Lam, Y. M.; Zhu, J. X.; Marcus, R. A.; Michel-Beyerle, M. E.; Chia, E. E. M. Phonon Mode Transformation Across the Orthohombic-Tetragonal Phase Transition in a Lead Iodide Perovskite CH3NH3PbI3: A Terahertz Time-Domain Spectroscopy Approach. *J. Phys. Chem. Lett.* **2016**. https://doi.org/10.1021/acs.jpclett.5b02223.

(46) Zhu, X. Y.; Podzorov, V. Charge Carriers in Hybrid Organic-Inorganic Lead Halide Perovskites Might Be Protected as Large Polarons. *Journal of Physical Chemistry Letters*. 2015, pp 4758–4761. https://doi.org/10.1021/acs.jpclett.5b02462.

(47) Brenner, T. M.; Egger, D. A.; Kronik, L.; Hodes, G.; Cahen, D. Hybrid Organic - Inorganic Perovskites: Low-Cost Semiconductors with Intriguing Charge-Transport Properties. *Nat. Rev. Mater.* **2016**, *1* (1), 1–16. https://doi.org/10.1038/natrevmats.2015.7.

(48) Hsu, Y. H.; Chen, Y. A.; Tseng, H. W.; Zhang, Z.; Shen, J. Y.; Chuang, W. T.; Lin, T. C.; Lee, C. S.; Hung, W. Y.; Hong, B. C.; Liu, S. H.; Chou, P. T. Locked Ortho - And Para -Core Chromophores of Green Fluorescent Protein; Dramatic Emission Enhancement via Structural Constraint. *J. Am. Chem. Soc.* **2014**. https://doi.org/10.1021/ja5062856.

(49) Miyata, K.; Meggiolaro, D.; Tuan Trinh, M.; Joshi, P. P.; Mosconi, E.; Jones, S. C.; De Angelis, F.; Zhu, X. Y. Large Polarons in Lead Halide Perovskites. *Sci. Adv.* **2017**, *3* (8). https://doi.org/10.1126/sciadv.1701217.

(50) Biaggio, I. Mobility of an Electron in a Multimode Polar Lattice. *Phys. Rev. B - Condens. Matter Mater. Phys.* **1999**. https://doi.org/10.1103/PhysRevB.60.299.

(51) Feynman, R. P.; Hellwarth, R. W.; Iddings, C. K.; Platzman, P. M. Mobility of Slow Electrons in a Polar Crystal. *Phys. Rev.* **1962**, *127* (4), 1004–1017. https://doi.org/10.1103/PhysRev.127.1004.

(52) Wehrenfennig, C.; Eperon, G. E.; Johnston, M. B.; Snaith, H. J.; Herz, L. M. High Charge Carrier Mobilities and Lifetimes in Organolead Trihalide Perovskites. *Adv. Mater.* **2014**. https://doi.org/10.1002/adma.201305172.

(53) Wehrenfennig, C.; Liu, M.; Snaith, H. J.; Johnston, M. B.; Herz, L. M. Charge-Carrier Dynamics in Vapour-Deposited Films of the Organolead Halide Perovskite CH3NH3PbI3-XClx. *Energy Environ. Sci.* **2014**. https://doi.org/10.1039/c4ee01358a.

(54) DeQuilettes, D. W.; Vorpahl, S. M.; Stranks, S. D.; Nagaoka, H.; Eperon, G. E.; Ziffer, M. E.; Snaith, H. J.; Ginger, D. S. Impact of Microstructure on Local Carrier Lifetime in Perovskite Solar Cells. *Science (80-.).* **2015**, *348* (6235), 683–686. https://doi.org/10.1126/science.aaa5333.

(55) Yao, J.; Kirchartz, T.; Vezie, M. S.; Faist, M. A.; Gong, W.; He, Z.; Wu, H.; Troughton, J.; Watson, T.; Bryant, D.; Nelson, J. Quantifying Losses in Open-Circuit Voltage in Solution-Processable Solar Cells. *Phys. Rev. Appl.* **2015**. https://doi.org/10.1103/PhysRevApplied.4.014020.

(56) Buin, A.; Pietsch, P.; Xu, J.; Voznyy, O.; Ip, A. H.; Comin, R.; Sargent, E. H. Materials Processing Routes to Trap-Free Halide Perovskites. *Nano Lett.* **2014**. https://doi.org/10.1021/nl502612m.

(57) Kim, J.; Lee, S. H.; Lee, J. H.; Hong, K. H. The Role of Intrinsic Defects in Methylammonium Lead Iodide Perovskite. *J. Phys. Chem. Lett.* **2014**. https://doi.org/10.1021/jz500370k.

(58) Du, M. H. Density Functional Calculations of Native Defects in CH3NH3PbI3: Effects of Spin - Orbit Coupling and Self-Interaction Error. *J. Phys. Chem. Lett.* **2015**. https://doi.org/10.1021/acs.jpclett.5b00199.

(59) Noel, N. K.; Abate, A.; Stranks, S. D.; Parrott, E. S.; Burlakov, V. M.; Goriely, A.; Snaith, H. J. Enhanced Photoluminescence and Solar Cell Performance via Lewis Base Passivation of Organic-Inorganic Lead Halide Perovskites. *ACS Nano* **2014**, *8* (10), 9815–9821. https://doi.org/10.1021/nn5036476.

(60) Stranks, S. D. Nonradiative Losses in Metal Halide Perovskites. *ACS Energy Letters*. 2017. https://doi.org/10.1021/acsenergylett.7b00239.

(61) Duim, H.; Adjokatse, S.; Kahmann, S.; ten Brink, G. H.; Loi, M. A. The Impact of Stoichiometry on the Photophysical Properties of Ruddlesden–Popper Perovskites. *Adv. Funct. Mater.* **2020**. https://doi.org/10.1002/adfm.201907505.

(62) Leverenz, H. W. *An Introduction to Luminescence of Solids*; 1950.

(63) Yang, Y.; Yang, M.; Li, Z.; Crisp, R.; Zhu, K.; Beard, M. C. Comparison of Recombination Dynamics in CH3NH3PbBr3 and CH3NH3PbI3 Perovskite Films: Influence of Exciton Binding Energy. *J. Phys. Chem. Lett.* **2015**. https://doi.org/10.1021/acs.jpclett.5b02290.

(64) Bohn, B. J.; Tong, Y.; Gramlich, M.; Lai, M. L.; Döblinger, M.; Wang, K.; Hoye, R. L. Z.; Müller-Buschbaum, P.; Stranks, S. D.; Urban, A. S.; Polavarapu, L.; Feldmann, J. Boosting Tunable Blue Luminescence of Halide Perovskite Nanoplatelets through Postsynthetic Surface Trap Repair. *Nano Lett.* **2018**. https://doi.org/10.1021/acs.nanolett.8b02190.

(65) Yang, D.; Ming, W.; Shi, H.; Zhang, L.; Du, M. H. Fast Diffusion of Native Defects and Impurities in Perovskite Solar Cell Material CH3NH3PbI3. *Chem. Mater.* **2016**. https://doi.org/10.1021/acs.chemmater.6b01348.

(66) Cardona, M. Band Parameters of Semiconductors with Zincblende, Wurtzite, and Germanium Structure. *J. Phys. Chem. Solids* **1963**. https://doi.org/10.1016/0022-3697(63)90097-0.

(67) Svoboda, K.; Denk, W.; Kleinfeld, D.; Tank, D. W. In Vivo Dendritic Calcium Dynamics in Neocortical Pyramidal Neurons. *Nature* **1997**. https://doi.org/10.1038/385161a0.

(68) Helmchen, F.; Svoboda, K.; Denk, W.; Tank, D. W. In Vivo Dendritic Calcium Dynamics in Deep-Layer Cortical Pyramidal Neurons. *Nat. Neurosci.* **1999**. https://doi.org/10.1038/14788.

(69) Stosiek, C.; Garaschuk, O.; Holthoff, K.; Konnerth, A. In Vivo Two-Photon Calcium Imaging of Neuronal Networks. *Proc. Natl. Acad. Sci. U. S. A.* **2003**. https://doi.org/10.1073/pnas.1232232100.

(70) Christie, R. H.; Bacskai, B. J.; Zipfel, W. R.; Williams, R. M.; Kajdasz, S. T.; Webb, W. W.; Hyman, B. T. Growth Arrest of Individual Senile Plaques

in a Model of Alzheimer’s Disease Observed by in Vivo Multiphoton Microscopy. *J. Neurosci.* **2001**. https://doi.org/10.1523/jneurosci.21-03-00858.2001.

(71) Bacskai, B. J.; Kajdasz, S. T.; Christie, R. H.; Carter, C.; Games, D.; Seubert, P.; Schenk, D.; Hyman, B. T. Imaging of Amyloid-β Deposits in Brains of Living Mice Permits Direct Observation of Clearance of Plaques with Immunotherapy. *Nat. Med.* **2001**. https://doi.org/10.1038/85525.

(72) Yuste, R.; Denk, W. Dendritic Spines as Basic Functional Units of Neuronal Integration. *Nature*. 1995. https://doi.org/10.1038/375682a0.

(73) Mainen, Z. F.; Malinow, R.; Svoboda, K. Synaptic Calcium Transients in Single Spines Indicate That NMDA Receptors Are Not Saturated. *Nature* **1999**. https://doi.org/10.1038/20187.

(74) Göppert-Mayer, M. Über Elementarakte Mit Zwei Quantensprüngen. *Ann. Phys.* **1931**. https://doi.org/10.1002/andp.19314010303.

(75) Garrett, W. K. and C. G. B. Two-Photon Excitation in CaF2:EU2+. *Phys. Rev. Lett.* **1961**, *7* (6), 229–232.

(76) SHEPPARD, C.; GU, M. Image Formation in Two-Photon Fluorescence Microscopy. *Opt.* **1990**.

(77) Electromagnetic Diffraction in Optical Systems, II. Structure of the Image Field in an Aplanatic System. *Proc. R. Soc. London. Ser. A. Math. Phys. Sci.* **1959**. https://doi.org/10.1098/rspa.1959.0200.

(78) Zipfel, W. R.; Williams, R. M.; Webb, W. W. Nonlinear Magic: Multiphoton Microscopy in the Biosciences. *Nature Biotechnology*. 2003. https://doi.org/10.1038/nbt899.

(79) Xu, C.; Zipfel, W.; Shear, J. B.; Williams, R. M.; Webb, W. W. Multiphoton Fluorescence Excitation: New Spectral Windows for Biological Nonlinear Microscopy. *Proc. Natl. Acad. Sci. U. S. A.* **1996**. https://doi.org/10.1073/pnas.93.20.10763.

(80) Xu, C.; Webb, W. W. Multiphoton Excitation of Molecular Fluorophores and Nonlinear Laser Microscopy. In *Topics in Fluorescence Spectroscopy*; 2002. https://doi.org/10.1007/0-306-47070-5_11.

(81) Guo, Z.; Manser, J. S.; Wan, Y.; Kamat, P. V.; Huang, L. Spatial and Temporal Imaging of Long-Range Charge Transport in Perovskite Thin Films by Ultrafast Microscopy. *Nat. Commun.* **2015**, *6*. https://doi.org/10.1038/ncomms8471.

(82) Leblebici, S. Y.; Leppert, L.; Li, Y.; Reyes-Lillo, S. E.; Wickenburg, S.; Wong, E.; Lee, J.; Melli, M.; Ziegler, D.; Angell, D. K.; Ogletree, D. F.;

Ashby, P. D.; Toma, F. M.; Neaton, J. B.; Sharp, I. D.; Weber-Bargioni, A. Facet-Dependent Photovoltaic Efficiency Variations in Single Grains of Hybrid Halide Perovskite. *Nat. Energy* **2016**. https://doi.org/10.1038/nenergy.2016.93.

(83) Jones, T. W.; Osherov, A.; Alsari, M.; Sponseller, M.; Duck, B. C.; Jung, Y. K.; Settens, C.; Niroui, F.; Brenes, R.; Stan, C. V.; Li, Y.; Abdi-Jalebi, M.; Tamura, N.; MacDonald, J. E.; Burghammer, M.; Friend, R. H.; Bulović, V.; Walsh, A.; Wilson, G. J.; Lilliu, S.; Stranks, S. D. Lattice Strain Causes Non-Radiative Losses in Halide Perovskites. *Energy Environ. Sci.* **2019**. https://doi.org/10.1039/c8ee02751j.

(84) Nah, S.; Spokoyny, B.; Stoumpos, C.; Soe, C. M. M.; Kanatzidis, M.; Harel, E. Spatially Segregated Free-Carrier and Exciton Populations in Individual Lead Halide Perovskite Grains. *Nat. Photonics* **2017**. https://doi.org/10.1038/nphoton.2017.36.

(85) Kojima, A.; Teshima, K.; Shirai, Y.; Miyasaka, T. Organometal Halide Perovskites as Visible-Light Sensitizers for Photovoltaic Cells. *J. Am. Chem. Soc.* **2009**, *131* (17), 6050–6051. https://doi.org/10.1021/ja809598r.

(86) Shi, Q.; Ghosh, S.; Sarkar, A. S.; Kumar, P.; Wang, Z.; Pal, S. K.; Pullerits, T.; Karki, K. J. Variation in the Photocurrent Response Due to Different Emissive States in Methylammonium Lead Bromide Perovskites. *J. Phys. Chem. C* **2018**, *122* (7), 3818–3823. https://doi.org/10.1021/acs.jpcc.8b00542.

(87) Debye, P.; Sears, F. W. On the Scattering of Light by Supersonic Waves. *Proc. Natl. Acad. Sci.* **1932**. https://doi.org/10.1073/pnas.18.6.409.

(88) Lucas, R.; Biquard, P. Propriétés Optiques Des Milieux Solides et Liquides Soumis Aux Vibrations Élastiques Ultra Sonores. *J. Phys. le Radium* **1932**. https://doi.org/10.1051/jphysrad:01932003010046400.

(89) Grulkowski, I.; Jankowski, D.; Kwiek, P. Acousto-Optic Interaction of a Gaussian Laser Beam with an Ultrasonic Wave of Cylindrical Symmetry. *Appl. Opt.* **2007**. https://doi.org/10.1364/AO.46.005870.

(90) Mohamed, A. E. N. A.; El-Halawany, M. M. E.; Rashed, A. N. Z.; Tabbour, M. S. F. High Transmission Performance of Radio over Fiber Systems over Traditional Optical Fiber Communication Systems Using Different Coding Formats for Long Haul Applications. *Nonlinear Opt. Quantum Opt.* **2012**.

(91) Born, M.; Wolf, E.; Hecht, E. Principles of Optics: Electromagnetic Theory of Propagation, Interference and Diffraction of Light . *Phys. Today* **2000**. https://doi.org/10.1063/1.1325200.

(92) Fu, S.; Sakurai, A.; Liu, L.; Edman, F.; Pullerits, T.; Öwall, V.; Karki, K. J.

Generalized Lock-in Amplifier for Precision Measurement of High Frequency Signals. *Rev. Sci. Instrum.* **2013**, *84* (11). https://doi.org/10.1063/1.4827085.

(93) Iaru, C. M.; Geuchies, J. J.; Koenraad, P. M.; Vanmaekelbergh, D.; Silov, A. Y. Strong Carrier-Phonon Coupling in Lead Halide Perovskite Nanocrystals. *ACS Nano* **2017**. https://doi.org/10.1021/acsnano.7b05033.

(94) Zhu, H.; Miyata, K.; Fu, Y.; Wang, J.; Joshi, P. P.; Niesner, D.; Williams, K. W.; Jin, S.; Zhu, X. Y. Screening in Crystalline Liquids Protects Energetic Carriers in Hybrid Perovskites. *Science (80-.).* **2016**, *353* (6306), 1409–1413. https://doi.org/10.1126/science.aaf9570].

(95) Karki, K. J.; Abdellah, M.; Zhang, W.; Pullerits, T. Different Emissive States in the Bulk and at the Surface of Methylammonium Lead Bromide Perovskite Revealed by Two-Photon Micro-Spectroscopy and Lifetime Measurements. *APL Photonics* **2016**, *1* (4), 046103. https://doi.org/10.1063/1.4948645.

(96) DeQuilettes, D. W.; Zhang, W.; Burlakov, V. M.; Graham, D. J.; Leijtens, T.; Osherov, A.; Bulović, V.; Snaith, H. J.; Ginger, D. S.; Stranks, S. D. Photo-Induced Halide Redistribution in Organic-Inorganic Perovskite Films. *Nat. Commun.* **2016**. https://doi.org/10.1038/ncomms11683.

(97) Chen, F.; Zhu, C.; Xu, C.; Fan, P.; Qin, F.; Gowri Manohari, A.; Lu, J.; Shi, Z.; Xu, Q.; Pan, A. Crystal Structure and Electron Transition Underlying Photoluminescence of Methylammonium Lead Bromide Perovskites. *J. Mater. Chem. C* **2017**, *5* (31), 7739–7745. https://doi.org/10.1039/C7TC01945A.

(98) Chen, F.; Zhu, C.; Xu, C.; Fan, P.; Qin, F.; Gowri Manohari, A.; Lu, J.; Shi, Z.; Xu, Q.; Pan, A. Crystal Structure and Electron Transition Underlying Photoluminescence of Methylammonium Lead Bromide Perovskites. *J. Mater. Chem. C* **2017**. https://doi.org/10.1039/c7tc01945a.

(99) Krzysztof Galkowski, ab Anatolie Mitioglu, a Atsuhiko Miyata, a Paulina Plochocka, A.; Oliver Portugall, a Giles E. Eperon, c Jacob Tse-Wei Wang, c Thomas Stergiopoulos, C.; Samuel D. Stranks, c H. J. S. and R. J. N. Determination of the Exciton Binding Energy and Effective Masses for Methylammonium and Formamidinium Lead Tri-Halide Perovskite Semiconductors. *Energy Environ. Sci.* **2016**, *9*, 962.

(100) Biaggio, I. Mobility of an Electron in a Multimode Polar Lattice. *Phys. Rev. B - Condens. Matter Mater. Phys.* **1999**, *60* (1), 299–307. https://doi.org/10.1103/PhysRevB.60.299.

(101) Wright, A. D.; Verdi, C.; Milot, R. L.; Eperon, G. E.; Pérez-Osorio, M. A.; Snaith, H. J.; Giustino, F.; Johnston, M. B.; Herz, L. M. Electron-Phonon

Coupling in Hybrid Lead Halide Perovskites. *Nat. Commun.* **2016**, *7*. https://doi.org/10.1038/ncomms11755.

(102) Diab, H.; Trippé-Allard, G.; Lédée, F.; Jemli, K.; Vilar, C.; Bouchez, G.; Jacques, V. L. R.; Tejeda, A.; Even, J.; Lauret, J. S.; Deleporte, E.; Garrot, D. Narrow Linewidth Excitonic Emission in Organic-Inorganic Lead Iodide Perovskite Single Crystals. *J. Phys. Chem. Lett.* **2016**, *7* (24), 5093–5100. https://doi.org/10.1021/acs.jpclett.6b02261.

(103) Rudin, S.; Reinecke, T. L. Temperature-Dependent Exciton Linewidths in Semiconductor Quantum Wells. *Phys. Rev. B* **1990**, *41* (5), 3017–3027. https://doi.org/10.1103/PhysRevB.41.3017.

(104) Malikova, L.; Krystek, W.; Pollak, F. H.; Dai, N.; Cavus, A.; Tamargo, M. Temperature Dependence of the Direct Gaps of ZnSe AnSe. *Phys. Rev. B - Condens. Matter Mater. Phys.* **1996**, *54* (3), 1819–1824. https://doi.org/10.1103/PhysRevB.54.1819.

(105) Lee, J.; Koteles, E. S.; Vassell, M. O. Luminescence Linewidths of Excitons in GaAs Quantum Wells below 150 K. *Phys. Rev. B* **1986**. https://doi.org/10.1103/PhysRevB.33.5512.

(106) Ni, L.; Huynh, U.; Cheminal, A.; Thomas, T. H.; Shivanna, R.; Hinrichsen, T. F.; Ahmad, S.; Sadhanala, A.; Rao, A. Real-Time Observation of Exciton-Phonon Coupling Dynamics in Self-Assembled Hybrid Perovskite Quantum Wells. *ACS Nano* **2017**, *11* (11), 10834–10843. https://doi.org/10.1021/acsnano.7b03984.

(107) Zhu, Q.; Zheng, K.; Abdellah, M.; Generalov, A.; Haase, D.; Carlson, S.; Niu, Y.; Heimdal, J.; Engdahl, A.; Messing, M. E.; Pullerits, T.; Canton, S. E. Correlating Structure and Electronic Band-Edge Properties in Organolead Halide Perovskites Nanoparticles. *Phys. Chem. Chem. Phys.* **2016**, *18* (22), 14933–14940. https://doi.org/10.1039/c6cp01843b.

(108) Tilchin, J.; Dirin, D. N.; Maikov, G. I.; Sashchiuk, A.; Kovalenko, M. V.; Lifshitz, E. Hydrogen-like Wannier-Mott Excitons in Single Crystal of Methylammonium Lead Bromide Perovskite. *ACS Nano* **2016**, *10* (6), 6363–6371. https://doi.org/10.1021/acsnano.6b02734.

(109) Hu, C. H. and K. W. and X. Z. and H. Y. and X. S. and Q. Y. and Bin. Unraveling Surface and Bulk Trap States in Lead Halide Perovskite Solar Cells Using Impedance Spectroscopy. *J. Phys. D. Appl. Phys.* **2018**, *51* (9), 95501. https://doi.org/10.1088/1361-6463/aaa7cd.

(110) Jacques I. Pankove. *Optical Processes in Semiconductors*; 1971.

(111) Osipov, V. Al; Shang, X.; Hansen, T.; Pullerits, T.; Karki, K. J. Nature of Relaxation Processes Revealed by the Action Signals of Intensity-Modulated

Light Fields. *Phys. Rev. A* **2016**, *94* (5). https://doi.org/10.1103/PhysRevA.94.053845.

(112) Dobrovolsky, A.; Merdasa, A.; Unger, E. L.; Yartsev, A.; Scheblykin, I. G. Defect-Induced Local Variation of Crystal Phase Transition Temperature in Metal-Halide Perovskites. *Nat. Commun.* **2017**. https://doi.org/10.1038/s41467-017-00058-w.

(113) Richter, J. M.; Abdi-Jalebi, M.; Sadhanala, A.; Tabachnyk, M.; Rivett, J. P. H.; Pazos-Outón, L. M.; Gödel, K. C.; Price, M.; Deschler, F.; Friend, R. H. Enhancing Photoluminescence Yields in Lead Halide Perovskites by Photon Recycling and Light Out-Coupling. *Nat. Commun.* **2016**. https://doi.org/10.1038/ncomms13941.

(114) Fang, H. H.; Raissa, R.; Abdu-Aguye, M.; Adjokatse, S.; Blake, G. R.; Even, J.; Loi, M. A. Photophysics of Organic-Inorganic Hybrid Lead Iodide Perovskite Single Crystals. *Adv. Funct. Mater.* **2015**. https://doi.org/10.1002/adfm.201404421.

(115) Tress, W.; Yavari, M.; Domanski, K.; Yadav, P.; Niesen, B.; Correa Baena, J. P.; Hagfeldt, A.; Graetzel, M. Interpretation and Evolution of Open-Circuit Voltage, Recombination, Ideality Factor and Subgap Defect States during Reversible Light-Soaking and Irreversible Degradation of Perovskite Solar Cells. *Energy Environ. Sci.* **2018**. https://doi.org/10.1039/c7ee02415k.

(116) Ciesielski, R.; Schäfer, F.; Hartmann, N. F.; Giesbrecht, N.; Bein, T.; Docampo, P.; Hartschuh, A. Grain Boundaries Act as Solid Walls for Charge Carrier Diffusion in Large Crystal MAPI Thin Films. *ACS Appl. Mater. Interfaces* **2018**. https://doi.org/10.1021/acsami.7b17938.

(117) Wang, K. H.; Li, L. C.; Shellaiah, M.; Sun, K. W. Structural and Photophysical Properties of Methylammonium Lead Tribromide (MAPbBr3) Single Crystals. *Sci. Rep.* **2017**. https://doi.org/10.1038/s41598-017-13571-1.

(118) Chen, Q.; De Marco, N.; Yang, Y.; Song, T. Bin; Chen, C. C.; Zhao, H.; Hong, Z.; Zhou, H.; Yang, Y. Under the Spotlight: The Organic-Inorganic Hybrid Halide Perovskite for Optoelectronic Applications. *Nano Today*. 2015. https://doi.org/10.1016/j.nantod.2015.04.009.

(119) Stoumpos, C. C.; Malliakas, C. D.; Kanatzidis, M. G. Semiconducting Tin and Lead Iodide Perovskites with Organic Cations: Phase Transitions, High Mobilities, and near-Infrared Photoluminescent Properties. *Inorg. Chem.* **2013**. https://doi.org/10.1021/ic401215x.

(120) Guo, D.; Bartesaghi, D.; Wei, H.; Hutter, E. M.; Huang, J.; Savenije, T. J. Photoluminescence from Radiative Surface States and Excitons in Methylammonium Lead Bromide Perovskites. *J. Phys. Chem. Lett.* **2017**, *8*

(17), 4258–4263. https://doi.org/10.1021/acs.jpclett.7b01642.

(121) Miller, O. D.; Yablonovitch, E.; Kurtz, S. R. Strong Internal and External Luminescence as Solar Cells Approach the Shockley-Queisser Limit. *IEEE J. Photovoltaics* **2012**, *2* (3), 303–311. https://doi.org/10.1109/JPHOTOV.2012.2198434.

(122) Eperon, G. E.; Moerman, D.; Ginger, D. S. Anticorrelation between Local Photoluminescence and Photocurrent Suggests Variability in Contact to Active Layer in Perovskite Solar Cells. *ACS Nano* **2016**, *10* (11), 10258–10266. https://doi.org/10.1021/acsnano.6b05825.

(123) Miller, O. D.; Yablonovitch, E.; Kurtz, S. R. Strong Internal and External Luminescence as Solar Cells Approach the Shockley-Queisser Limit. *IEEE J. Photovoltaics* **2012**, *2* (3), 303–311. https://doi.org/10.1109/JPHOTOV.2012.2198434.

(124) Dar, M. I.; Jacopin, G.; Meloni, S.; Mattoni, A.; Arora, N.; Boziki, A.; Zakeeruddin, S. M.; Rothlisberger, U.; Gra tzel, M. Origin of Unusual Bandgap Shift and Dual Emission in Organic-Inorganic Lead Halide Perovskites. *Sci. Adv.* **2016**, *2* (10), e1601156–e1601156. https://doi.org/10.1126/sciadv.1601156.

(125) Kelzenberg, M. D.; Turner-Evans, D. B.; Kayes, B. M.; Filier, M. A.; Putnam, M. C.; Lewis, N. S.; Atwater, H. A. Photovoltaic Measurements in Single-Nanowire Silicon Solar Cells. *Nano Lett.* **2008**. https://doi.org/10.1021/nl072622p.

(126) Graham, R.; Yu, D. Scanning Photocurrent Microscopy in Semiconductor Nanostructures. *Modern Physics Letters B*. 2013. https://doi.org/10.1142/S0217984913300184.

(127) Saidaminov, M. I.; Haque, M. A.; Almutlaq, J.; Sarmah, S.; Miao, X. H.; Begum, R.; Zhumekenov, A. A.; Dursun, I.; Cho, N.; Murali, B.; Mohammed, O. F.; Wu, T.; Bakr, O. M. Inorganic Lead Halide Perovskite Single Crystals: Phase-Selective Low-Temperature Growth, Carrier Transport Properties, and Self-Powered Photodetection. *Adv. Opt. Mater.* **2017**. https://doi.org/10.1002/adom.201600704.

(128) Yang, B.; Mao, X.; Yang, S.; Li, Y.; Wang, Y.; Wang, M.; Deng, W.; Han, K. Low Threshold Two-Photon-Pumped Amplified Spontaneous Emission in CH3NH3PbBr3 Microdisks. *ACS Appl. Mater. Interfaces* **2016**. https://doi.org/10.1021/acsami.6b04246.

(129) Saidaminov, M. I.; Adinolfi, V.; Comin, R.; Abdelhady, A. L.; Peng, W.; Dursun, I.; Yuan, M.; Hoogland, S.; Sargent, E. H.; Bakr, O. M. Planar-Integrated Single-Crystalline Perovskite Photodetectors. *Nat. Commun.* **2015**. https://doi.org/10.1038/ncomms9724.

(130) Graham, R.; Miller, C.; Oh, E.; Yu, D. Electric Field Dependent Photocurrent Decay Length in Single Lead Sulfide Nanowire Field Effect Transistors. *Nano Lett.* **2011**. https://doi.org/10.1021/nl1038456.